Structural insights into oligomerization and mitochondrial remodeling of dynamin 1-like protein

Dissertation zur Erlangung des akademischen Grades des Doktors der Naturwissenschaften (Dr. rer. nat.)

eingereicht im Fachbereich Biologie, Chemie, Pharmazie der Freien Universität Berlin

vorgelegt von
Dipl.-Ing. Chris Fröhlich
aus der Lutherstadt Eisleben

Berlin
2013

Die vorliegende Arbeit wurde im Zeitraum April 2009 bis März 2013 am
Max-Delbrück-Centrum für Molekulare Medizin Berlin-Buch unter Anleitung von
PROF. DR. OLIVER DAUMKE
angefertigt.

1. Gutachter: Prof. Dr. Udo Heinemann
2. Gutachter: Prof. Dr. Oliver Daumke

Tag der Disputation: 29.07.2013

… to boldly go where no man has gone before.

Contents

Contents

Contents

___

List of Figures

List of Figures

_____

List of Tables

1.   Introduction

1.1.   Mitochondria

Mitochondria are double-membrane enclosed subcellular organelles occupying significant space within the cytoplasm of eukaryotic cells [1] (Figure 01). They are often termed the powerhouses of cells because mitochondria are the place of oxidative phosphorylation (OXPHOS), an important biological process of producing the energy storage molecule adenosine-5'-triphosphate (ATP) (reviewed in [2]). Furthermore, β-oxidation, the citric acid cycle, urea synthesis and gluconeogenesis take place in this organelle. Mitochondria also participate in calcium signaling, the assembly of iron-sulphur clusters, in the biosynthesis of haem, certain phospholipids, amino acids, vitamin co-factors, and intermediary metabolism, while also contributing to cellular stress responses such as apoptosis and autophagy (reviewed in [3]).

In terms of evolution, the concept of mitochondria-derived energy conversion (mistakenly ATP production is often referred to as energy production) revolutionized cellular metabolism and it is believed that development of complex multicellular organisms would have been impossible without mitochondria. Eukaryotic cells incapable to use sun light for energy conversion would be relatively ineffective with-
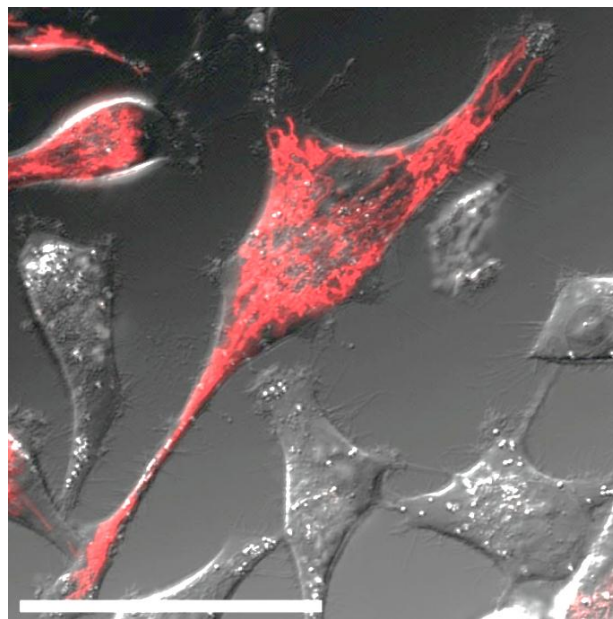
Figure 01:   Mitochondria in a HeLa cell. Confocal microscopy image showing HeLa cells stained with the mitochondrial marker dsRed2 (see 2.1.6).Depicted is an overlay of the bright field channel and the 584 nm channel (red light). As can be seen, mitochondria form an extensive cellular network. Scale bar = 50 µm.

out mitochondria and energy supply would depend solely on glycolysis yielding two molecules of ATP and NADH per molecule of glucose. This is less than 10 % of the total free energy potentially available by oxidation from one molecule of glucose. In contrast, when mitochondria further process pyruvate and finally oxidize it to CO_2 and H_2O nearly half of the theoretical oxidation energy of glucose is captured for ATP production, making mitochondria ultimate enhancers in terms of effectiveness. As a net result, approximately 30 ATP molecules are generated out of one glucose molecule. In addition to pyruvate, fatty acids and some amino acids are also used by mitochondria to produce ATP. Thus, the evolution of cellular respiration and the use of oxygen as THE final electron acceptor enable aerobic organisms to harness much more energy than can be derived from anaerobic metabolism.

Since mitochondrial ATP synthesis and proper mitochondrial function is strongly dependent on a functional mitochondrial membrane potential, the following chapter will focus on mitochondrial membrane composition and mitochondrial membrane dynamics in more detail.

1.1.1. The mitochondrial compartment

It is believed that mitochondria originate from alphaproteobacteria which have been engulfed by eukaryotic progenitors. Mitochondria in particular share a common evolutionary ancestor with the SAR11 clade, a lineage of one of the most abundant marine bacteria on earth [4]. It is noteworthy that already in 1910, the Russian scientist Konstantin Mereschkowski proposed the theory of symbiogenesis, nowadays known as the Endosymbiotic theory; that the evolution of complex multicellular organisms was accompanied by a symbiotic relationship with less complex organism [5]. As a result of being engulfed by a cell, mitochondria consist of an outer membrane (mom) and an inner membrane (mim) both of which are highly specialized membranes with different shapes, compositions, and functions. The existence of two membranes separates mitochondria into four distinct compartments: the mom, the mim, the space between the two membranes (the intermembrane space), and a matrix, the space within the inner membrane (Figure 02). The composition and shape of the mim and mom differ significantly (reviewed in [6]). Notably, both, the mim and mom, can be distinguished from the plasma membrane and other membrane compartments by the presence of the phospholipid cardiolipin, which is unique for mitochondria. Hence, cardiolipin is used as a marker for the
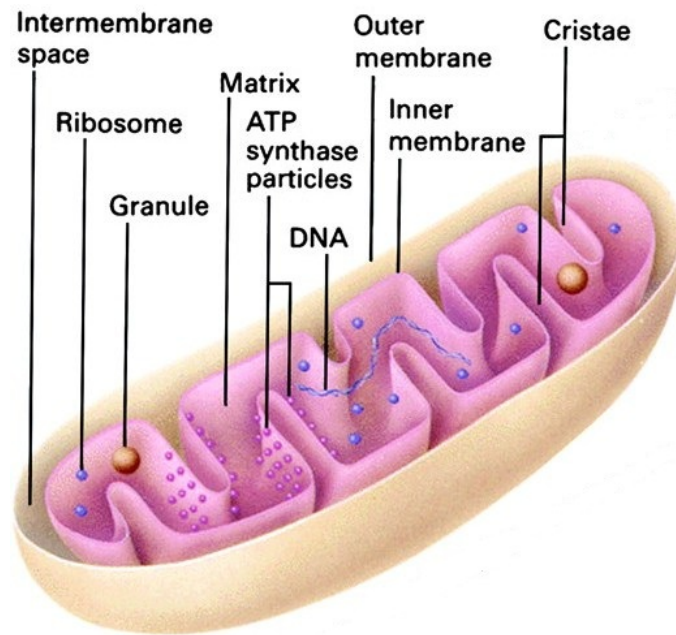
Figure 02: The mitochondrial morphology. Schematic representation showing a single mitochondrium. Selected components are depicted. Figure modified from [7]. For explanation, see text.

identification of the mitochondrial membrane. The mom contains about 4 mole percent cardiolipin (CL) whereas the mim contains up to 25 mole percent. Other phospholipids found in both membranes are phosphatidylcholine (PC, ~50 % mom, ~42% mim), phosphatidylethanolamine (PE, ~26 % mom, ~32 % mim), phosphatidylinositol (PI, ~14 % mom, ~4 % mim), and phosphatidylserine (PS, ~5 % mom and mim). Phosphatidylglycerol (PG) was also shown to be incorporated in both membranes whereas the sterol content of mitochondria is usually very low, except for cells synthesizing steroid hormones. Mitochondrial membrane lipid composition is strongly dependent on diet and hormonal state [6]. The high PE:PG ratio in addition to the presence of CL and PG indicate the bacterial origin of the mitochondrial membrane and is thought to be necessary for OXPHOS [8]. Most of the mitochondrial lipid content is produced *in situ* by mitochondria. The synthesis of lysophosphatidic acid (LPA) occurs in the mitochondria. LPA is further used mostly for triacylglycerol formation. Mitochondria also synthesize phosphatidic acid (PA) and PG, which is used for synthesis of CL. PE is produced by decarboxylation of PS and also exported to other organelles. However, some of the phospholipids are synthesized outside the mitochondrion and are imported.

The smooth mom surrounds the organelle, thereby maintaining its shape. Its lipid to protein ratio is about one third to two thirds, respectively [6]. Most of the proteins

associated with the mom are involved in glycolysis and phospholipid synthesis. Furthermore, the mom is perforated with porins, β-barrel shaped pore-forming transmembrane proteins, permitting the free diffusion of molecules of less than 5 kDa [9]. Porins are voltage-dependent anion channels (VDAC) allowing selective transport of small molecules, thus the mom is relatively permeable for sugars, nucleotides, inorganic phosphate, and ions. The mim is characterized by lamellar structures called cristae, folding into the matrix and accommodating the respiratory chain complexes. This wrinkle-like fold serves to increase the mim surface for the plethora of important metabolic reactions taking place here. Numerous small sphere-like structures are found on the mim surface facing into the matrix. These structures are associated with the multisubunit ATP synthase complex (F_1F_0 ATPase). Furthermore, many transport proteins and enzymes are embedded in the mim, accounting for the fact that the by weight lipid to protein ratio of the mim is about 1:8 [6]. The mim is permeable only for water, oxygen and CO_2, e.g. most other molecules and ions require specific transport systems for entry and exit. Finally, both the mim and the mom contain a sophisticated transport complex for translocation of proteins across the membranes (translocase of the outer and inner membrane; Tom and Tim, respectively), since most of mitochondrial proteins are encoded in the nucleus and have to be transported into the mitochondria. The intermembrane space serves for maintenance of adenine nucleotide balance and proteins imported into the matrix are processed here. It contains several enzymes which use ATP for phosphate transfer including adenylate kinase and creatine kinase. Finally, the protein-rich core of mitochondria, the matrix, contains the enzymes of the pyruvate dehydrogenase complex, citric acid cycle, and glycine oxidative decarboxylation during photorespiration as well as pools of important metabolites including ADP, ATP, NAD, and $NADH^+$ [7]. Furthermore it possesses a small genome (~ 16.4 kb in mammals) encoding 13 OXPHOS proteins and the machinery necessary to transcribe and translate them [10]. Taken together mitochondria form a sophisticated two-membrane system which is dynamic in terms of form and function as outlined in the next chapter.

1.1.2.   The mitochondrial network
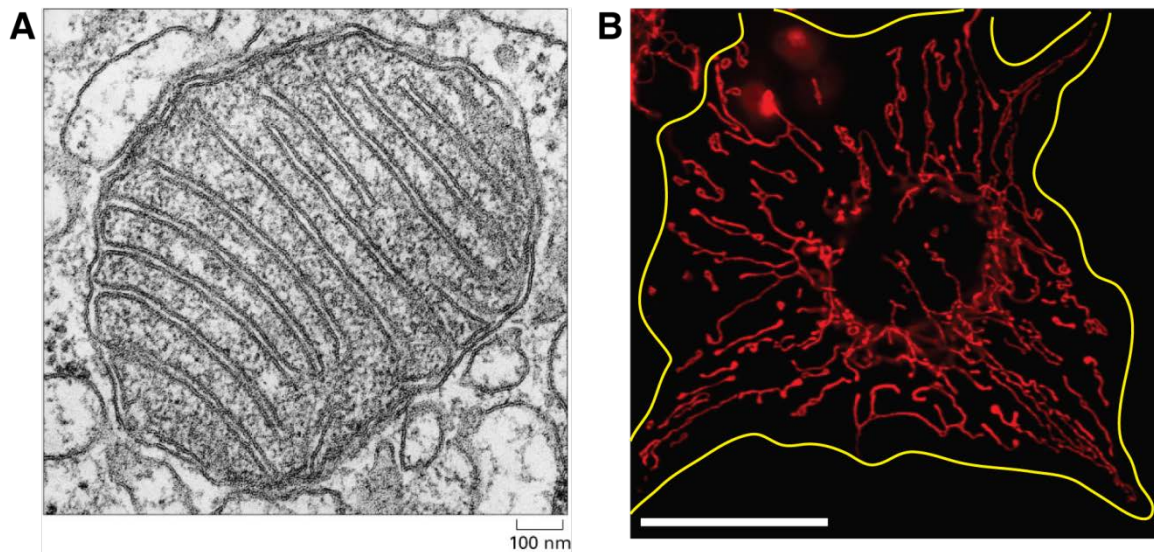
Figure 03:   The mitochondrial network. **A:** Typical electron microscopy picture showing a cross section of a mitochondrial tube. The mom, the mim, cristae, and matrix are clearly visible. Initially it was thought that mitochondria are discrete cell organelles like indicated in this picture. Picture by Daniel S. Friend. **B:** Confocal microscopy picture showing the mitochondrial network in a COS cell. Mitochondria are stained with dsRed2 (see 2.1.6). The cell shape was drawn by hand (yellow line). Scale bar = 50 μm.

Mitochondria are usually depicted as stiff and elongated cylinders resembling a single and discrete cell organelle. It was 1973 when the first evidence indicated that mitochondria form a long branched, interconnected, tubulovesicular network throughout the whole cell instead of being a set of single cell organelles [11] (Figure 03). Many independent studies proved these findings (extensively reviewed in [12]). Moreover, mitochondria are remarkably dynamic cell organelles that continuously divide and fuse and move along the cytoskeletal tracks. These fine-tuned processes allow control of intracellular distribution of mitochondria and determine their cell type-specific appearance. Thus, the morphology of mitochondria is not only dependent on its membrane composition (see 1.1.1) but is governed by the concerted balance between frequently occurring fusion and fission events. The dynamic shape and behavior of mitochondria allows the cell to respond to different physiological conditions. It has been widely accepted that mitochondrial dynamics is crucial for the maintenance of mitochondrial DNA, respiratory activity, and calcium signaling. Furthermore it was shown that mitochondrial dynamics plays a role in the control of embryonic development, apoptosis and neuronal plasticity (reviewed in [13, 14]).

As mitochondria cannot be created *de novo,* a scission mechanism is required for distribution of mitochondria throughout dividing cells. Scission also facilitates proper organelle transport and serves as quality control mechanism to eliminate dysfunctional mitochondria by mitophagy [15]. Furthermore, scission has been shown to be important for cytochrome c release of fragmented mitochondria during apoptosis [16]. The key mediator of mitochondrial division is dynamin 1-like protein (DNM1L, see 1.3.7) which is a member of the dynamin superfamily of G proteins (see 1.3). Mitochondrial fission is balanced by opposing fusion events in order to maintain a homogenous mitochondrial network by mixing content between constantly fusing and dividing organelles. The mitochondrial genome within the cell is heteroplasmic and fusion can rescue two mitochondria with mutations in different genes by cross-complementing each other. Furthermore, fusion and fission serve as repair mechanisms that mitigates effects of environmental damage by mixing protein and lipid content of the mitochondrial network. Therefore, fusion is a mechanism to optimize oxidative capacity in response to environmental cues [17]. The core components of the mitochondrial fusion machinery are also large GTPases of the dynamin superfamily which are grouped according to their involvement in inner- or outer membrane fusion (see 1.3.6). Mitofusins (Fzo1 in yeast, MFN1 and MFN2 in mammals) catalyze outer membrane fusion while dynamin-related OPA1 (Mgm1 in yeast) is responsible for inner membrane fusion (reviewed in [18]).

Given the fact that mitochondrial dynamics is an important tool of cellular response to constantly changing environmental cues, it is obvious that dysfunctional mito-chondrial fusion or fission processes can lead to severe diseases. The next chapter will give an overview on that topic.

1.1.3.   Mitochondria associated diseases

Human mitochondrial diseases are heterogeneous in terms of etiology and symptoms. Because of their central function regarding metabolism and energy supply, mitochondria dysfunction is implicated in a wide range of diverse diseases affecting any organ system; for example Alzheimer's -, Huntington's - or Parkinson's disease, cardiomyopathies, metabolic syndrome, cancer, and obesity to name just a few (extensively reviewed in [13, 18]). The primary cause of abnormal mitochondrial function is mtDNA mutation. Since the mitochondrial genome encodes 13 OXPHOS-related proteins, mutations in the mtDNA often cause defects of respiratory chain

function. Nuclear gene mutations are the second cause of mitochondrial dysfunction and can affect several other functions than respiratory chain defects. Some of these mutations are reliably associated with certain phenotypes although some phenotypes cannot be addressed to any mitochondria specific mutations yet. The glycolytic enzyme hexokinase, for example, can specifically interact with porins which are embedded in the mom (see 1.1.1). The physical association with the mom ensures the hexokinase's fast access to one of its substrates, ATP, which is produced by mitochondria. Bustamante and colleagues showed that mitochondria-bound hexokinase is highly elevated and the driving force for the extremely high glycolytic rates that take place aerobically in rapidly-growing malignant tumor cells, the so-called Warburg effect [19]. Thus, mitochondria can be involved in severe diseases without being a direct cause.

In contrast, certain proteins important for proper mitochondrial function were shown to be specifically responsible for a distinct phenotype. Parkin and PTEN-induced putative kinase 1 (PINK1), for example, are important proteins of the mitophagy pathway and mutations in either of the proteins lead to Parkinson's disease [20]. Furthermore, mitochondrial dynamics is crucial in terms of mitochondrial disease. Mutations in the mim fusion mediator protein MFN2 (see 1.3.6.1) was shown to be causative for autosomal dominant Charcot-Marie-Tooth type 2 disease - an early onset axonal sensorimotor neuropathy [21], and mutations in the mom fusion protein OPA1 (see 1.3.6.2) cause optic atrophy with a specific wide-ranging phenotype [22].

Defective mitochondrial fission also leads to severe diseases. Dysfunction of the mitochondrial division protein, DNM1L (see 1.3.7), has been implicated in a number of mitochondria-based neurological disorders (reviewed in [23]). Impaired mitochondrial function and increased fragmentation of mitochondria were reported in Parkinson's disease patients. Perturbed mitochondrial morphology in some of these patients might be caused by diminished proteasome-dependent degradation and subsequent accumulation of DNM1L. Fibroblasts from Alzheimer's disease patients show significantly elongated mitochondria and a marked decrease in DNM1L expression. Furthermore, S-nitrosylation of DNM1L caused by the expression of the β-amyloid protein was reported to trigger mitochondrial fission and induce synaptic loss and neuronal damage. This implicates DNM1L also in Alzheimer's disease [24], although these results are controversial [25]. Abnormal mitochondrial dynamics and altered DNM1L expression levels were also found in Huntington's disease patients.

Finally, a disease report described a newborn girl with the A395D mutation in DNM1L who showed severe developmental defects such as microcephaly, optic neuropathy, hypoplasia, persistent lactic acidemia, and elevated plasma levels of long-chain fatty acids [26]. It is difficult to define mitochondrial diseases in terms of causality because of the many overlapping phenotypes and a multifactorial spectrum of causes. However, as stated before impaired mitochondrial dynamics is a major cause leading to mitochondria associated diseases. Since dynamin-related G proteins are key regulators of mitochondrial fusion and fission events the next chapters will introduce this protein family in more detail beginning with a general overview on G proteins.

1.2.   G proteins

Nucleotide triphosphate binding and hydrolyzing proteins (NTPs) are indispensable for a plethora of fundamental aspects of life. Representing approximately 10 - 18 % of the predicted gene products in the sequenced prokaryotic and eukaryotic genomes, the mononucleotide-binding fold (P loop NTPase fold) is the most prevalent fold among NTPs and more strikingly the most prevalent domain in proteins encoded in the genomes of most cellular life forms [27]. One of at least seven major monophyletic lineages within the P loop NTPase fold is the GTPase superclass [28]. Members of this superclass are sometimes referred to as guanine nucleotide binding proteins (GNBPs) or more simple G proteins as they bind and hydrolyze GTP to $GDP + P_i$. All G proteins possess at least one canonical domain, the G domain, which is responsible for nucleotide binding and hydrolysis. Besides the G domain, several G proteins contain one or more additional domains which are characteristic for individual functions.

Many G proteins are directly responsible for the transmission of extracellular signals to the intracellular environment and are further involved in a wide range of cellular processes including protein synthesis, sensual perception, vesicle-associated processes, nuclear import and export, regulation of cell shape, cytoskeleton, cell migration, mitochondrial integrity and signal transduction cascades leading to cell proliferation and cell differentiation (extensively reviewed in [29]). Based on conserved sequence motifs, shared structural features and domain architectures (synapomorphies) of all available bacterial and eukaryotic G proteins two major groups of the GTPase superclass have been identified [28]. They were named the

_____
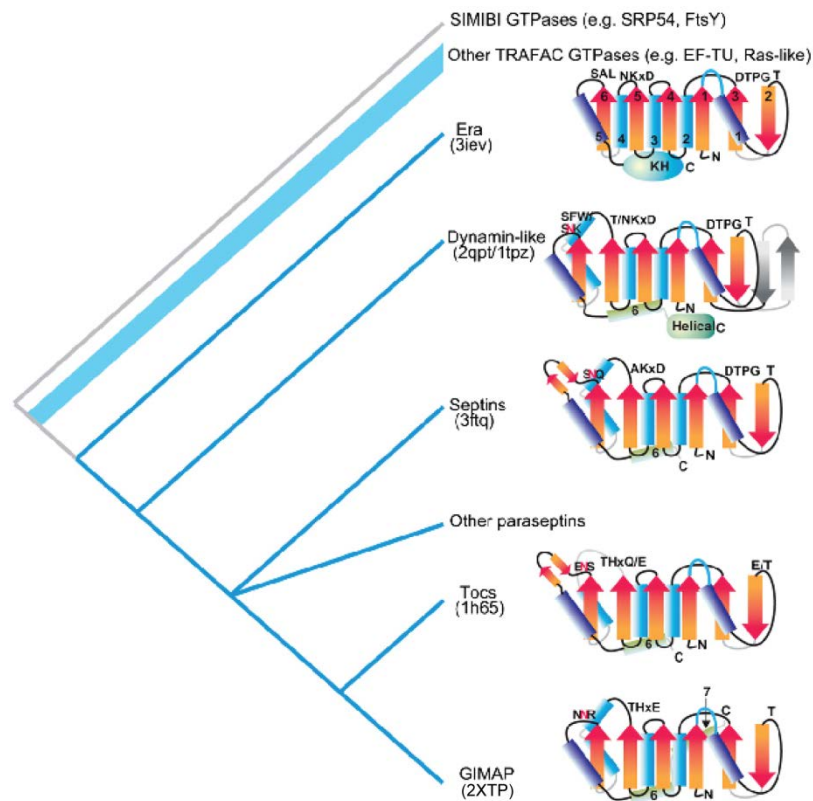
Figure 04: Higher-order relationship analysis of the dynamin superfamily. Cladogram showing higher-order relationships of a distinctive cluster within TRAFAC class proteins (see main text). Simplified topologies of representative members of each clade for which structures are available are shown (see PDB ID codes). Topologies also indicate the typical forms of the different conserved G domain motifs in a given group. The phosphate-binding loop is colored blue. The strands and helices are numbered in the Era structure, with the additional helices indicated in the structures in which they occur. Figure modified rom [30].

TRAFAC (translation factor related) and the SIMIBI class (signal recognition particle, MinD, BioD). The TRAFAC and SIMIBI class contain together more than 20 distinct families that are further subdivided into 57 subfamilies [28]. Recently, an important distinctive protein cluster within the TRAFAC class was described. Analysis of sequence and structural features and biochemical properties revealed a common ancestor for septins, paraseptins, translocon at the outer envelope membrane of chloroplasts (Toc) proteins, GTPase of immunity associated proteins (GIMAPs), *E. coli* Ras-like (Era) family proteins, and dynamin-like proteins excluding them from other TRAFAC class G proteins (Figure 04) [30]. Most of its members form nucleotide-dependent higher-ordered oligomers. Since the present work investigates a dynamin-like protein, the following chapters will focus specifically on that protein family.

1.3. The dynamin superfamily of G proteins
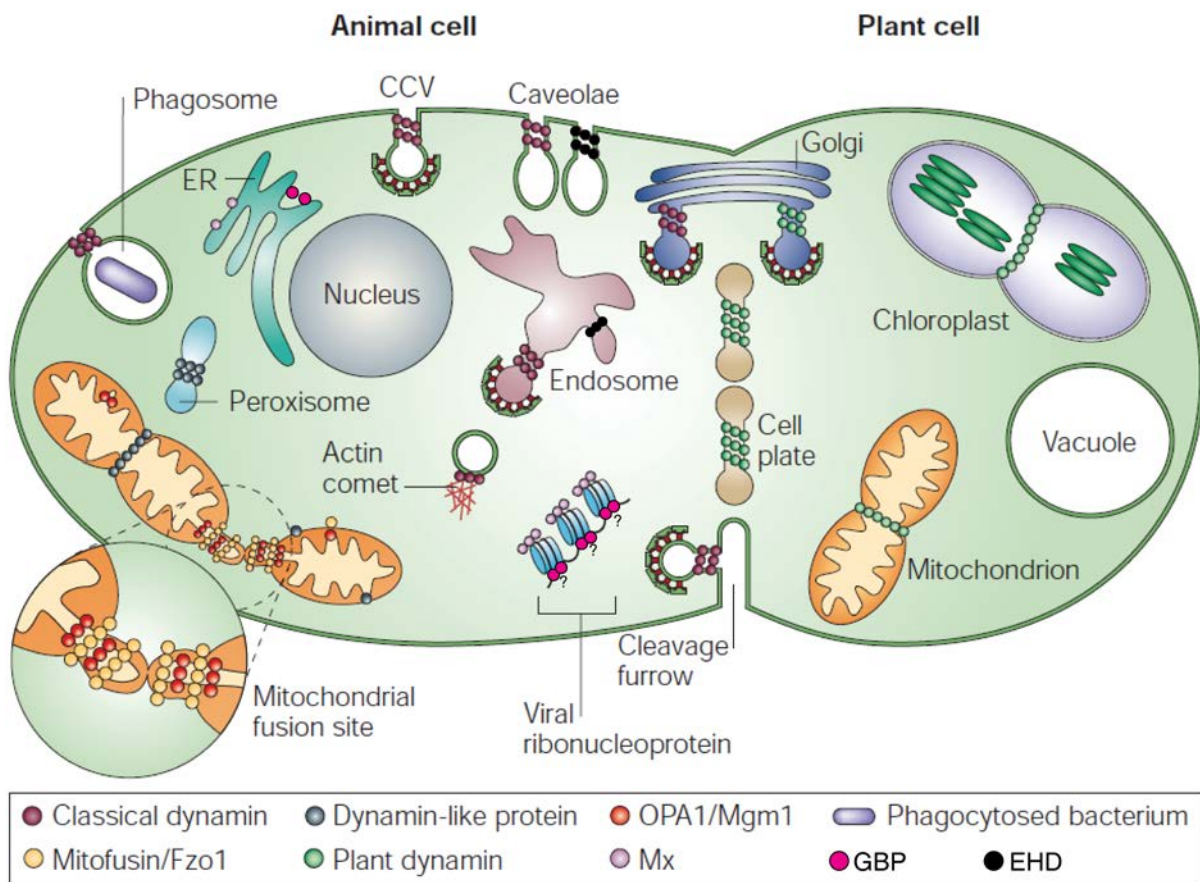
Figure 05: Selected dynamin superfamily proteins, their cellular localization and function. Figure modified from [31].

Members of the dynamin superfamily of proteins are large G proteins involved in a wide range of different cellular processes including budding off transport vesicles, fusion and division of mitochondria, viral host defense, division of peroxisomes and chloroplasts, and cytokinesis (Figure 05, reviewed in [31]), They are found mostly in the eukaryotic kingdom but appear also in some bacteria. Dynamin proteins can be distinguished from the small Ras-like and other TRAFAC class GTPases (see above) by their (1) low micromolar affinity for nucleotides and a relatively high basal GTPase activity (2) enhanced GTPase activity in the presence of lipid-templates, (3) lipid-template dependent oligomerization and the propensity to self-assemble. The dynamin superfamily includes classical dynamins and dynamin-related proteins such as Myxovirus resistance proteins (Mx proteins) [32], bacterial dynamin-like proteins (BDLPs) [33], guanylate-binding proteins (GBPs) / atlastins [34], EPS15 homology domain-containing proteins (EHDs) [35], Mitofusins (MFN proteins) [36], optic atrophy

10

protein 1 (OPA1) [37], and dynamin 1-like protein (DNM1L) [38], which is investigated in the present study.

All of these proteins have similar domain architecture (Figure 06). The most conserved domain is the G domain which is an extended form of the canonical G domain fold observed in Ras and many other G proteins of the TRAFAC class. It consists of a central mixed β-sheet surrounded by several α-helices at both sides [39]. Compared to the canonical Ras-like G domain fold, additional α-helices and β-strands are present in the G domain of dynamin superfamily proteins. Furthermore, there are minor variations present within the family. Typically the G domain contains a set of conserved sequence elements which are (in order of appearance in the sequence): **G**xxxx**GKS**/T, **T**, **D**xx**GQ**/H/T, T/N**K**x**D**, C/S**A**K/L/T (where x stands for any amino acid and invariant residues are in bold) [29]. These conserved structural motifs are referred to as G motifs and are by convention named G1 - G5 [40]. With the exception of G5, these motifs are conserved among all G proteins. Members of the dynamin superfamily of G proteins contain a partially invariant asparagine and
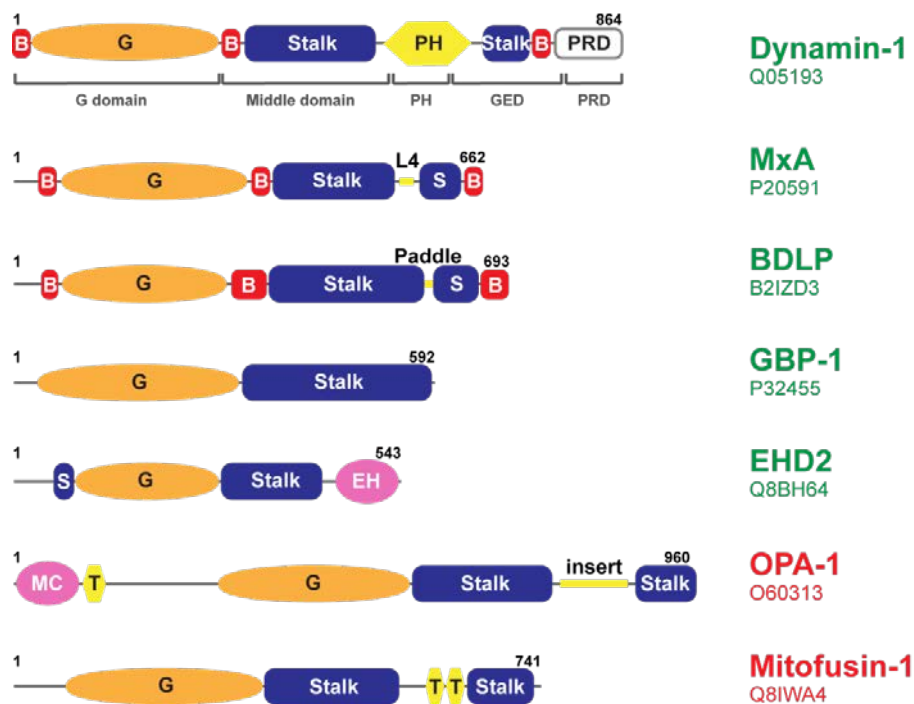
Figure 06: Domain architecture of selected dynamin superfamily proteins. Structure-based domain architecture of the indicated proteins of the dynamin superfamily as they are described in the following chapters (see text). Green names = structure available, red names = no structural data available. The first and the last residues are labeled. For dynamin the classical predicted domain assignment is shown below. B = bundle signaling element, G = G domain, GED = GTPase effector domain, L4 = loop 4, PH = pleckstrin homology domain, PRD = proline rich domain, S = stalk, EH = Eps15 homology domain. MC = mitochondrial targeting sequence. The distinct protein domains are explained in the next chapters (see text). Figure courtesy of Katja Faelber (modified).

arginine at positions roughly equivalent to those of the G5 motif [41]. The G1 motif is also referred to as phosphate-binding loop (P loop), whereas G2 and G3 are also termed switch I and switch II, respectively. Nucleotide binding is predominantly mediated via interactions of the P-loop with the α- and β-phosphates of the guanine nucleotide and of the G4 motif with the nucleotide base. In contrast, switch I and II contain the key residues that trigger the conformational changes after GTP hydrolysis [39]. The above mentioned extensions within the G domain are located between the G2 and G3 and downstream the G5 motif and are supposed to fulfill additional regulatory functions [41, 42]. A common feature of the G domain of dynamin superfamily proteins is the ability to dimerize across a conserved interface - the G interface (see later). The G domain of dynamin superfamily proteins is followed by additional helical domains - termed stalk and bundle signaling element (BSE) - which mediate self-assembly. These domains vary considerably in length between different dynamin members and in some cases the stalk is an extended single domain including the BSE. Furthermore, the stalk is intersected by long insertion or discrete domains in some cases. Consequently, the sequence identity within these domains is very low. However, structural comparisons show significant similarities of the domain architectures of the different dynamin proteins.

During the last decade researchers have made amazing progress regarding our understanding of the molecular architecture of dynamin superfamily proteins. Available structures of five dynamin superfamily members show that the sequence-derived domain boundaries of these proteins do not correspond to the structural domains (Figure 06) and reveal interesting mechanistic insights into the mode of action and assembly of these proteins. The following chapters will outline the current state of knowledge of selected proteins of the dynamin superfamily pointing out their specific molecular architectures and functions.

1.3.1. Dynamin

1.3.1.1. Dynamins are key players in clathrin-mediated endocytosis

Dynamin is the founding member of the dynamin superfamily of large G proteins. The first insights into dynamin function were related to a temperature-sensitive paralytic phenotype of a *Drosophila melanogaster* mutant discovered in the early 70s. The phenotype was termed *shibire*, after the Japanese word for numbness [43]. Soon it

was discovered that synaptic terminals of *shibire*-flies exhibit drastic accumulation of many clathrin-coated "collared pits" on the plasma membrane near presynaptic sites concomitant with a dramatically decreased number of neurotransmitter-filled synaptic vesicles in the presynaptic elements [44, 45]. These findings suggested the *shibire*-encoded protein to be of fundamental importance in clathrin mediated endocytosis (CME). The term "dynamin" was then, in the late 80s, characterized by Shpetner and Vallee. They co-purified dynamin with microtubules out of calf brain and speculated about a neuronal role of dynamins in "bridging microtubules and generate force between them", so they chose the name dynamin, the Greek word for force [46]. They also proved later that dynamin exhibits a microtubule-associated enhancement of its GTPase activity [47]. Soon after the isolation of calf dynamin, the corresponding locus was identified in the rat genome [48]. Sequence analysis revealed 81 % identity to the *shibire* gene. Since then, dynamin was implicated to be important for brain function. Today we know that dynamin exhibits three homologs in mammals. Dynamin 1 and -3 exhibit a tissue-specific expression pattern in brain, lung, heart or testis, whereas dynamin 2 is ubiquitously expressed [49]. Dynamins are found in almost all eukaryotes and are involved in a number of membrane deforming events most notably budding off clathrin coated vesicles (CCV) during CME. Furthermore dynamins were found to be involved in budding off caveolae, and during phagocytosis and podosome formation (Figure 05).

In solution dynamin is predominantly tetrameric, whereas the presence of appropriate membrane templates promotes oligomerization into helical structures leading to tubulation of the underlying membrane template *in vitro* [50-52]. Takei and colleagues observed a similar ring-like dynamin coat at the neck of CCVs *in vivo* [53]. Once assembled the relatively moderate GTPase activity of dynamin is stimulated 100-fold [54, 55]. GTP hydrolysis, in turn, results in conformational changes in the dynamin oligomer leading to vesicle scission (see later) [56-58]. Monomeric dynamin has a size of approximately 100 kDa and is composed of a G domain, a BSE, a stalk (introduced in 1.3), a pleckstrin homology (PH) domain, and a proline rich domain (PRD). Given dynamin's central role in neurotransmitter uptake during CME, elucidation of the underlying molecular mechanism leading to vesicle budding off the plasma membrane is of greatest interest to many researchers. Hence, much effort was put into deciphering the structure of this interesting protein. The next chapters will outline available structural, mechanistic and functional data of dynamin.

1.3.1.2. The G domain and the bundle signaling element

The first insights into a part of the dynamin structure was accomplished with artificial hetero-fusion proteins of the dynamin G domain fused to the myosin II catalytic domain of *D. discoideum* in the nucleotide-free and GDP-bound conformations [42, 59]. The architecture of dynamin's G domain resembles that of classical Ras-like G proteins with conserved nucleotide-binding motifs G1-G4 and the dynamin-specific G5 motif (see 1.3). The GDP-bound conformation showed no large conformational change when compared to the nucleotide-free G domain except for the switch regions [59]. Apart from a few secondary structure elements not present in classical Ras-like G proteins, it is worth noting that the myosin C-terminal helix of the fusion protein packs into a hydrophobic groove that is formed by conserved residues of the N- and C-terminal helices of the dynamin G domain forming a three helical bundle (Figure 07A). Based on this structure it was suggested that the myosin helix mimics an intermolecular domain interaction of the C-terminal GTPase effector domain (GED) with the G domain. This hypothesis was supported by previous findings which showed that GED is important for dynamin's assembly-stimulated GTPase activity [60] and by the observation that the C-terminal helix of the dynamin G domain is required for interactions with the GED [61]. To further prove this hypothesis a homo-fusion protein comprising dynamin's G domain and the C-terminal end of its GED was designed termed minimal GTPase GED fusion protein: GG [62]. Biochemical
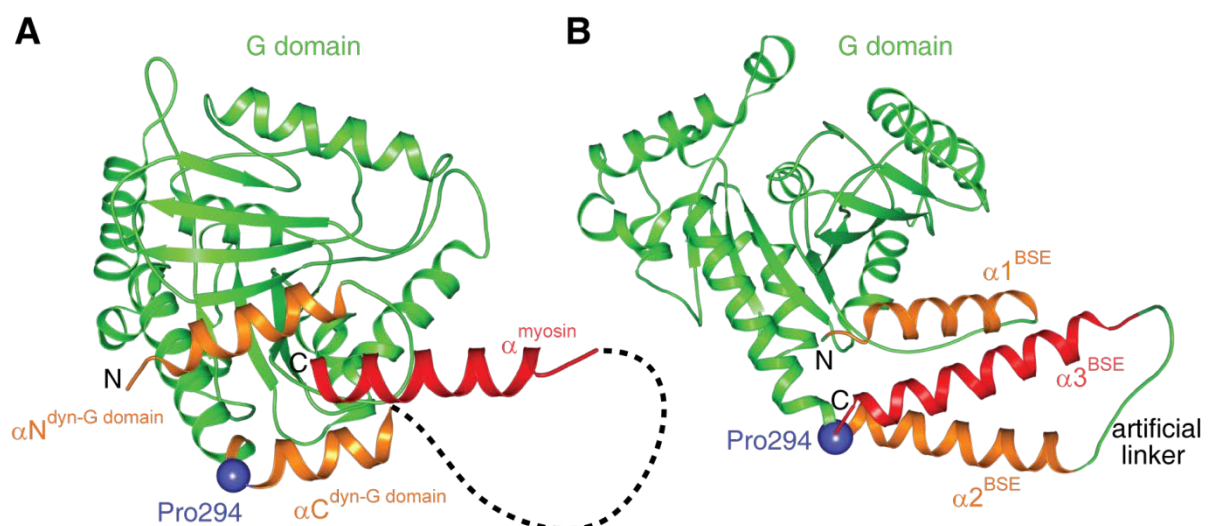
Figure 07: Crystal structures of individual dynamin 1 G domain fusion proteins **A:** Crystal structure of the rat dynamin G domain fused to the myosin II catalytic domain (PDB ID: 2AKA). The rat dynamin G domain is colored green, the N- and C-terminal helices of the G domain are colored orange. The C-terminal helix of the myosin II catalytic domain is colored in red. The dotted line indicates the location of the myosin II catalytic domain, which is not drawn for clarity. **B:** Crystal structure of the minimal GTPase GED fusion protein of human dynamin 1 in the presence of GDP·AlF$_4^-$ (not drawn for clarity) (PDB ID: 2X2E). Two helices of the BSE are colored orange. The BSE helix originating from the C-terminal part of the GED is colored red. Pro294 is indicated as a blue sphere. N- and C-termini are labeled.

experiments of that construct confirmed the presence of the G domain-GED interface built by the N- and C-terminal helices of the G domain and the C-terminal helix of the GED. Furthermore it was shown that this interface is crucial for structural integrity of the full length dynamin and that mutations in this interface disrupt assembly-stimulated GTPase activity and impair with dynamin catalyzed membrane fission *in vitro* and *in vivo*. Based on this results the proposed three helical bundle was termed bundle signaling element (BSE) because of its central role during dynamin function [62]. Soon after biochemical characterization of the GG its structure was solved (Figure 07B) confirming the proposed architecture of the BSE as being a three helical bundle connecting the G domain with the rest of the protein - the so-called stalk (see 1.3.1.5) [63]. Furthermore, a conserved proline residue (P294, see later) was identified around which the BSE was proposed to swing as a compact domain upon GTP hydrolysis dependent conformational changes.

1.3.1.3. G domain dimerization is crucial for dynamin function

Interestingly, the GG dimerized in the crystal in the presence of GDP and aluminum tetrafluoride (GDP·AlF$_4^-$), which mimics the transition state of GTP hydrolysis (Figure 08A) [63]. Dimerization occurred via a conserved interface in the G domain - the G interface - with three key intermolecular interactions contributing to the dimer interface: 1) dual *cis*/*trans* coordination of the guanine base by the G4 motif, 2) association of switch I with the "*trans* stabilizing loop" primarily by main chain interactions, and 3) a pair of symmetric salt bridges that anchor the base of the dimer *in trans*. Notably the crystal structure revealed how GTP hydrolysis in dynamin is achieved without a charge- compensating catalytic GAP-arginine which is known to be necessary for GTP hydrolysis in small Ras-like G proteins [64]. In dynamin neutralization of the negative charge between the β- and γ-phosphate of the nucleotide in the transition state is achieved by a sodium ion present in the G interface which coordinates AlF$_4^-$, the β-phosphate of the nucleotide, and switch I. Thus G domain dimerization across the G interface is crucial for dynamin's assembly stimulated GTPase activity. The BSE did not participate in G domain dimerization but structural comparison with nucleotide-free G domain of the hetero-fusion protein construct (see above) revealed a relative movement of the BSE around P294 triggered by GTP hydrolysis. The GG construct was also crystallized in the presence of the non-hydrolysable GTP analog GMPPCP [65] and structural comparison

_____

A

B
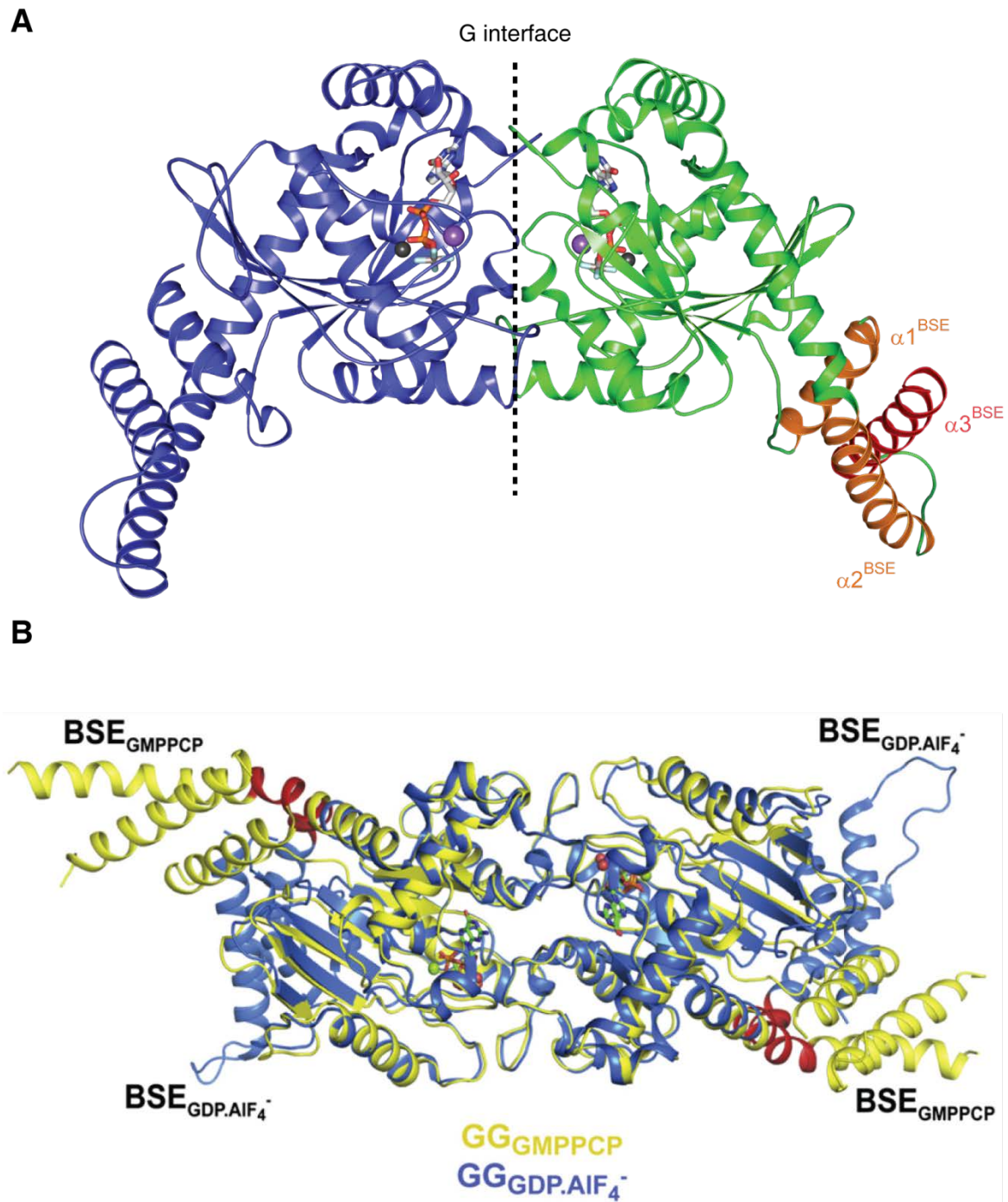
Figure 08: Crystal structures of the human dynamin GG dimers **A:** Human dynamin 1 GG (PDB ID: 2X2E) in the presence of GDP·AlF$_4^-$ showing dimeric arrangement in the crystal via the G interface. One monomer is colored individually in blue. The other monomer is colored according to Figure 07. GDP·AlF$_4^-$ is shown as stick representation. Na$^+$ is shown as purple spheres. Mg^{2+} is shown as black spheres. **B:** Structural superposition of the human dynamin 1 GG dimer in the presence of GDP·AlF$_4^-$ (blue, PDB ID: 2X2E) and GMPPCP (yellow, PDB ID: 3ZYC). The different conformations of the BSE are obvious. The BSE hinge (P294) is colored red. Figure B taken from [65].

between the different GG and G domain fusion protein structures confirmed major GTP hydrolysis dependent structural re-arrangements of the BSE relative to the G domain around P294 (Figure 08B). The respective region was termed hinge region. These findings confirmed the BSE as being a flexible domain transducing a "powerstroke" upon nucleotide-binding and hydrolysis important for dynamin's membrane-remodeling activity [65].

1.3.1.4. Dynamin's PH domain mediates lipid binding

The pleckstrin homology (PH) domain was first identified in pleckstrin and later also in other proteins mediating intra-cellular signaling [66]. It is a globular domain composed of one α-helix and seven β-strands and three lipid-binding loops pointing
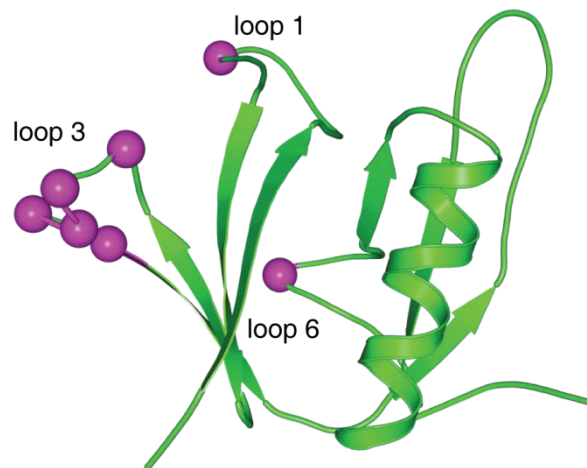
Figure 09: Crystal structure of the PH domain from human dynamin 1 (PDB ID: 1DYN). The residues responsible for lipid binding are shown as magenta-colored spheres.

towards the solvent [67]. The PH domain has some specificity for phosphatidylinositol 4,5-bisphosphate (PIP2) which is found mainly at the plasma membrane. This is one of the reasons why dynamin is acting exclusively at the plasma membrane and not at internal membranes. The PH domain intersects the stalk between α-helix 3 and α-helix 4 (see below).

1.3.1.5. The stalk is the central assembly hub for dynamin oligomerization

Recently, the structure of dynamin 1 ΔPRD was solved by two independent labs [68, 69]. The structure revealed differences between the classic sequence-derived domain assignment and the structure-based domain arrangement (Figure 10A). The

MD and the N-terminal part of the GED form the stalk whereas the C-terminal part of the GED together with the N- and C-terminal helices of the G domain form the BSE, confirming previous findings of the BSE-G domain architecture. Furthermore, two loops and two conserved proline residues (P32 and P294) connecting the BSE with the G domain and the stalk were proposed to serve as flexible hinges (hinge 1 and hinge 2, respectively) allowing for dynamic movement of the G domain, BSE, and stalk relative to each other, supporting the "powerstroke" hypothesis.

The structure revealed the stalk as being the central element for oligomerization into long filaments (Figure 10B). This is in agreement with previous findings on MxA [50]. The stalk is composed of an antiparallel four-helix bundle which is intersected by the PH domain (see 1.3.1.4). A highly conserved central stalk interface (interface 2) is responsible for dimerization leading to a X-shaped dimer. Mutations in this interface render the protein insoluble [68]. In the crystals, two additional conserved stalk interfaces (interface 1 and -3) mediate further oligomerization of dynamin dimers into linear filaments suggesting that that oligomerization is mediated via these two interfaces *in vivo*. Interface 1 was observed only in the structure of Ford *et al.* and is predicted to be less stable than interface 2, tolerating different angles between two stalk dimers (see below). Interface 3 is predicted to involve the unresolved loops L1N^S and L2^S at the tip of the stalk. Mutations in interface 3 were shown to interfere with higher order oligomerization, liposome binding and liposome-stimulated GTPase activity [68]. Furthermore, Faelber *et al.* reported a mutation in interface 3 (IHGIR395-399AAAAA) leading to dimeric distribution of dynamin in solution. Molecular dynamic simulations suggested that both, interface 1 and -3 are quite flexible allowing for adjustments of the angle between the dynamin dimers which might be needed to regulate the diameter of the dynamin helical oligomer to adopt to lipid templates of different diameter [68]
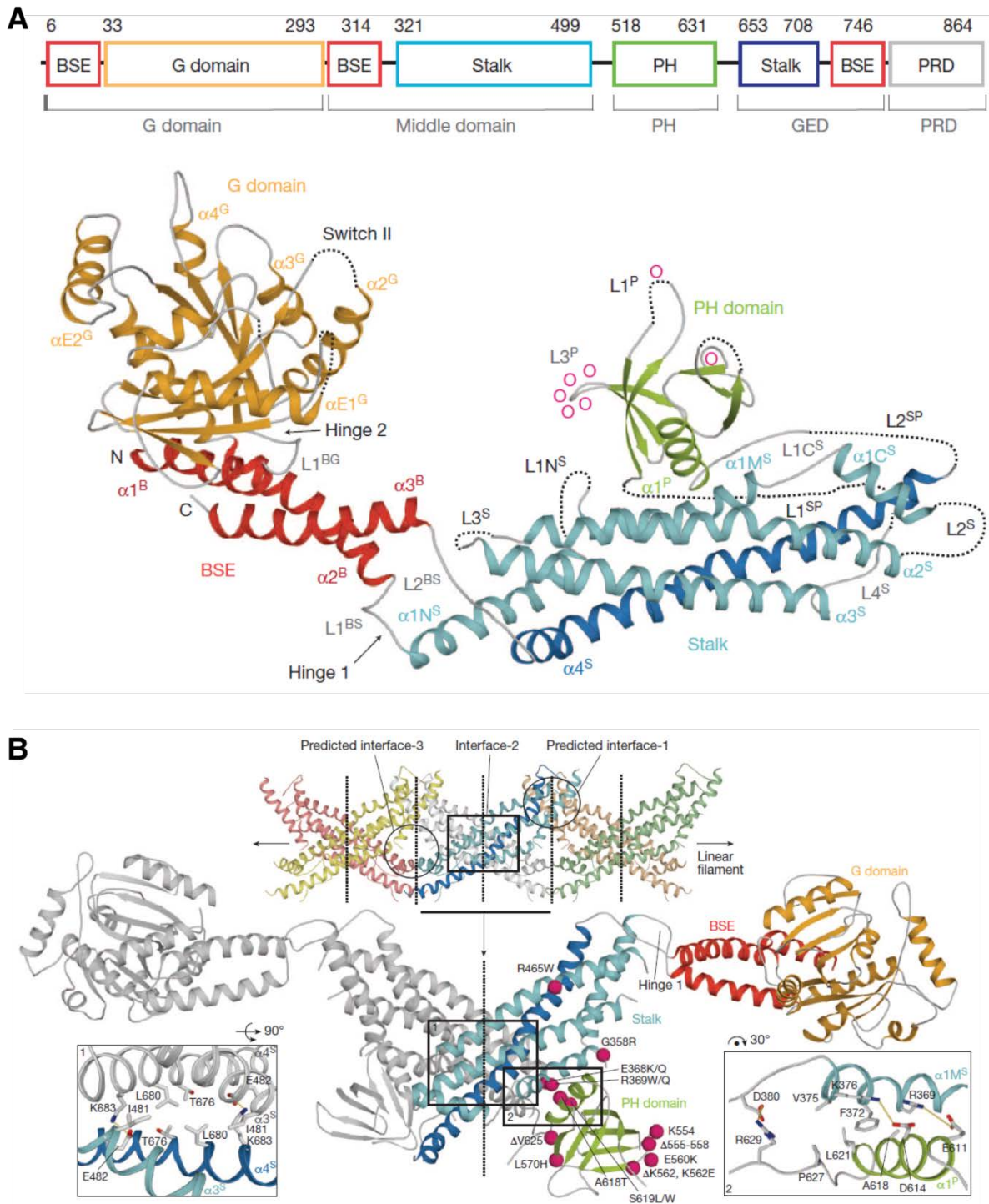
Figure 10: Crystal structure of human dynamin 1 ∆PRD (PDB ID: 3SNH). **A:** Structure of the dynamin 1 ∆PRD monomer and its domain diagram above showing structural domains and the old sequence-derived domain assignment below. Domains are colored as depicted in the figure. **B:** Structure of the dynamin 1 ∆PRD dimer. The upper panel shows the stalks only whereas the lower panel shows one dynamin 1 ∆PRD dimer. One monomer is monochrome the other one domain-colored as in A. Disease-related dynamin 2 mutations are indicated with pink spheres. Figures taken from [68].

_____

1.3.1.6. Regulatory functions of the stalk
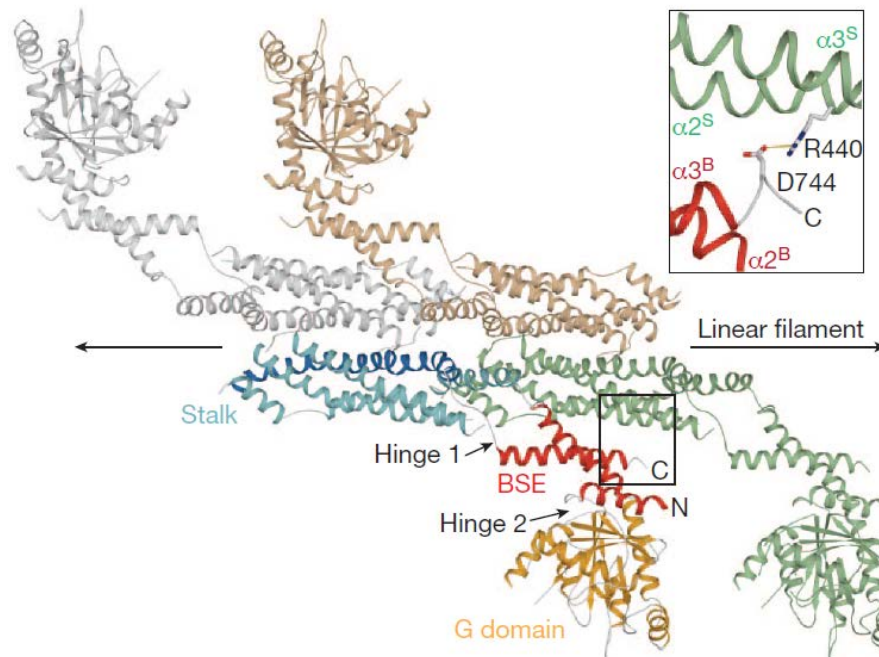
Figure 11: Interaction of the dynamin 1 ΔPRD BSE with the neighboring stalk. Top view on the dynamin 1 ΔPRD tetramer (PDB ID: 3SNH). The PH domain are not drawn for clarity. The insert shows a close-up view of the intermolecular BSE-stalk interaction (a salt-bridge).

The stalk mediates inter- and intradomain interactions controlling dynamin's activity. In the crystals, the PH domain binds to the stalk via another conserved interface involving α1 of the stalk and α1 of the PH domain (Figure 10B). This interface was shown to be important for higher-ordered assembly and basal GTPase activity. It was proposed that this interface may have an auto-inhibitory function [68].

Furthermore, a salt-bridge was found located between α-helix 2 of the stalk (R440) and the C-terminal and of the BSE (D744) of the neighboring, parallel dynamin dimer (Figure 11). This interaction was proposed to have a regulatory function as mutations in this interface lead to increased rates of dynamin-mediated endocytosis *in vivo* [68].

1.3.1.7. Functional models of dynamin's mechano-chemical action

Fitting of the dynamin 1 ΔPRD structure in the cryo-EM map of dynamin 1 [41] suggested that adjustments in stalk interfaces 1 and -3 allow bending of the oligomer and helix formation (see 1.3.1.5) [68, 69]. Furthermore, the EM-fit supported the idea of G domain dimerization across the G interface which involves G domains of adjacent rungs of the helix (Figure 12A). The PH domains mediate contact to the membrane.

Three popular and widely debated models try to explain the mechano-chemical action of dynamin: the "constrictase" [52], "popase" [55], and "twistase" [58] model. In a convincing model unifying available structural and functional data, Faelber and colleagues argue that dynamin is recruited in the GTP-bound state to the bud neck *in vivo* [70]. Intra- and intermolecular domain interactions between the stalk and the PH domain and the stalk and the BSE, respectively (see 1.3.1.6), are released upon membrane binding. This enables recruitment of more dynamin subunits (tetramers), resulting in a right-handed helical oligomer around the neck of the vesicle (Figure 12B). This oligomerization most notably involves the central stalk interface 2 and predicted interfaces 1 and -3. After one helical turn the G domains of neighboring filaments are proposed to dimerize via the G interface, thereby mediating contacts between neighboring dynamin filaments. G domain dimerization leads to opening of
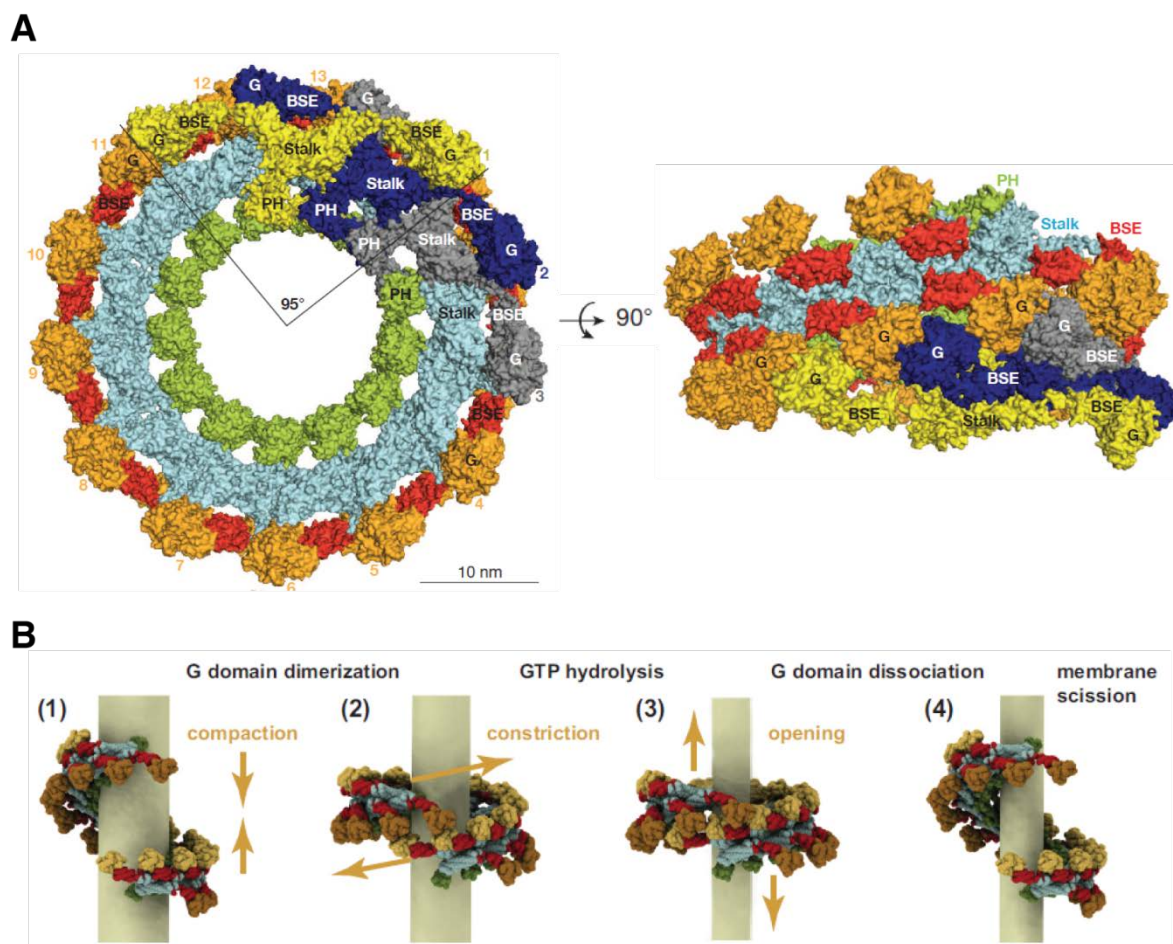
Figure 12: Functional model of dynamin's mechano-chemical action. **A:** Model of the oligomerized dynamin 1 helix in the constricted state in top and side view. Three dimers (1-3) are uniformly colored. The other dynamin molecules are colored according to their structural domains. G domain orange, BSE red, stalk light blue, PH domain, green. One turn is completed by 13 stalk dimers. G domain dimerization occurs between dimer (i) and dimer (i+10). Figure taken from [68]   **B:** Model for dynamin action during membrane scission. For explanation, see text. Figures taken from [68] and [70].

the flexible BSE-G domain interaction, inducing GTP hydrolysis which is, in turn, followed by a conformational change moving the BSE back to the G domain. Repeated cycles of this re-arrangements in a nut runner-like manner might act as power strokes pulling neighboring filaments of the helix along each other, thereby constricting the underlying membrane tubule [65, 69]. Constriction, in turn, might be accompanied by a right-handed twisting of the dynamin filaments, which was indeed observed before [58]. The torque of twisting dynamin oligomers was estimated to be ~700 - 1000 pN·nm during constriction which is amazingly high compared to other known molecular torques [71]. It is reasonable that multiple rounds of GTP binding and hydrolysis might occur prior to breakage of the budding vesicle from its highly curved neck [70]. It was proposed that fission occurs spontaneously at the edge between the dynamin coated neck and the vesicle because of a considerable change in membrane curvature in this region. This would lead to an increase of the local membrane elastic energy which reduces the energy barrier for fission making spontaneous fission possible [71].

However, to fully understand the complete scission process of dynamin nucleotide-dependent conformational changes have to be investigated on a molecular level, ideally with a nucleotide-bound structure of full length dynamin which is not available so far. Also, the disassembly process needs to be better understood. Even more intriguing is the fact that other members of the dynamin superfamily most likely use similar mechanisms to accomplish completely different functions. An example is given in the next chapter.

1.3.2. Myxovirus resistance (Mx) proteins

1.3.2.1. Mx proteins mediate antiviral host response

In vertebrates, Mx proteins are key components of the innate interferon (IFN)-induced antiviral host response [32]. Two human Mx homologs are known, termed MxA and MxB [72]. Their gene expression is stimulated by type I and type III IFNs [73]. Upon expression, Mx proteins exhibit a powerful antiviral activity against a broad range of viruses, including members of the Orthomyxovirus family (e.g. Influenzavirus, Thogotovirus, and Dhorivirus) and the Bunyavirus family (e.g. Hantavirus and Rift valley fever virus) [74]. Upon viral infection, Mx proteins redistribute to sites of viral replication and inhibit further propagation of viral particles

[75, 76]. The exact molecular mechanism mediating the antiviral capacity of MxA is not well understood at the moment. However, based on the full-length structure of human MxA a functional model was proposed which is introduced in the following chapters.

1.3.2.2.   Different functions - similar structures: MxA and dynamin 1

Mx proteins share many features with classical dynamins. They bind, for example, guanine nucleotides with low affinity and exhibit assembly-stimulated GTPase activity while oligomerizing in a concentration dependent manner. In solution, they exhibit a predominantly tetrameric distribution at low and medium concentrations [50]. Furthermore, they bind to liposomes and induce liposome tubulation *in vitro* [77, 78]. Like dynamin, MxA is composed of an N-terminal G domain, a BSE, and a stalk, thus, its structure also deviates from the sequence-derived domain prediction (Figure 13) [79]. Sharing only ~20 % sequence identity, the molecular domain architectures of dynamin 1 and MxA are almost identical (compare Figure 10A + Figure 13). At the equivalent position of the PH domain in dynamin a predicted substrate binding loop ($L4^S$) is located in MxA. As in dynamin, the G domain, BSE,
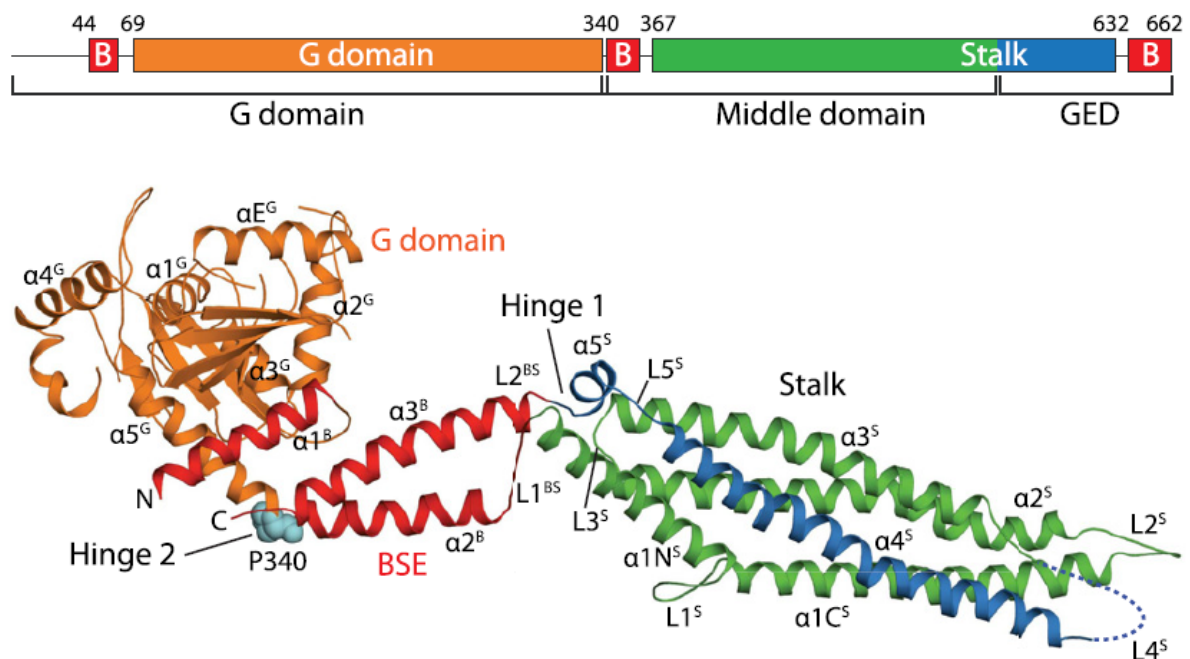
Figure 13:   Structure of the MxA monomer (PDB ID: 3SZR). The upper panel shows the structure-based domain representation with the old sequence-derived domain boundaries given below. The lower panel shows a ribbon-type representation of an MxA monomer with its domains colored as depicted. N- and C-termini as well as secondary structure elements are labeled. The invariant proline residue (P340) is shown as spheres. Figure take from [79].

and stalk are connected via 2 hinge regions, allowing for flexibility of these domains relative to each other. Hinge 1 was shown to be crucial for oligomerization, GTPase activity, and antiviral activity of MxA [79]. Hinge 2 comprises the conserved proline residue (P340) which is equivalent to P294 in dynamin 1 (compare Figure 07 + Figure 13).

1.3.2.3. The MxA stalk mediates oligomerization and regulatory function

In the crystals, MxA forms linear oligomers mediated by three distinct, conserved interfaces (interface 1, -2, and -3) and the putative substrate binding loop (L4) (Figure 14) [50, 79]. This arrangement is similar to that of the linear oligomeric filaments in the dynamin crystal (compare Figure 10B + Figure 14). Mutations in either of the stalk interfaces or deletion of L4 disrupts the MxA tetramer or oligomer, resulting in dimeric (mutations in interfaces 1 or -3) or monomeric (mutations in interface 2) distribution in solution. Furthermore liposome binding is disturbed by disrupting the stalk interfaces and by introducing mutations in the predicted substrate-binding loop L4 [50]. Like for dynamin 1, interface 1 is proposed to be flexible allowing for rotation of dimeric MxA stalks assembled via interface 2 (Figure 14). Similar to dynamin 1, the BSE and the stalk of the neighboring parallel MxA monomer form an interface via a number of polar contacts. Mutations in this interface were shown to interfere with oligomerization and the antiviral function of MxA, suggesting that dynamin and MxA are regulated similarly via these stalk-BSE interactions.
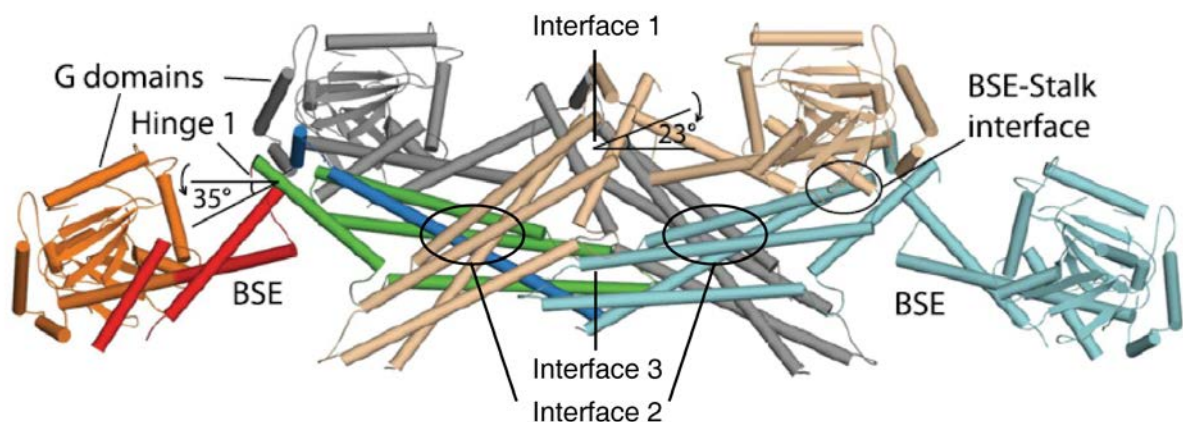
Figure 14: MxA tetramer constituting the building block of the ring-like oligomer. Individual monomers are colored monochrome with one exception where the G domain is colored in light orange, BSE in red, stalk in green and blue (blue = part of the GED). Compare to Figure 10B. Figure modified from [79].

1.3.2.4. The MxA stalk mediates assembly in rings rather than helices

Based on the full-length structure of MxA and on electron microscopy studies showing ring-like MxA oligomers around tubulated liposomes [80], Gao and colleagues proposed a molecular model for the antiviral activity for MxA involving the conserved interfaces 1, -2, and -3 and the BSE-stalk interface (Figure 15) [79]. According to this model, MxA oligomerizes in rings clamping around the viral ribonucleoparticles. Ring formation is mediated via the flexible interface 1 (see 1.3.2.3). The G domains are proposed to be located above the stalk of the neighboring molecule in the ring whereas loops L4 are pointing towards the inside of the ring. Nucleotide-dependent dimerization of the G domains across the conserved G interface is proposed to involve neighboring ring-filaments. Upon GTP-hydrolysis, conformational changes of the G domain could be transmitted to the stalk of the neighboring molecule via the BSE-stalk interface. Global GTP-dependent conformational changes of the whole oligomer might, in turn, disintegrate or sequester infective virus particles in the early stage of the viral assembly. It is noteworthy to mention that a similar oligomerization model was proposed for dynamin 1 (see 1.3.1.7), although dynamin 1 was supposed to oligomerize in a right-handed helix rather than into rings. Thus, completely different cellular functions might be based on similar molecular principles.
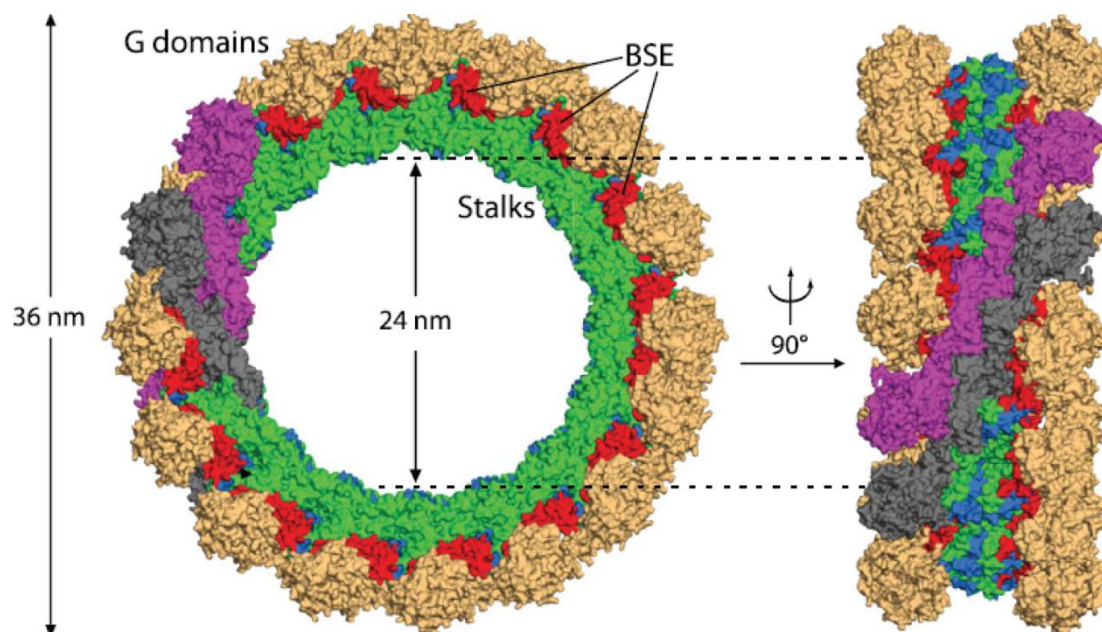
Figure 15: Model of the ring-like MxA oligomer. Colors as in Figure 14. Two MxA dimers are individually highlighted in magenta and gray. Figure modified from [79]. For explanation, see text.

1.3.3. Bacterial dynamin-like proteins (BDLPs)

Many Eubacteria have genes encoding for putative dynamin-related proteins which are termed BDLPs. Their sequence identity to dynamin is low and most of the BDLPs are not well characterized in terms of structure and function. However, it was suggested that BDLPs mediate bacterial membrane fusion rather than scission [81]. Microscopy-based subcellular localization studies of the BDLP from the cyanobacterium *Nostoc punctiforme* (from here on referred to as *np*BDLP) revealed punctate distribution to the cell periphery, predominantly to the cell membrane [33]. In the same study it was shown that *np*BDLP in the presence of the non-hydrolyzable GTP analog GMP-PNP is capable of binding to liposomes composed of bacterial lipids and to oligomerize in a regular helical pattern around these lipids, tubulating them in a similar fashion like dynamin 1 (see 1.3.2) and MxA (see 1.3.1) [33].

In contrast to dynamin 1 and MxA, nucleotide-free *np*BDLP is monomeric in solution while dimerizing in the presence of GDP [33]. The crystal structure of the nucleotide-free and the GDP-bound *np*BDLP revealed a different domain organization compared to dynamin 1 [68] or MxA [79] (Figure 16A, B). The protein is composed of an N-terminal, globular G domain and two additional domains termed neck and trunk.
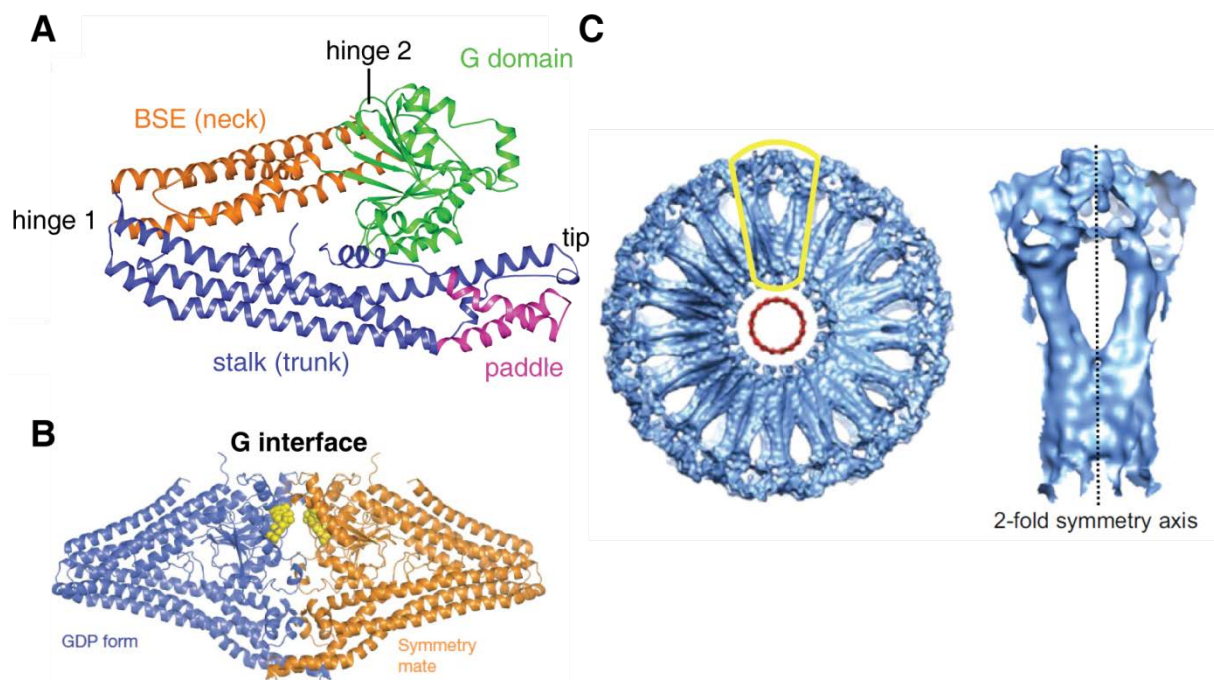
Figure 16:   Different structures of *np*BDLP.   **A:** Structure of the nucleotide-free BDLP monomer (PDB ID: 2J69). Domains are indicated. **B:** Dimerization of GDP-bound *np*BDLP (PDB ID: 2J68) in the crystal across the G interface. GDP is shown as yellow spheres. **C:** Electron density of the GMP-PNP-bound *np*BDLP tube reconstruction (PDB ID: 2W6D). The asymmetric unit is highlighted in yellow. Lipid core is red. Figures B and C modified from[33] and [82], respectively. For explanation, see text.

Both, neck and trunk are antiparallel four-helix bundles reminding of the BSE (neck) and stalk (trunk) of dynamin 1 and MxA. Neck and trunk are bent relative to each other around a flexible loop region connecting neck and trunk, termed hinge 1. A similar hinge was also found to connect the BSE with the stalk in dynamin 1 (see 1.3.1.5) and MxA (see 1.3.2.2) [68, 79]. The G domain bends towards the neck around 3 proline residues without forming extensive contacts to the neck. The corresponding region is partially conserved and termed hinge 2, which is also present in dynamin 1 and MxA (see above). The trunk is organized like the stalks of dynamin 1 and MxA, containing three helices from the MD and one helix from the GED. The regions of the trunk equivalent to the substrate binding loops of MxA or the PH domain of dynamin 1 are termed tip and paddle in BDLP and are predicted to mediate membrane association. The paddle is a two helix motif located at the distal end of the stalk (Figure 16A).

BDLP dimerized via the conserved G interface in the crystals in both, nucleotide-free and GDP-bound conformations (Figure 16B). Interestingly, the GDP-bound BDLP dimer exhibits a larger dimer interface covering the nucleotide-binding site in a similar way to that of the human GBP1 (see 1.3.4) [83]. Upon GDP binding the tip region also undergoes a remarkable conformational change, most likely facilitating crosstalk between the G domains within the dimer. Cryo-EM reconstructions of the BDLP oligomer in the presence of GMP-PNP revealed a tightly packed helical arrangement around lipid tubules with a diameter of 50 nm (Figure 16C) [82]. The outer periphery ("coat") of the asymmetric unit contained globular densities in which G domain dimers were modeled. Compared to the architecture in the crystal structure, neck and trunk have undergone dramatic rearrangement relative to each other. The trunk bent around hinge 1 to form an extended linear neck to trunk domain. Accordingly, neck and trunk have been modeled in a linear fashion into the cryo-EM density ("spokes") with the hydrophobic paddle facing the lipid tubule.

However, it is not clear how such a huge domain rearrangement is driven by GTP binding and/or hydrolysis *in vivo*. Furthermore, the function of BDLP in cellular context remains to be exactly elucidated.

1.3.4.   Guanylate-binding proteins (GBPs)

GBPs are inducible by interferons like MxA proteins (see 1.3.2.1). They were originally found as guanylate-binding proteins in extracts of human fibroblast cells treated with IFNs, γ-IFN being the most effective one. The proteins were identified using GTP-, GDP-, and GMP-bound agarose beads to which they bound effectively [84, 85]. GBPs comprise seven members in humans [86]. They have a different antiviral spectrum than Mx proteins (see 1.3.2) [31]. hGBP1 was shown to mediate antiviral activity to Vesicular Stomatitis Indiana virus (causing zoonotic *Stomatitis vesicularis*) and Encephalomyocarditis virus (causing *Encephalomyocarditis*) [87]. Furthermore GBPs were shown to have an inhibitory effect on endothelial cell proliferation [88]. Like all dynamin proteins, GBPs are stable in absence of guanine nucleotides and exhibit a low affinity for them [89]. They also show a high concentration-dependent basal GTPase rate of ~80/minute and nucleotide-dependent dimerization [34]. A unique feature of GBPs is their ability to hydrolyze GTP to GDP and GDP to GMP [90, 91]. The physiological function of GDP hydrolysis is unknown.

The crystal structure of hGBP1 was the first high resolution full length structure of a dynamin protein [34]. hGBP1 is composed of a large G domain (LG) and an elongated α-helical stalk arranged as a tight antiparallel helical bundle comprising the MD and the GED (Figure 17). The G domain exhibits the typical dynamin superfamily fold with some exceptions. There are insertions in switch I (see below), between switch II and α2, and between β6 and α5. Most notably the G4 motif is altered (instead of missing as predicted by sequence analysis) to the sequence TLRD which is conserved among GBPs. The most dramatic difference to other dynamin superfamily members is the presence of the so-called "phosphate cap", a switch I insertion undergoing conformational change upon nucleotide binding and responsible for the moderate affinity of GBPs towards GMP [34, 83]. In the crystals, hGBP1 dimerized via the conserved G interface similarly to other dynamin superfamily members (see e.g. 1.3.1.3). Thereby, an arginine finger and a serine are re-oriented promoting GTP hydrolysis [83, 92].

Compared to other dynamin superfamily proteins, the helical stalk is much more elongated. The GED entity of the stalk contains two antiparallel helices of which one is extremely long (118 Å). The C-terminal end of the last GED helix contains the prenylation-recognition CaaX motif. The MD entity of the stalk contains five antiparallel α-helices and is connected with the LG via a loop between α6 and α7

28

containing the conserved proline residue constituting a flexible hinge equivalent to hinge 2 in dynamin 1 (see 1.3.1.5) and MxA (see 1.3.2.2). GED and MD are connected via another conserved flexible loop, hinge 1.

Due to the distant relationship of GBPs to other members of the dynamin superfamily, GBPs are insufficient for a global explanation of the hydrolysis mechanism and the mechano-chemical mode of action of the dynamin superfamily. However, a model explaining higher ordered assembly of GBPs is not available at present.
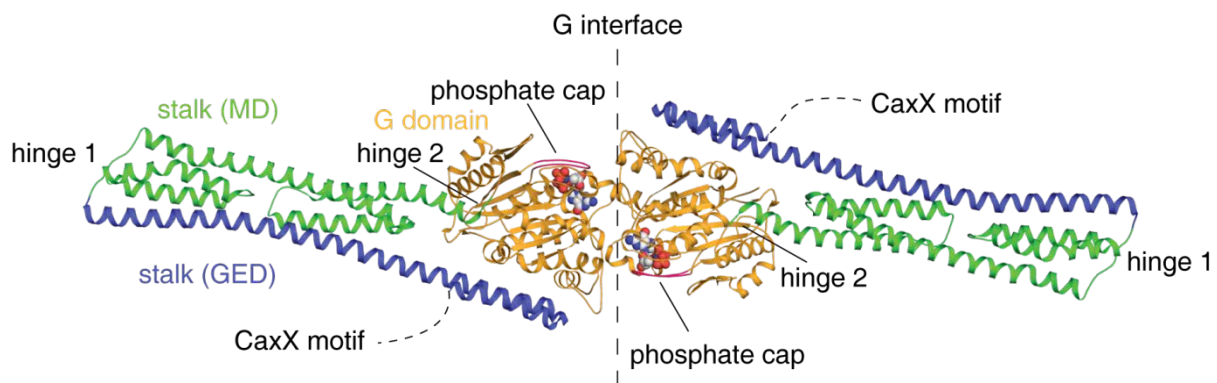
Figure 17: Ribbon-type representation of the GMP-PNP-bound hGBP1 dimer (pdb: 1F5N). The domains, the phosphate cap, the hinges, and the CaxX motif are depicted. GMP-PNP is shown as spheres. For explanation, see text.

1.3.5. Eps15 homology-domain containing proteins (EHDs)

EHDs were recently suggested as new members of the dynamin superfamily despite the fact that they bind ATP rather than GTP [35]. Nevertheless, EHDs share many common features with dynamins such as low affinity for nucleotides, low basal hydrolysis rate, lipid stimulated nucleotide hydrolysis, and the ability to tubulate lipids *in vitro* by oligomerizing in ring-like structures around them [35]. Accordingly, EHDs were reported to play a role in clathrin independent endocytosis [93] and endocytic recycling [94, 95] (Figure 05). EHDs have four members in mammals (EHD1-4) and one member in *Drosophila melanogaster*, *Caenorhabditis elegans*, and many parasites (e.g. *Toxoplasma gondii*). Interestingly EHDs exhibit a Eps15 homology (EH) domain known to interact with NPF-motif containing proteins such as PACSIN. In contrast to other dynamin proteins, nucleotide-free mEHD2 is dimeric in solution rather than tetrameric.

In 2007 Daumke and colleagues solved the crystal structure of mouse full-length EHD2 bound to AMP-PNP, a non-hydrolyzable ATP analogue [35]. The protein dimerized in the crystals via a conserved interface in the G domain at the opposite site of the nucleotide-binding pocket. This dimer architecture is different from that observed in other dynamin superfamily proteins. mEHD2 is composed of an N-terminal nucleotide-binding domain (despite ATP binding also referred to as G domain), a stalk, and a C-terminal EH-domain (Figure 18A). The G domain exhibits a G domain fold as typical for dynamin proteins (see 1.3) except for minor structural changes in the G4 motif, responsible for the specificity towards adenine nucleotides rather than guanine nucleotides. The EH domain and the stalk are connected to each other by a 40-residues linker positioning the EH domain on top of the G domain of the opposing monomer. G domain and stalk are linked via a network of extensive contacts. The stalk contains a conserved polybasic stretch at the tip which was shown to mediate liposome-binding [35]. The whole dimer architecture is reminiscent of a scissor with the lipid-binding sites being the tip of the blades.

Daumke and colleagues proposed an oligomerization model for mEHD2 where the highly conserved switch regions within the G domain mediate contacts between different EHD dimers [35]. A similar G domain interaction was observed in BDLP (see 1.3.3) and hGBP1 (see 1.3.4). Accordingly, mutations in the proposed interface
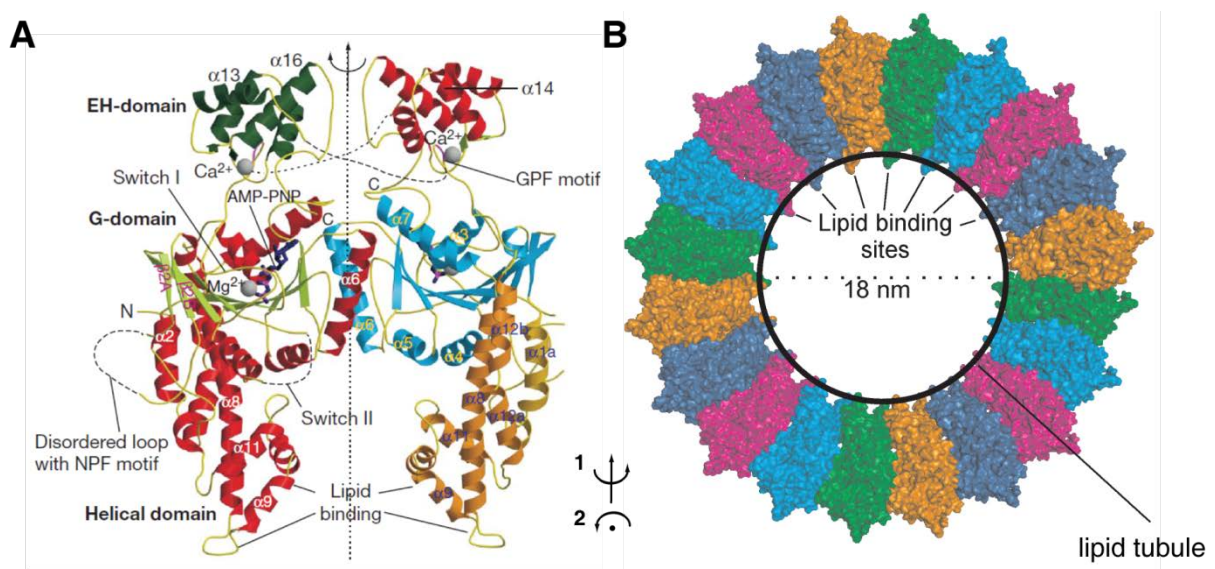
Figure 18:   Structure of EHD2 **A:** Structure of the mEHD2 dimer (PDB: 2QPT). One monomer is colored according to the secondary structure (α-helices in red, β-sheets in light green) and the other according to the domain structure (G domain in blue, helical domain in orange, EH domain in green). AMP-PNP is shown as sticks. Ions are shown as grey spheres **B:** Model of the mEHD2 oligomer. The EH domains point outside the ring whereas the lipid binding sites are pointing ring inwards. Figure modified from [35]. For explanation, see text.

were shown to interfere with lipid-stimulated ATPase activity [35]. It was suggested that such an interaction leads to the formation of a ring-shaped oligomer which exhibits a compact structure with a thickness of about 10 nm and an inner diameter of 18 nm (Figure 18B). This model is consistent with EM studies. In such an oligomer, the lipid-binding sites would point ring-inwards and are believed to create membrane curvature, necessary for membrane remodeling. However, the proposed mEHD2 oligomer remarkably differs from that proposed for dynamin (see 1.3.1.7), MxA (see 1.3.2.4), and BDLP (see 1.3.3).

1.3.6. Mitochondrial fusion dynamins

1.3.6.1. Mitochondrial outer membrane fusion dynamins

Mitochondrial fusion is an exceptionally intricate process. As mitochondria are double-membrane enclosed cell organelles, four membranes have to be coordinated to fuse. The first known mediator for mitochondrial fusion was the dynamin-related protein fuzzy onion (FZO) which was identified as a central key player during mitochondrial outer membrane fusion in *Drosophila* ([36] reviewed in [18]). FZO has two homolog ins mammals, mitofusin (MFN) 1 and 2. Mitochondria in Purkinje neurons of mice lacking MFN 2 are significantly fragmented and fail to distribute within these long neurons leading to their degeneration [96]. Furthermore, it was shown that transgenic mice with dysfunctional mutations in *Mfn1* and *Mfn2* of the skeletal muscle display increased accumulation of mtDNA mutations leading to, for example, loss of respiratory complex functions [97]. In humans, mutations in *Mfn2* were shown to be causative for autosomal Charcot-Marie-Tooth disease type 2a [98]. At the moment there is no structural information of a MFN homolog available so far. Sequence analysis, however, predicts the presence of a N-terminal G domain, a stalk, and a BSE (Figure 06). The stalk is predicted to be interspersed with two transmembrane helices at positions roughly equivalent to the position of the PH domain in dynamin (see 1.3.1.4). These helices are thought to anchor mitofusins to the mom. Lacking any structural data, the molecular mechanism leading to mom fusion is not known at present.

1.3.6.2. Mitochondrial inner membrane fusion dynamins

In mammals, the fusion of the mim is mediated by the dynamin-related protein Optic atrophy protein 1 (OPA 1) (reviewed in [18]). Its yeast homolog is termed mitochondrial genome maintenance protein 1 (Mgm 1). Mutations in OPA1 are implicated with degeneration of retinal ganglion cells and optic nerve, a disease termed Autosomal dominant optic atrophy an eponym for OPA 1. The proteins exhibits a long and a short form both of which are crucial for proper mitochondrial morphology. The short form is produced by proteolytic cleavage of a predicted N-terminal transmembrane segment (TS) and its mitochondrial targeting sequence (MTS). Only the long form is transported into the mitochondrial lumen and its MTS is cleaved afterwards. Long OPA 1 is predicted to be attached to the mim via its TS. Furthermore, OPA 1 contains a predicted G domain and a stalk. The stalk is intersected by a 100 amino acid region which is predicted to be unstructured (Figure 06). No high resolution structure of OPA 1 is available yet.

1.3.7. The mitochondrial fission dynamin 1-like protein (DNM1L)

1.3.7.1. DNM1L is a key player in mitochondrial fission

In the mid-1990s, genetic screens in the budding yeast *Saccharomyces cerevisiae* identified a dynamin-related protein termed Dnm1p. Because of the close relationship to classical dynamins and because of an unsuitable experimental setup it was mistakenly recognized as being important for receptor-mediated endocytic pathway in yeast [38]. Two years later another genetic screen revealed the human homolog of Dnm1p, initially termed DVLP (for Dnm1p/Vps1p-like protein) [99]. The same protein (termed Dymple this time) was identified by another group one year later using a HeLa cell cDNA library [100]. Other groups also found the protein in different screens and termed it either dynamin-like protein 1 (DLP 1), or dynamin-related protein 1 (DRP 1) [101, 102]. Since other proteins are also referred to as dynamin-related proteins (e.g. Mgm 1, Fzo 1) the terms DRP 1 or DLP 1 are misleading. Thus, the name dynamin 1-like protein (DNM1L in mammals, Dnm1 in yeast) was suggested. These terms will be used thorough this study.

Human DNM1L is an 80 kDa mechano-chemical G protein and the closest relative of dynamin (see 1.3.1). It catalyzes the fission of mitochondria (see 1.1.2) [103-105] and peroxisomes [106] and is expressed ubiquitously in all tissues with higher
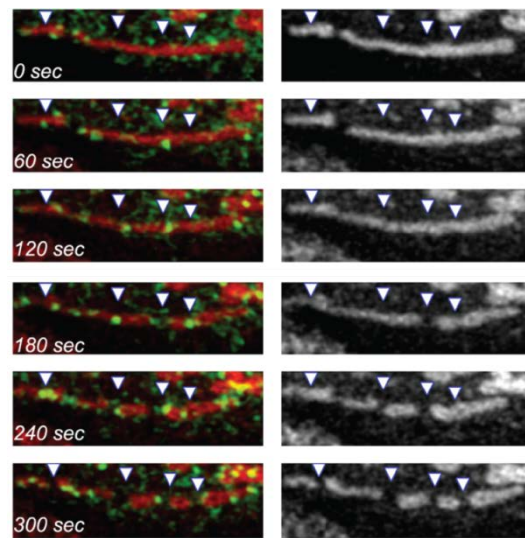
Figure 19: DNM1L mediates mitochondrial fission. Time-lapsed confocal microscopy picture series showing mitochondrial scission events occurring at DNM1L-mom co-localization sites in HeLa cells. Colored pictures show mitochondria in red and DNM1L in green. Corresponding monochrome pictures are shown for better identification of scission sites. Picture modified from [107].

expression levels in heart, brain, and muscle (reviewed in [13]). DNM1L is a cytosolic protein which is recruited to the mom where it oligomerizes at discrete foci. Some of these foci develop into mitochondrial scission sites (Figure 19) [103, 104]. Cells lacking DNM1L contain highly interconnected mitochondria that are formed by an imbalance of mitochondrial fusion over fission. Impaired mitochondrial dynamics caused by dysfunctional DNM1L has been implicated in neurological disorders (see 1.1.3).

1.3.7.2. Recruitment of DNM1L to mitochondria scission sites involves certain adaptor proteins and the endoplasmic reticulum (ER)

In mammals, recruitment to the mom involves the endoplasmic reticulum [108] and is thought to be mediated via adaptor proteins, such as mitochondrial fission factor (Mff) [109], mitochondrial elongation factor 1 / mitochondrial dynamics proteins of 49 and 51 kDa (MIEF1 / MiD49/51) [110, 111], and mitochondrial fission protein Fis1 [112, 113]. For the yeast homologue of DNM1L, Dnm1, recruitment via similar adaptors (Mdv1, Caf4) was shown to nucleate and promote self-assembly of Dnm1 into helical structures, thereby driving membrane scission [114-116]. Knock down of either of these proteins leads impaired mitochondrial fission events with the result of significantly elongated mitochondria in these cells. Furthermore, an exchange of the predicted mitochondrial transmembrane domain with the plasma membrane targeting

_____
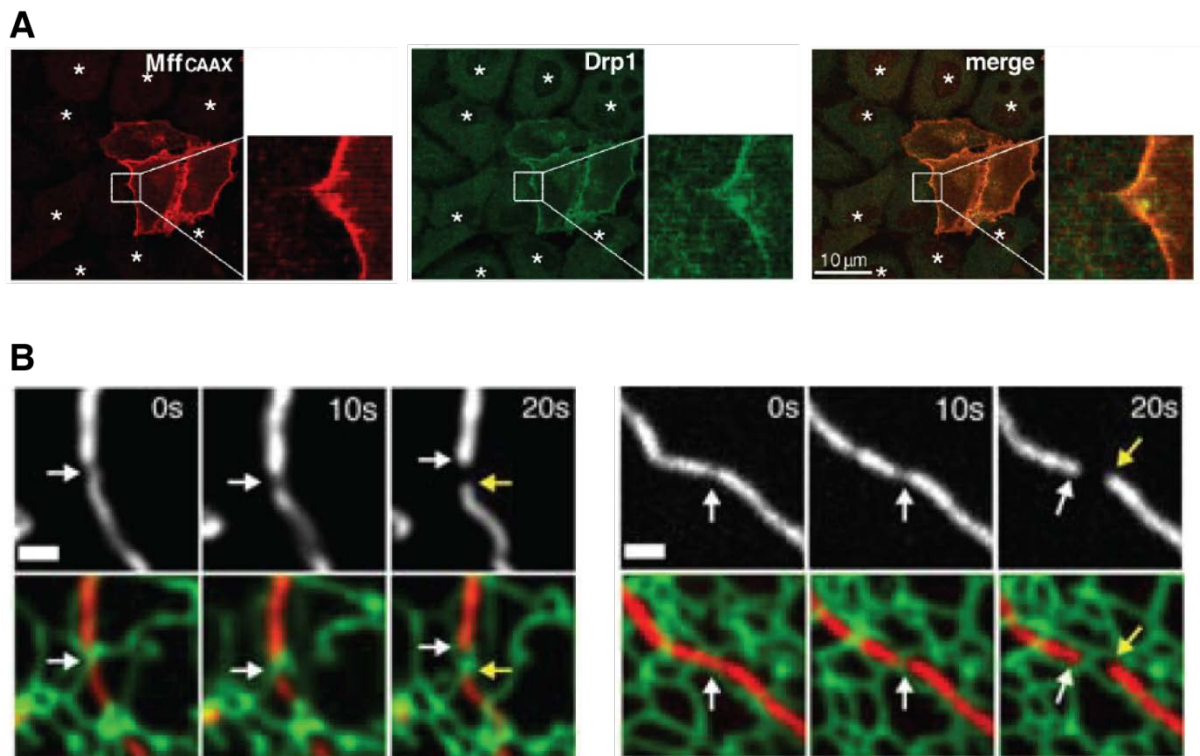
Figure 20:   Adaptor proteins and the ER are crucial for mitochondrial scission **A:** HeLa cells transfected with Mff siRNA and FLAG-Mff-CAXX immunostained with antibodies against FLAG (red) and DNM1L (green, here termed Drp1). Asteriks show FLAG-Mff-CAXX non-expressing cells. Figure taken from [109]. **B:** Two time-lapsed confocal microscopy picture series showing mitochondrial scission sites correspond to ER interaction events in COS-7 cells. Colored pictures show mitochondria in red and ER in green. Corresponding mono-chrome pictures are shown for better identification of scission sites. Picture modified from [108].

CAXX motif in Mff results in localization of both, Mff and DNM1L to the plasma membrane (Figure 20A). However, Mff or a homolog does not exist in yeast. Thus, the recruitment mechanism of DNM1L to the mom seems to be less conserved between yeast and mammals. Another study showed that the mitochondrial scission sites correspond to ER interaction events (Figure 20B) suggesting a strong relationship of the mitochondrial network with the ER.

1.3.7.3. Two-start versus one-start helix

Purified yeast Dnm1 forms highly ordered oligomers around lipid tubules with an average outer diameter of approximately 120 nm, causing liposome tubulation [117, 118]. Electron microscopy (EM) reconstructions of this oligomer in the presence of a non-hydrolyzable GTP analogue showed that Dnm1 assembles as a two-start helix with a helical pitch of 28.8 nm around these tubules, i.e. two distinct helices with a spacing of about 14.4 nm were evident (Figure 21). Upon GTP hydrolysis, lipid

tubules covered by Dnm1 constrict to ~70 nm [118]. In contrast to Dnm1, nucleotide-free dynamin oligomerizes around tubulated liposomes as a one-start helix, with an outer diameter of 50 nm [119, 120]. In the GTP-bound form, this oligomer further constricts to generate an even narrower tubule [41, 56]. To understand these variations, molecular insights into the structure of DNM1L would be of greatest benefit. Furthermore, a high resolution structure is the key to understand the molecular principles regarding the process of mitochondrial division and to understand DNM1L caused mitochondria-associated disease.
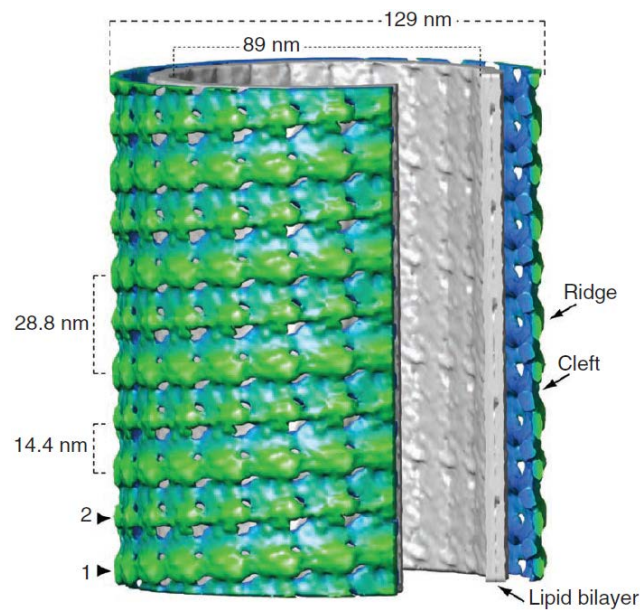
Figure 21:   Cryo-EM reconstruction showing yeast Dnm1 oligomerization around a lipid tubule. For better clarity, a wedge of the tubule was removed. Dnm1 electron density is colored with a radial gradient (the more green the more outside, the more blue the more inside). The lipid bilayer is depicted in grey. The Dnm1 two-start helix is indicated. Picture taken from [118]. For explanation, see text.

1.4.   Scope of this work

At the beginning of this work, it was not clear how large G proteins of the dynamin superfamily mediate such diverse processes like clathrin-mediated endocytosis, antiviral host defense or mitochondrial membrane remodeling processes most notably because high resolution structural data were not available. During the last decade, much effort has been spent to solve the structure of dynamin, the founding member of the dynamin superfamily. However, crystallization trials yielded no crystals suitable for diffraction experiments.

In 2010 the structure of the stalk of human MxA was solved in the Daumke lab. Soon after, the full length structures of dynamin and MxA were reported by the same lab. The structures revealed amazing new insights into oligomerization mechanism and domain architecture of these proteins. Despite limited sequence identity, dynamin and MxA exhibit the same domain arrangement. Two different functional models were proposed for oligomerization of these proteins. While dynamin is believed to oligomerize as a right-handed helix, MxA is proposed to form ring-like oligomers.

A close relative of dynamin and MxA, dynamin 1-like protein, mediates mitochondrial fission events that are crucial for mitochondrial dynamics. Malfunctioning of this process is known to be involved in a wide range of severe diseases. This thesis aims to elucidate the molecular mechanism of the mitochondrial fission process catalyzed by DNM1L. To this end, the following points were addressed. First, despite limited sequence similarity, it is predicted that DNM1L exhibits the same domain architecture as dynamin and MxA, composed of an N-terminal G domain, a BSE, and a stalk. Is that true? Furthermore, DNM1L contains a ~100 amino acids region of unknown function - the B insert - at positions equivalent to that of the PH domain in dynamin and the predicted substrate binding loop in MxA. What is the function of this region? Strikingly, all mutations reported for DNM1L which are known to be causative for certain diseases or which impair DNM1L function are located near this region or in the predicted stalk. What is the molecular mechanism by which these mutations lead to mitochondria associated diseases? Available low resolution cryo-EM structural data of DNM1L suggest an oligomerization mode that differs from that proposed for dynamin or MxA. How does DNM1L assemble into higher ordered oligomers and why should they be different from those observed for the close relative dynamin?

This work introduces the crystal structure of human dynamin 1-like protein, which is

_____

the first high resolution structure from a mitochondrial dynamin-like protein. Based on this structure, hypotheses on different aspects of DNM1L function were developed and verified by analyzing changes in protein function following mutation of selected residues. Through this approach, a function for the B insert could be proposed. Finally, by combining the low resolution cryo-EM structure with the high resolution crystal structure, a model for DNM1L oligomerization was suggested.

Taken together, the results of this work elucidate the molecular basis for oligomerization of human dynamin 1-like protein and substantially contribute to our understanding of how mitochondria are divided. Also, given the results presented here, disease-causing mutations in DNM1L can be now explained more comprehensive on a molecular level.

2. Materials and Methods

2.1. Materials

A detailed list of all materials including instruments, chemicals, enzymes, and kits can be found in the appendices A and B.

2.1.1. Chemicals

All used chemicals and consumables which are not listed in the following sections were purchased at: Roth, Jena Bioscience, Sigma-Aldrich, Life Technologies, and Merck.

2.1.2. Antibodies

Mouse monoclonal anti-DNM1L antibody	Sigma-Aldrich
Goat anti-mouse HRP-coupled secondary antibody	Jackson ImmunoResearch
Rabbit monoclonal anti-Actin antibody	Sigma-Aldrich
Goat anti-rabbit HRP-coupled secondary antibody	Jackson ImmunoResearch

2.1.3. Enzymes

DNAseI	Roche
*Dpn*I	New England Biolabs
Pfu DNA polymerase	Stratagene
*BamH*I	New England Biolabs
*EcoR*I	New England Biolabs
*Hind*III	New England Biolabs
*Xho*I	New England Biolabs
T4 DNA ligase	New England Biolabs
PreScission protease^{TM}	GE Healthcare

2.1.4. Kits

NuPAGE$^{©}$ MES SDS buffer kit	Life Technologies
NuPAGE$^{©}$ MOPS SDS buffer kit	Life Technologies
NuPAGE$^{©}$ Novex 4 - 12 % Bis-Tris	Life Technologies
Mark12^{TM} unstained ps	Life Technologies
PAGE Ruler unstained ps	Thermo Scientific
SeaBlue$^{®}$ Plus2 pre-stained ps	Life Technologies
2-Log DNA ladder	New England Biolabs
QIAprep^{TM} spin mini prep kit	Qiagen
QIAquick gel extraction kit	Qiagen
GeneAmp$^{©}$ dNTPs	Life Technologies
JBS Classics I+II suites	Jena Bioscience
JBS JSCG suite	Jena Bioscience
JBScreen Plus HTS	Jena Bioscience
MPD Suite	Qiagen
pHClear I+II suites	Qiagen
PACT suite	Qiagen
ComPAS suite	Qiagen
Classic Lite suite	Qiagen
PEGs I+II suites	Qiagen
Additive Screen^{TM}	Hampton Research
Roti$^{©}$Fect transfection kit	Roth

2.1.5. Microorganisms and cell lines

E. coli TG1	*K12, supE, hsdΔ5, thi, Δ(lac-proAB), F'[traD36, proAB^{+}, lac^{q}, lacZΔM15]* (Promega)
E. coli BL21 (DE3) Rosetta	*F^{-} ompT hsdsSB(rB^{-} mB^{-}) gal dcm (DE3) pRARE (CmR) pRARE* containing the tRNA genes *argU, argW, leX, glyT, leuW, proL, metT, thrT, tyrU* and *thrU* (Novagen)
COS-7	*CV-1* derived African green monkey kidney fibroblast-like cell line, *SV40* (lytic growth), *SV40 tsA209, T antigen* (Cell Lines Service)

2.1.6. Vectors

pSKB2LNB

modified *pET-28a* vector containing a N-terminal PreScission cleavage site (LMB)

pmeGFP-C1

mammalian expression vector containing one copy of monomeric (A206K) eGFP upstream of the protein of interest (addgene)

pDsRed2-Mito

mammalian expression vector containing the MTS from human cytC oxidase N-terminally fused to dsRed2 (Clontech)

2.1.7. cDNA clone

The cDNA for human DNM1L isoform-2 (UniProt ID: O00429-3) was derived from Source Bioscience.

2.1.8. Primers

2.1.8.1. Cloning Primers

The following primers have been used to amplify cDNA for subsequent cloning into respective vectors (Eurofins MWG).

pSKB2LNB *hs*DNM1L-i2$^{1-710}$ (*BamH*I/*EcoR*I, B491/B492)
fw. Primer   5'GGC**GGATCC**ATGGAGGCGCTAATTCCTGTC   3'
rev. Primer   5'GGC**GAATTC**<u>C</u>TATCACCAAAGATGAGTCTCCC   3'

Table 1: Overview showing primers used to amplify cDNA of human DNM1L for subsequent cloning into the respective vector. Primer-IDs are shown in parentheses. Restriction sites are in bold. Additionally introduced stop codon is underlined.

2.1.8.2. Quick change mutagenesis primers

The following primers have been used to introduce point mutations into the respective constructs or to delete the B insert (Eurofins MWG).

*hs*DNM1L-i2$^{1-710\ \Delta\text{B insert}}$ (B632/B633)
fw. Primer   5'AATGAACAATAATATAGAGGAACAGCGAGATTGTGAGGTTATTG   3'
rev. Primer   5'CCTCACAATCTCGCTGTTCCTCTATATTATTGTTCATTAGCCCAC   3'

*hs*DNM1L-i2$^{1-710\ \text{GPRP404-404AAAA (I3)}}$ (B819/B820)
fw. Primer   5'CATTAGAAATGCTACTGCTG<u>C</u>TG<u>C</u>TG<u>C</u>TGCTTTATTTGTGCCTG   3'
rev. Primer   5'CAGGCACAAATAAAG<u>C</u>AG<u>C</u>AG<u>C</u>AGCAGCAGTAGCATTTCTAATG   3'

2. Materials and Methods

---

*hs*DNM1L-i2$^{1-710\ E426A}$ (C082/C083)
fw. Primer   5 ' CAAATCAAACGTCTAGAAGCGCCCAGCCTCCGCTG   3 '
rev. Primer   5 ' CAGCGGAGGCTGGGCGCTTCTAGACGTTTGATTTG   3 '

*hs*DNM1L-i2$^{1-710\ R430D}$ (C078/C079)
fw. Primer   5 ' GAAGAGCCCAGCCTCGACTGTGTGGAACTGGTTC   3 '
rev. Primer   5 ' GAACCAGTTCCACACAGTCGAGGCTGGGCTCTTC   3 '

*hs*DNM1L-i2$^{1-710\ E490A}$ (C686/C687)
fw. Primer   5 ' CATAACTTAGTGGCAATTGCACTGGCTTATATCAACAC   3 '
rev. Primer   5 ' GTGTTGATATAAGCCAGTGCAATTGCCACTAAGTTATG   3 '

*hs*DNM1L-i2$^{1-710\ E490R}$ (C688/C689)
fw. Primer   5 ' CATAACTTAGTGGCAATTCGACTGGCTTATATCAACAC   3 '
rev. Primer   5 ' GTGTTGATATAAGCCAGTCGAATTGCCACTAAGTTATG   3 '

*hs*DNM1L-i2$^{1-710\ N635A}$ (C225/C226)
fw. Primer   5 ' CTCATTGTCAGAAAGGCTATTCAAGACAGTGTG   3 '
rev. Primer   5 ' CACACTGTCTTGAATAGCCTTTCTGACAATGAG   3 '

*hs*DNM1L-i2$^{1-710\ D638A}$ (C227/C228)
fw. Primer   5 ' CAGAAAGAATATTCAAGCCAGTGTGCCAAAGGCAG   3 '
rev. Primer   5 ' CTGCCTTTGGCACACTGGCTTGAATATTCTTTCTG   3 '

*hs*DNM1L-i2$^{1-710\ K642E}$ (C229/C230)
fw. Primer   5 ' CAAGACAGTGTGCCAGAGGCAGTAATGCATTTTTTG   3 '
rev. Primer   5 ' CAAAAAATGCATTACTGCCTCTGGCACACTGTCTTG   3 '

*hs*DNM1L-i2$^{1-710\ M482D}$ (C231/C232)
fw. Primer   5 ' CCTGTTACAAATGAAGACGTCCATAACTTAGTG   3 '
rev. Primer   5 ' CACTAAGTTATGGACGTCTTCATTTGTAACAGG   3 '

*hs*DNM1L-i2$^{1-710\ anti\ DNM1L\ siRNA\ resistance\ silent\ mutation\ cluster1}$ (C100/C101)
fw. Primer   5 ' GAAATGCTACTGGTCCTCGTCCAGCACTGTTTGTGCCTGAGGTTTCATTTG 3 '
rev.Primer   5 ' CAAATGAAACCTCAGGCACAAACAGTGCTGGACGAGGACCAGTAGCATTTC 3 '

*hs*DNM1L-i2$^{1-710\ anti\ DNM1L\ siRNA\ resistance\ silent\ mutation\ cluster\ 2}$ (C102/C103)
fw. Primer   5 ' CTGGTCCTCGTCCAGCACTGTTCGTACCGGAGGTTTCATTTGAG   3 '
rev. Primer   5 ' CTCAAATGAAACCTCCGGTACGAACAGTGCTGGACGAGGACCAG   3 '

*hs*DNM1L-i2$^{1-710\ anti\ DNM1L\ siRNA\ resistance\ silent\ mutation\ cluster\ 3}$ (C104/C105)
fw. Primer   5 ' CAGCACTGTTCGTACCGGAAGTGTCATTTGAGTTACTGG   3 '
rev. Primer   5 ' CCAGTAACTCAAATGACACTTCCGGTACGAACAGTGCTG   3 '

Table 2: Detailed overview showing primers used to introduce (silent) point mutations in DNM1L and to delete the B insert of DNM1L. Primer-IDs are shown in parentheses. Underlined nucleotides represent mutation sites. B = B insert, I3 = interface-3.

2.1.9. Media and antibiotics

Luria-Bertani (LB)

10 g/L tryptone/peptone; 10 g/L NaCl; 5 g/L yeast extract

Terrific-Broth (TB)

powder, 50 g/L + 4 mL glycerol/L

Autoinduction medium(AIM)

powder, 60 g/L + 10 mL glycerol/L

Dulbecco's modified eagle medium (DMEM)

high glucose (4.5 g/L), w/o phenol red, with L-glutamine

Ampicillin sodium salt

50 mg/mL in H_2O (1000x)

Chloramphenicol

34 mg/mL in EtOH (1000x)

Kanamycinsulfate

10 mg/mL in ddH_2O (1000x) for liquid cultures and 50 mg/mL in ddH_2O (1000x) for plates

Penicillin/Streptomycine

ready to use stock (100x) contained 10 U/ml Penicilline and 10 µg/ml Streptomycine

2.1.10. Buffers

Buffer A

50 mM HEPES/NaOH pH 7.5, 400 mM NaCl
2.5 mM 2-mercaptoethanol, 5 mM $MgCl_2$
40 mM imidazole, 0.1 mM Pefabloc protease inhibitor, 1 mM DNAseI

Buffer B

50 mM HEPES/NaOH pH 7.5, 400 mM NaCl
2.5 mM 2-mercaptoethanol, 5 mM $MgCl_2$
40 mM imidazole

Buffer C

50 mM HEPES/NaOH pH 7.5, 800 mM NaCl
2.5 mM 2-mercaptoethanol, 5 mM MgCl2
40 mM imidazole, 1 mM ATP, 10 mM KCl

Buffer D

50 mM HEPES/NaOH pH 7.5, 400 mM NaCl,
2.5 mM 2-mercaptoethanol, 5 mM $MgCl_2$,
80 mM imidazole, 0.5 % (w/v) CHAPS

Buffer E

50 mM HEPES/NaOH pH 7.5, 400 mM NaCl
2.5 mM 2-mercaptoethanol, 5 mM $MgCl_2$
300 mM imidazole

_____

Buffer F	20 mM HEPES/NaOH pH 7.5, 300 mM NaCl 2.5 mM DTT, 2.5 mM $MgCl_2$
TSS buffer	85 % (v/v) LB-medium w/o NaOH, 10 % (w/v) PEG 3350, 5 % DMSO, 50 mM $MgCl_2$, pH 6.5
Dulbecco's PBS	sterile premix, without Ca^{2+}/Mg^{2+}
10x TBE buffer stock (1L)	108 g Tris-base, 55 g boric acid 9.3 g Na_2EDTA pH 8.0
4x SDS buffer stock (10 mL)	0.2 M Tris-HCl pH 6.8, 40 % (v/v) glycerol, 0.5 M 2-mercaptoethanol, 0.3 M SDS, 1.2 mM bromphenol blue, 50 mM EDTA
HPLC buffer	100 mM potassium phosphate (pH 6.5) [K_2HPO_4 1M, 65.9 mL + KH_2PO_4 1M, 134.1 mL] 10 mM TBAB, 7.5 % (v/v) acetonitrile

2.2. Molecular biology methods

2.2.1. Polymerase chain reaction

cDNA of DNM1L as amplified with gene specific primers using *Pfu* DNA polymerase and subsequently cloned into the desired vectors using standard protocols [121].

2.2.2. DNA digestion

DNA restriction digests and digests of methylated template-DNA were conducted using enzymes from New England Biolabs according to the manufacturer's protocol.

2.2.3. Agarose gel electrophoresis

Agarose gels were prepared and ran according to standard procedures [121] using 1xTBE buffer with 0.3 µg/ml ethidium bromide.

2.2.4. DNA purification

Desired DNA bands were excised from gel and subsequently purified using the QIAquick gel extraction kit according to the manufacturer's protocol.

2.2.5. Ligation

Plasmids and DNA inserts were quantified by means of spectrometry at a wave length of 260 nm in a Nanodrop 2000 spectrophotometer (ThermoScientific). 10 ng of plasmid was ligated with six-fold molar excess of insert using DNA T4 ligase. Ligation was carried out at RT for one hour.

2.2.6. Preparation of chemically competent *E. coli*

Competent cells were prepared as described previously [122]. 1 L LB-Medium was inoculated with 10 ml pre-culture and grown at 37 °C until an OD_{600} of 0.4. Bacteria were incubated on ice for 20 min, pelleted for 5 min at 1200xg at 4 °C and re-suspended in 100 ml ice-cold sterile TSS buffer (see 2.1.10), flash frozen and stored at -80 °C.

2.2.7. Transformation of chemically competent *E. coli*

Bacteria were transformed using the heat shock method according to the standard protocol [121]. After insertion of the desired cDNA into the vector, *E. coli* TG1 was transformed with the ligation batch. Vectors were amplified isolated and sequence verified. Finally, the expression-optimized bacteria strain *E. coli* BL21 (DE3) Rosetta has been transformed with the isolated plasmids carrying the insert of interest.

2.2.8. Isolation of plasmid DNA

Plasmids were isolated using the QIAprep Spin Miniprep Kit according to the manufacture's protocol with the exception that the final elution of DNA was carried out in 50 - 75 µl ddH2O.

2.2.9. DNA sequencing

Analysis of the sequencing samples was processed by Eurofins MWG operon and by Source Bioscience.

2.2.10. Site specific mutagenesis

Site-directed mutagenesis was carried out using *Pfu* DNA polymerase according to the protocol described by Sambrook *et al*., 2001. Modifications are: 5 µl 10x *Pfu*

buffer, 5 µl dNTPs (2 mM each), 125 ng of the desired primers, 50 ng plasmid template, 2.5 U *Pfu* polymerase, ad 50 µl with dd H_2O. The batch was split in 2 x 25 µl and placed in 55 °C and 57 °C temperature vessels during primer annealing, respectively. The following thermocylce protocol was applied: 0.5 min at 95 °C, (1 min at 95 °C, 1 min at 55 °C and 57 °C, resp., desired min [500 bp/min] at 68 °C) x 18, 10 min at 72 °C. Selection of mutants was carried out after *Dpn*I digestion of target template.

2.2.11. Sequence alignments

Sequences were aligned using CLUSTAL W [123] and adjusted by hand.

2.2.12. Bacterial storage

Bacterial cultures were frozen in 30% (v/v) glycerol for long time storage at -80 °C.

2.2.13. Construct design

An overview of the constructs prepared for the present study can be found in the appendix C.

2.3. Biochemical methods

2.3.1. SDS PAGE

Separation of proteins of different molecular weight was performed according to [124] using a denaturing, discontinuous SDS-polyacrylamide gel electrophoresis (SDS-PAGE) kit at a neutral pH [125] according to the manufacture's protocol.

2.3.2. Protein over-expression test in *E. coli*

To test protein over-expression of the desired construct a selective 5 ml AIM *E. coli BL21* (DE3) *Rosetta* overnight culture carrying the respective expression plasmid was grown O/N at 37 °C. A 0.5 ml sample was taken and centrifuged for 5 min at 16,000x*g*. The pellet was resuspended in 250 µl ddH$_2$O and 20 µl thereof were mixed with 20 µl 4xSDS buffer, boiled for 10 min at 95 °C and 5 µl were loaded on a NuPAGE$^©$ Novex 4-12% Bis-Tris gel.

2.3.3. Protein solubility test

To test the solubility of a given construct, 1 L TB medium supplemented with the respective antibiotics was inoculated 1:50 with an O/N LB medium *E. coli* BL21 (DE3) Rosetta culture carrying the respective expression plasmid. Whilst shaking cells were grown to an OD_{600} of 0.4 - 0.5 at 37 °C following temperature shift to 18 °C. Protein expression was induced by addition of 40 µM IPTG and cultures were grown for another 20 h at 18 °C. Bacteria were collected by centrifugation at 4,000x*g* for 15 min at 4 °C and pellets were resuspended in 50 ml buffer A per 1 L bacteria culture pellet. The bacteria suspension was passed three times through a Fluidizer to disrupt the cells. The lysate was cleared at 35,000x*g* and 4 °C for 30 min in an Optima-L100 K ultracentrifuge using a type 35 rotor. The supernatant containing soluble cell content was filtered through a 0.2 µm filter and applied on a 1 ml HisTrap HP chromatography column equilibrated with 5 CV buffer B. The column was washed with 30 CV buffer B. Bound protein was eluted with 5 ml buffer E. Samples taken at every step of the test purification were analyzed using SDS-PAGE.

2.3.4. Large scale protein over-expression in *E. coli*

Large scale protein over-expression was accomplished using 10 L TB medium supplemented with the respective antibiotics analogous to protein solubility tests. The resuspended bacterial pellets were lysed and purified or stored at -30 °C.

2.3.5. Protein purification / AC and SEC

All chromatographic procedures were conducted at 4 °C. The filtered supernatant was applied on a chromatography column loaded with 25 ml Ni Sepharose HP beads equilibrated with 5 CV of buffer B. The column was extensively washed with buffer B until E_{280} baseline was reached. Afterwards, the column was washed with buffer 10 CV buffer C, 5 CV buffer B, 10 CV buffer D, and 5 CV buffer B to remove unspecifically bound proteins. Bound protein was eluted with buffer E and dialysed overnight at 4 °C (18 kDa cutoff) against buffer B without imidazole in the presence of PreScission protease to cleave the N-terminal His_6-tag. The protein was re-applied to a Ni-NTA column pre-equilibrated with buffer B without imidazole to which it bound under these conditions also in the absence of the His_6-tag. Subsequently, the protein was eluted with buffer B. The peak fractions were pooled and concentrated. In a final

step, DNM1L was purified by SEC on a Superdex 200 column in buffer F for crystallographic experiments or Dulbecco's PBS for biochemical experiments. Fractions containing DNM1L were pooled, concentrated and flash frozen in liquid nitrogen. All fractions collected during purification were analyzed using SDS-PAGE (see 2.3.1).

2.3.6. Protein concentration

Protein solutions were concentrated using Amicon centrifugal filter devices with a 50 kDa cutoff according to the manufacturer's protocol.

2.3.7. Determination of protein concentration

The extinction coefficient (E) of different protein constructs was determined online (http://web.expasy.org/protparam/) according to [126] and protein concentration was subsequently determined using the Nanodrop 2000 at a wavelength $\lambda = 280$ nm. The equation for the calculation of the protein concentration was derived from the Lambert-Beer law

$$A = -\log\left(\frac{I}{I_0}\right) = \varepsilon \cdot c \cdot l$$

Equation 1: The Lambert-Beer law. A = absorbance, I = intensity of light leaving the solution, I_0 = intensity of light entering the solution, ε = molar extinction coefficient, c = concentration of the solution, l = length of the light path

2.3.8. Protein storage

Pooled, concentrated SEC peak fractions were divided into appropriate aliquots, flash-frozen ($N_{2,l}$), and subsequently stored at -80 °C.

2.3.9. Western Blot

Western Blots detecting DNM1L were performed as described by Sambrook *et al.*, 2001. Actin was used as a loading control.

2.3.10. Nucleotide detection using reversed-phase HPLC

Nucleotide detection using reversed-phase HPLC was performed as described previously [127]. The principle of nucleotide separation is the interaction between the

hydrophobic static phase and the ion pairs of nucleotides and TBA in the mobile phase. Depending on the number of phosphates, a variable number of TBA-ions are bound by the nucleotide which increases the retention time on the column. The samples were diluted with buffer F to a final concentration of 50 µM (sample volume 20 µl) and applied on a HPLC system equipped with a reversed-phase ODS-2 C18 column (250 x 4 mm) equilibrated with HPLC buffer. Runs were conducted at a flow rate of 1.5 ml/min. Denatured proteins were adsorbed at a nucleosil 100 C18 pre-column. Nucleotide peaks were detected by measuring adsorption at 254 nm. The column was calibrated by standard nucleotide solutions prepared with buffer F at a nucleotide concentration of 50 µM.

2.3.11.   Isothermal titration calorimetry (ITC)

ITC experiments were carried out at 8 °C in a VP-ITC in buffer F at a protein concentration of 44 µM. Nucleotide concentration in the syringe was 1 mM. Binding isotherms were fit and equilibrium dissociation constants were calculated using the Microcal ORIGIN software. Instead of GTP, the non-hydrolyzable GTP analogue guanosine 5'-O-[gamma-thio] triphosphate (GTP-γ-S) was used.

2.3.12.   Nucleotide hydrolysis assays

GTPase activities of 10 µM of the indicated DNM1L constructs were determined at 37 °C in PBS, 2.5 mM DTT, 0.5 mM MgCl2, in the absence and presence of 0.5 mg/ml phosphatidylserine (PS) liposomes using saturating concentrations of GTP as substrate (1 mM). Reactions were initiated by the addition of GTP to the batch. At different time points, reaction aliquots were diluted 15-fold in GTPase buffer and quickly transferred to liquid nitrogen. Nucleotides in the samples were separated via a reversed-phase Hypersil ODS-2 C18 column (250 x 4 mm) using HPLC buffer. Denatured proteins were adsorbed at a C18 guard column. Nucleotides were detected by absorption at 254 nm and quantified by integration of the corresponding peaks. Rates were derived from a linear fit to the initial reaction (< 40% GTP hydrolyzed).

2.3.13. Analytical ultracentrifugation

Sedimentation velocity experiments were carried out at 35,000 rpm in an XLI analytical ultracentrifuge. 400 µl of DNM1L at a concentration of 1.8 mg/ml and reference buffer (PBS + 2.5 mM DTT) were loaded in two-channel centerpieces with an optical path length of 12 mm. Samples were measured at 10 °C in an An-50 Ti rotor at a wavelength of 280 nm with radial spacing of 0.003 cm. The program Sednterp (http://bitcwiki.sr.unh.edu/index.php/Main_Page) was used to estimate the partial specific volume ῡ from amino acid composition as well as the density ρ and viscosity η of the buffer. Data were then analyzed with the Sedfit package [128] using a continuous c(s) distribution model. Theoretical sedimentation coefficients for monomeric, dimeric and tetrameric protein species were calculated using the following equation

$$s_{20,W} = \frac{M_W \cdot (1 - \rho_{20,W} \cdot \bar{\upsilon})}{N_A \cdot \left(\frac{f}{f_0}\right) \cdot 6\pi\eta_{20,W} \cdot \sqrt[3]{\frac{3M_W\bar{\upsilon}}{\pi N_A}}}$$

Equation 2:   Calculation of the theoretical sedimentation coefficient in aqueous solution. For explanation , see text.

with $\rho_{20,w}$ and $\eta_{20,w}$ being the density and viscosity of water at 20 °C, respectively, N_A Avogadro's number and M_W and f/f_0 the protein's molecular weight and frictional ratio, respectively. Assuming frictional ratios of 1.5, 1.8 and 2.0 for monomer, dimer and tetramer, sedimentation coefficients of 4.2, 5.6 and 8.0 S were calculated for a protein with a molecular weight of 80 kDa, respectively. In the case of DNM1L, DNM1L E426A, DNM1L R430D and DNM1L E490A additional broadening of the boundary was observed in the raw data. Furthermore, for all of these four constructs, the best fit was achieved assuming frictional ratios f/f_0 < 1. This indicates fast chemical exchange reactions in the sample and was interpreted as rapid interchange between different oligomeric species.

2.3.14. Analytical gelfiltration and right angle light scattering (RALS)

A coupled RALS-refractive index detector (Malvern) was connected in line to an analytical gel filtration column Superdex 200 10/300 (flowrate 0.5 ml/min) to

determine absolute molecular masses of the applied proteins. Data were analyzed with the provided software Omnisec. Buffer F was used as running buffer. For each protein sample, 100 µl of a 4 mg/ml solution was applied.

2.3.15. Oligomerization and liposome co-sedimentation assays

For liposome co-sedimentation assays, PS liposomes were prepared in PBS as previously described (www.endocytosis.org). 0.5 mg/ml liposomes (non-filtered) were incubated at 37 °C with 0.5 mM $MgCl_2$, 2 mM GDP, and 10 µM of the indicated DNM1L construct for 10 min in 50 µl reaction volume, followed by a 200,000xg spin for 15 min at 20 °C. Supernatant and pellet fractions were analyzed on SDS gels and quantified using ImageJ [129]. For oligomerization assays, the indicated DNM1L constructs were sedimented with or without 2 mM GDP in the absence of PS liposomes. Nucleotide-free spin assays were performed without $MgCl_2$.

2.3.16. Floatation assays

PS liposomes containing 1% (w/w) 1,2-dioleoyl-sn-glycero-3-phospho-L-serine-N-(5-dimethylamino-1-naphthalenesulfonyl) (Dansyl-PS) were prepared in PBS. Liposomes at a lipid concentration of 100 µM (non-filtered) were incubated for 5 min at 37 °C with 1.25 µM DNM1L and then mixed with 75% (w/v) sucrose or Accudenz® to a final sucrose/Accudenz® concentration of 30%. The batch was then carefully overlayed stepwise with 200 µl 25% sucrose/Accudenz® and 50 µl PBS to a total volume of 500 µl. After ultracentrifugation at 200,000 x g for 1h at 4 °C or 20 °C, samples were analyzed by UV light and protein contents of equal volumes of top and bottom fractions analyzed by SDS-PAGE.

2.3.17. Electron microscopy

6 µM DNM1L or the indicated mutants were incubated with pre-warmed (37 °C) PS liposomes in PBS, in the absence or presence of 2 mM nucleotides and 0.5 mM $MgCl_2$. The volume of the reaction mix was 25 µl. After 5 minutes incubation at 37 °C, 10 µl of the reaction mix was spotted on carbon-coated copper grids, stained with 2.5 % uranyl acetate and inspected using a Zeiss EM910 electron microscope.

2.4. Crystallographic and computational methods

2.4.1. Protein crystallization

Initial crystallization trials were carried out with native DNM1L. The frozen protein solution was gently thawed on ice and diluted to 10 mg/ml using filtered buffer F in the presence or absence of 2 mM nucleotide. All crystallization trials were performed at 4 °C. Non-automated crystallization trials were carried out using the hanging drop vapour diffusion method while automated trials were done using the sitting drop vapour diffusion method. With respect to the hanging drop method 500 µl of reservoir solution containing ddH$_2$O and precipitant was temperature equilibrated and put in 24-well crystallization sealed-plates. The hanging drop consisted of 1 or 0.5 µl protein solution and 1 µl of reservoir solution. Concerning automated crystallization trials, 70 µl premixed reservoir solution was automatically put in 96 well crystallization plates. The sitting drop consisted of 300 nl protein solution and 300 nl of reservoir solution. The procedure was carried out using Hydra II fully automated 96-channel dispenser.

2.4.2. Cryo-protection of crystals

All crystal tested were treated with suitable cryo-protectants prior data collection to prevent or alleviate radiation damage to the crystals during diffraction experiments. Cryo-solutions were composed of equal volumes of protein buffer and reservoir solution from the corresponding crystallization conditions plus varying concentrations (20-30 %) of PEG200, PEG3350, MPD, or glycerol. Crystals were soaked into 6-8 µl cryo-solutions at 4 °C for at least 5 s, before being flash frozen in N$_{2,l}$. Crystals were tested at BL 14.1 at BESSY II, Berlin (see below).

2.4.3. Data collection

All data were recorded at BL14.1 at BESSY II, Berlin, using a Rayonics MX-225 CCD detector. For structure determination a native data set was collected from a single crystal using the rotation method with a φ increment of 1° at a temperature of 100 K. The wavelength of the incident X-ray beam was 0.91841 Å and the crystal to detector distance was 210.5 mm. 191 images were recorded with either 20 s exposure time. Initial indexing and determination of an optimal data collection strategy was done

using Mosflm [130]. The data set was processed and scaled using the XDS program suite [131].

2.4.4. Protein structure solution

In general, the unit cell of a crystal is generated by applying crystallographic symmetry operations such as reflections, inversions, or rotations to the asymmetric unit, which is the smallest building block of a crystal. Three-dimensional translation of the unit cell makes up the macroscopic crystal. The space group of a crystal is defined by the symmetry operations applied to the asymmetric unit and the dimensions of the unit cell. Of the 230 possible space groups, only 65 are found in protein crystals, since inversions or reflections cannot be applied to chiral molecules [132].

The electrons within a given crystal diffract an impinging X-ray beam in a process called elastic or Thomson scattering. The directions of the diffracted X-ray beam contain the information about the dimension of the unit cell and its crystallographic symmetry, whereas the intensities of the diffracted beam contain the information of the electron density contribution in the crystal. The spatial arrangement of the atoms in a crystallized molecule can be deduced with its electron density.

The sum of the scattering by all individual atoms in a given unit cell is given by its structure factor $\vec{F}(S)$,

$$\vec{F}(S) = \sum_{j=1}^{n} f_j \cdot e^{(2\pi i \vec{r_j}\vec{S})}$$

Equation 3:   Calculation of the structure factor $\vec{F}(S)$ of a given unit cell. For explanation, see text.

where j is the number of atoms in the unit cell, $\vec{r_j}$ is the position of the atom j with respect to the origin, f_j is the atomic scattering factor (available in tables), and $\vec{S} = \vec{s} - \vec{s_0}$ with $\vec{s}$ as the scattered wave factor and $\vec{s_0}$ as incident wave vector. Therefore $\vec{F}(S)$ depends on the structure of the unit cell. The total wave $\vec{K}(S)$ scattered by the summation of all unit cells in a crystal can be written as,

$$\vec{K}(S) = \vec{F}(S) \cdot \sum_{t=0}^{n_1} e^{(2\pi i t \vec{a}\vec{S})} \cdot \sum_{u=0}^{n_2} e^{(2\pi i u \vec{b}\vec{S})} \cdot \sum_{v=0}^{n_3} e^{(2\pi i v \vec{c}\vec{S})}$$

Equation 4:   Calculation of the total scattering of a wave $\vec{K}(S)$. For explanation, see text.

where n_1 are the unit cells in direction $\vec{a}$, n_2 in direction $\vec{b}$, and n_3 in direction $\vec{c}$, and the position of each unit cell are: $t \cdot \vec{a} + u \cdot \vec{b} + v \cdot \vec{c}$. $\vec{K}(S)$ almost always equals zero, unless $\vec{a} \cdot \vec{S}$, $\vec{b} \cdot \vec{S}$, and $\vec{c} \cdot \vec{S}$ are integers of h,k, and l, respectively, conditions known as Laue conditions (with *hkl* being the so-called Miller indices, describing equivalent set of planes in the reciprocal crystal lattice). The equivalent of the Laue conditions in real space is known as the Bragg's Law,

$$n\lambda = 2d\sin\theta$$

Equation 5:   The Bragg's Law describes the conditions for constructive interference for successive crystallographic planes in a crystal lattice in real space. For explanation, see text.

where λ is the wavelength of the incident X ray beam, d is the spacing between the planes in crystal lattice, and θ being the angle between the incident ray and the scattering planes. The reflections on a detector are therefore the discrete intensity maxima of diffracted X-rays. The structure factor $\vec{F}(S)$ can be also written as the integration over all electrons in the unit cell:

$$\vec{F}(S) = \int_{cell} \rho\,(\vec{r})\,e^{(2\pi i \vec{r}_j \vec{S})} dv \ ,$$

Equation 6:   Calculation of the structure factor $\vec{F}(s)$ of given unit cell as an integration over all atoms. For explanation, see text.

where $\rho(\vec{r})$ is the electron density at position $\vec{r}$. Written in fractional coordinates (x,y,z,) for the unit cell and given V as the unit cell volume one can write $dv = V \cdot dx\,dy\,dz,$ and $\vec{r} \cdot \vec{S} = (\vec{a} \cdot x + \vec{b} \cdot y + \vec{c} \cdot z) \cdot \vec{S} = hx + ky + lz.$ Now the structure factor $\vec{F}(S)$ can be written as a function of h, k, and l,

$$\vec{F}(h,k,l) = V \int_{x=0}^{1} \int_{y=0}^{1} \int_{z=0}^{1} \rho(x\,y\,z) \times e^{(-2\pi i(hx+ky+lz))} dx\,dy\,dz$$

Equation 7:   The structure factor $\vec{F}(s)$ as a function of h k l. For explanation, see text.

$\vec{F}(h,k,l)$ is the Fourier transform of $\rho(h,k,l)$ and vice versa. The Laue condition restrict scattering to occur only in discrete directions, therefore the integration can be

written as a simple summation. Substituting $\vec{F} = |F|e^{i\alpha}$ will give,

$$\rho(x\,y\,z) = \frac{1}{V}\sum_{h}\sum_{k}\sum_{l}|F(h\,k\,l)|\cdot e^{-2\pi i(hx+ky+lz)+i\alpha(h\,k\,l)}$$

Equation 8:   Electron density of a given crystal according to the Laue conditions. For explanation, see text.

As can be seen in Equation 8 one needs two terms to calculate the electron density for every position in the unit cell. $|F(h\,k\,l)|$ terms are easily experimentally accessible, since they are proportional to the measured intensities on the detector. The phase angles $(h\,k\,l)$, however, cannot be determined straightforwardly from the diffraction pattern; they are lost during the measurement. This dilemma is known as the crystallographic phase problem and there are several common ways to determine the phases during a diffraction experiment for structure determination of macromolecule under investigation [133]. One method to obtain the phases is the isomorphous replacement method (or multiple isomorphous replacement, MIR). This method implies the incorporation of heavy atoms into the protein of interest. If the crystals of the derivated protein are isomorphous to the crystals of the native protein, the heavy atom structure factor amplitudes can be approximated by considering the differences of the reflection amplitudes of both crystals. The positions (and therefore the phases, too) of the heavy atoms can then be determined using the Patterson or direct methods. The phase angles of the crystallized protein can in turn be estimated using the heavy atom phase angles.

Another method which can be applied solve the phase problem utilizes anomalous scattering (single or multiple wavelength anomalous dispersion, SAD or MAD, respectively). The so-called anomalous difference is the difference in the reflection pairs $\vec{F}(hkl)$ and $\vec{F}(-h-k-l)$ which occurs if the energy of the incident X-ray photons are close to the absorption edge of a given element. In most cases selenium is used as selenomethionine-derivated proteins can be easily produced. The anomalous differences can be used to determine the location of the anomalous scatterers in the crystal (e.g. selenium positions) and to approximate the phase angles. Nowadays, SAD and MAD and another method called molecular replacement (MR) are the most widely used approaches to solve the phase problem.

MR requires knowledge of a homologues structure which can be used to

approximate the phase angles of the crystallized protein of interest and to solve its structure. As a rule of thumb, both proteins should have > 25% sequence identity and a r.m.s.d. of < 2 Å of the C_α positions.

The structure of DNM1L was solved by molecular replacement with Phaser [134] employing the structures of the isolated nucleotide-free G domain and the stalks of human dynamin1 (pdb 3SNH) as search models [68].

2.4.5. Atomic model building and refinement

The atomic model was built and fitted into the electron density using the program COOT [135] and iteratively refined using refmac5 [136] and phenix [137], using four-fold non-crystallographic symmetry of the separated G domains, stalks and BSE. 5% of the measured X-ray intensities were set aside from the refinement for cross-validation [138].

2.4.6. Structure analysis and figure preparation

The program LigPlot+ was used for interface analysis and plotting amino acid contacts [139]. Buried surfaces areas (per molecule) were calculated using CNS [140]. Surface-accessible areas per residue were calculated using areaimol [141]. Domain superpositions were performed with lsqkab [141]. For comparisons of the four DNM1L chains, the stalks were superimposed. Conservation plot was calculated using the Consurf Server [142] and the hydrophobic surface representation was generated using VASCo [143]. Figures were prepared with PyMol [144] and Adobe Illustrator.

2.4.7. Protein structure validation and deposition

All-atom contacts and geometry of the atomic model was evaluated using the Molprobity server [145]. The validated model was deposited in the Protein Data Bank (http://www.pdb.org), with the following accession number: 4BEJ

2.4.8. Electron microscopy model fit

DNM1L tetramers were manually fit into the EM reconstruction of yeast Dnm1 [118] using the Chimera Software package [146].

2.5. Cell biological methods

2.5.1. Cell culture and transfection

COS-7 cells were routinely maintained at 37°C and 5 % CO_2 in Dulbecco's modified Eagle's medium (DMEM) with 10 % fetal bovine serum. Cells were transiently transfected with 150 pmol DNM1L-targeting siRNA duplexes using Roti-Fect according to the manufacturer's instructions. 24h post siRNA, cells were co-transfected with 300 ng pDsRed2-Mito (mito-dsRed) and 800 ng of the different DNM1L constructs using Roti-Fect.

2.5.2. Live cell microscopy

For live cell microscopy, cells were cultured on 35 mm glass bottom dishes and transferred to low bicarbonate DMEM without phenol red supplemented with 25 mM HEPES pH 7.4. Live cell microscopy was performed 48 h post siRNA (24h post DNA) on a Olympus FluoView FV1000 confocal microscope equipped with a 60 x NA:1.30 silicone UPlanSApo objective. dsRed and meGFP were imaged using 559 nm and 488 nm laser lines, respectively.

2.5.3. Mitochondrial connectivity FRAP assay

For FRAP experiments, 48 h post siRNA transfection (24 h post DNA transfection) dsRed images (51 x 51 μm) were acquired and a circular ROI (d = 6.21 μm) approximately 10 μm distant from the nucleus was defined. The ROI was bleached for 1 s with 100 % laser power (559 nm) and dsRed fluorescence recovery was monitored for 90 s (1 frame/second). Mean fluorescence intensities within the ROI were calculated over time, initial values from pre-bleach images were normalized to one (n = 18 - 22 for each construct). Experiments were performed at room temperature.

3.   Results

3.1.   Protein production and biochemistry

3.1.1.   Protein over-expression

To obtain sufficient amounts of human DNM1L for crystallization trials and biochemical studies, the corresponding human cDNA encoding isoform 2 of DNM1L was PCR-amplified and cloned via standard restriction enzyme cloning methods in the bacterial expression vector pSKB2LNB and pmeGFP-C1 (see 2.2). The bacterial strain *E. coli* BL21 (DE3) Rosetta (see 2.1.5) optimized for eukaryotic protein expression was subsequently transformed with sequence-verified clones, allowing for IPTG-inducible expression. All constructs were expressed as N-terminally hexahistidine-tagged proteins with a PreScission protease cleavage site in the linker region between the His_6-tag and the protein under investigation. Protein over-expression and solubility was checked as described in 2.3.2 and 2.3.3. As can be seen in Figure 22, expression of the desired construct resulted in an additional band of approximately 80 kDa, compared to the non-induced samples. This indicated that the tested constructs were clearly over-expressed in *E. coli.* This was true for all DNM1L constructs investigated in the present study (see appendix C).
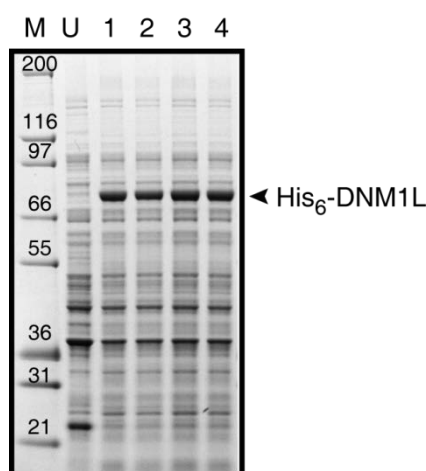
Figure 22:   Expression test. SDS-PAGE of a protein over-expression experiment. M - protein marker with molecular weight in kDa, U - non induced *E. coli* culture, 1-4 - four different DNM1L clones tested all of which clearly show an overexpression of the protein under investigation.

3.1.2.   Protein solubility and purification

Solubility of protein constructs is a prerequisite for their large scale purification. To check solubility of the various DNM1L constructs, cleared cell lysates were prepared after O/N bacteria-expression at 18 °C (see 2.3.3). After cells were broken, soluble material was separated from non-soluble cell content by ultracentrifugation. Supernatant fractions containing soluble proteins were analyzed by SDS-PAGE. As can be seen in Figure 23A, the tested construct was soluble. All constructs investigated in the present study were highly soluble, except construct
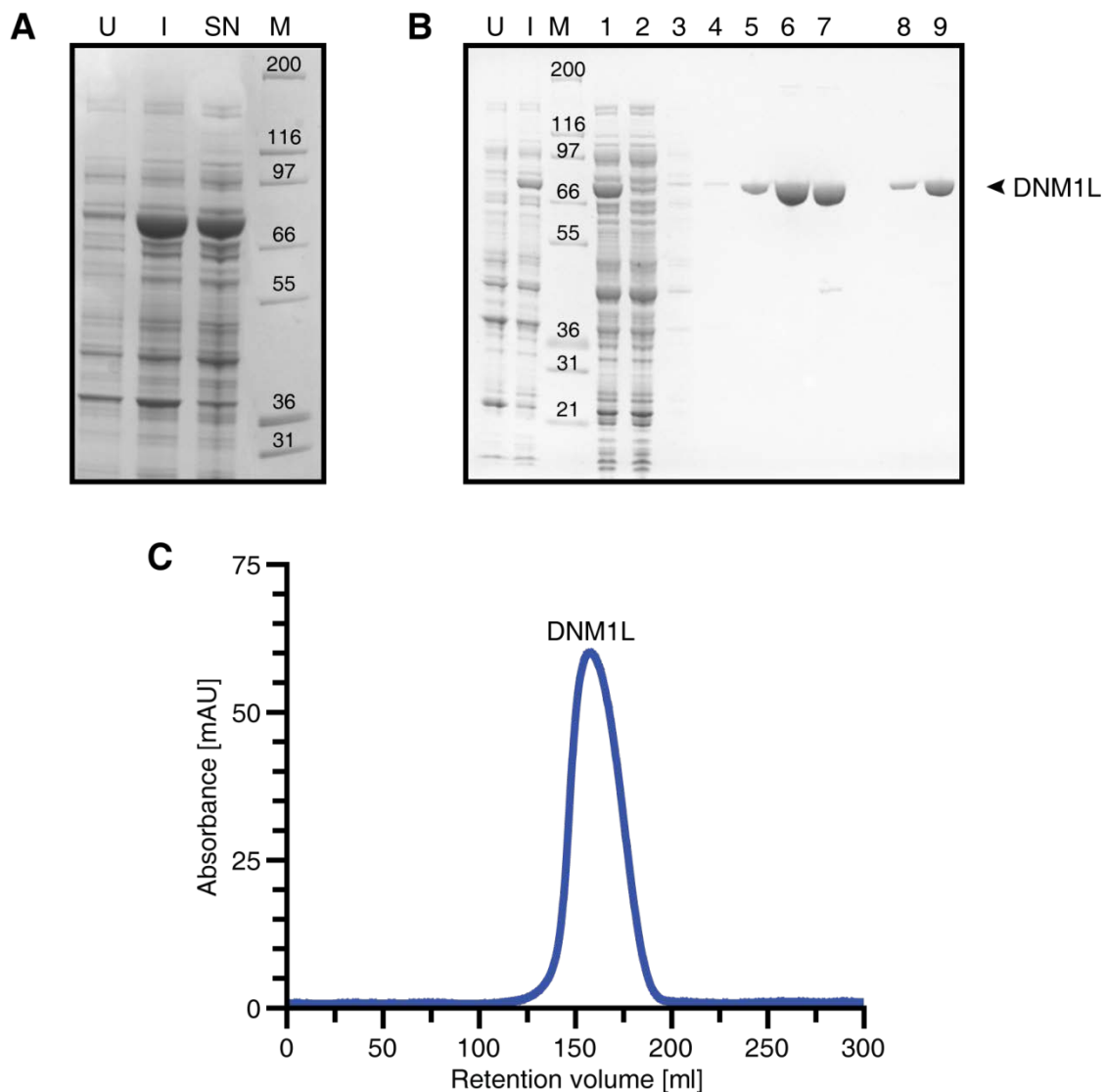
Figure 23:   DNM1L purification. **A:** SDS-PAGE showing solubility test of DNM1L. **B:** SDS-PAGE showing expression and purification of DNM1L. U- non-induced, I - induced *E.coli* culture, SN - supernatant, M - marker proteins with molecular weight in kDa, 1-5 - Ni-NTA column wash fractions, 6 - elution peak fraction of the Ni-NTA column, 7 - after cleavage of the His$_6$-tag, 8-9 - peak fractions from gelfiltration (Superdex 200). For explanation see text. **C:** SEC elution profile of full length DNM1L which eluted in a discrete peak (Superdex 200 26/60).

DNM1LΔ514-613 which exhibited a significantly reduced solubility (see 3.3.2).

Having tested reliable protein overexpression and protein solubility in small-scale, constructs were expressed in large-scale using 10 L *E.coli* cultures. After O/N expression at 18 °C, soluble cell content containing His_6-DNM1L was purified via AC (see 2.3.5). Bound DNM1L was eluted and dialysed overnight at 4 °C in the presence of PreScission protease to cleave the N-terminal His_6-tag. Protein was further purified via a second AC step as it bound to the beads even without His_6-tag in the absence of imidazole. Cleaved and polished protein was subsequently purified via SEC in a last step. During purification, fractions were collected and analyzed using SDS-PAGE. Gel filtration peak fractions containing the desired protein were pooled and further concentrated via ultrafiltration (see 2.3.6). Finally, protein concentrations were determined photometrically at λ = 280 nm (see 2.3.7) and appropriate protein aliquots snap-frozen for long term storage (see 2.3.8).

As can be seen in Figure 23B, the fractions not binding to NiNTA beads (lane 2) contained most of the soluble cell content but not His_6-DNM1L. Wash fractions (lane 3-5) contained mostly unspecific bound material and traces of His_6-DNM1L. Elution fractions and fractions taken after tag-removal and the second AC step contained almost pure protein (lanes 6 and 7, respectively). Pooled and concentrated gel filtration peak fractions (Figure 23C) showed no apparent protein contamination, as can be seen in lanes 8 and 9.

All DNM1L constructs investigated in the present study have been purified using the same protocol leading to protein yields between 15 - 120 mg/10L bacteria culture, sufficient for high throughput crystallization trials and biochemical characterization.

3.1.3.   Nucleotide binding and affinity

Homogenous nucleotide-loading is a prerequisite for all subsequent biochemical and structural experiments. Therefore, the nucleotide-loading state of purified constructs was determined by HPLC measurements (see 2.3.10). Purified DNM1L was nucleotide-free, as can be seen in Figure 24. This was true for all constructs purified in this work.

In order to quantify the affinity of purified DNM1L towards GTP and GDP, ITC experiments were carried out (see 2.3.11). Full length DNM1L has weak affinities for nucleotides in the micromolar range, with preferential binding of GTP over GDP. The protein bound to GTP-γ-S with a dissociation constant (K_d) of 10 μm and GDP with a
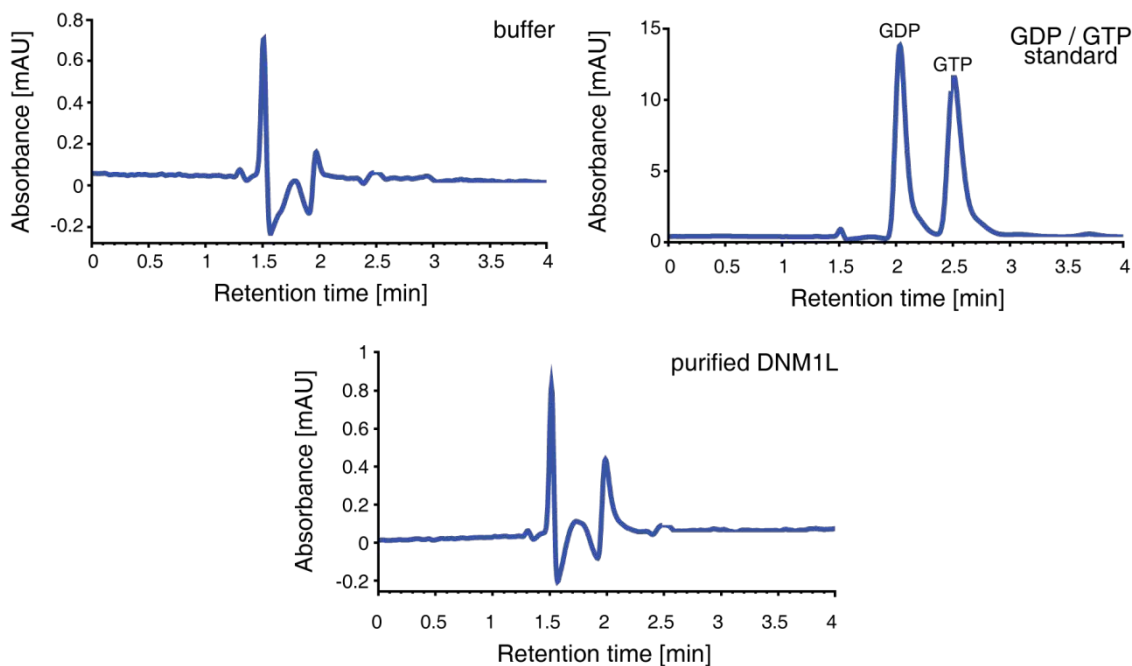
Figure 24:   Nucleotide-detection in DNM1L. DNM1L is nucleotide-free after purification as analyzed with reversed-phase HPLC. No GDP or GTP peaks were detected in a sample containing 50µM DNM1L. Standard solution contained 50 µM GDP and GTP, respectively. Note the different scales in each chromatogram.

K_d of 23 nm (Figure 25). The low affinity towards nucleotides is in agreement with data from other members of the dynamin superfamily [31, 91, 147].
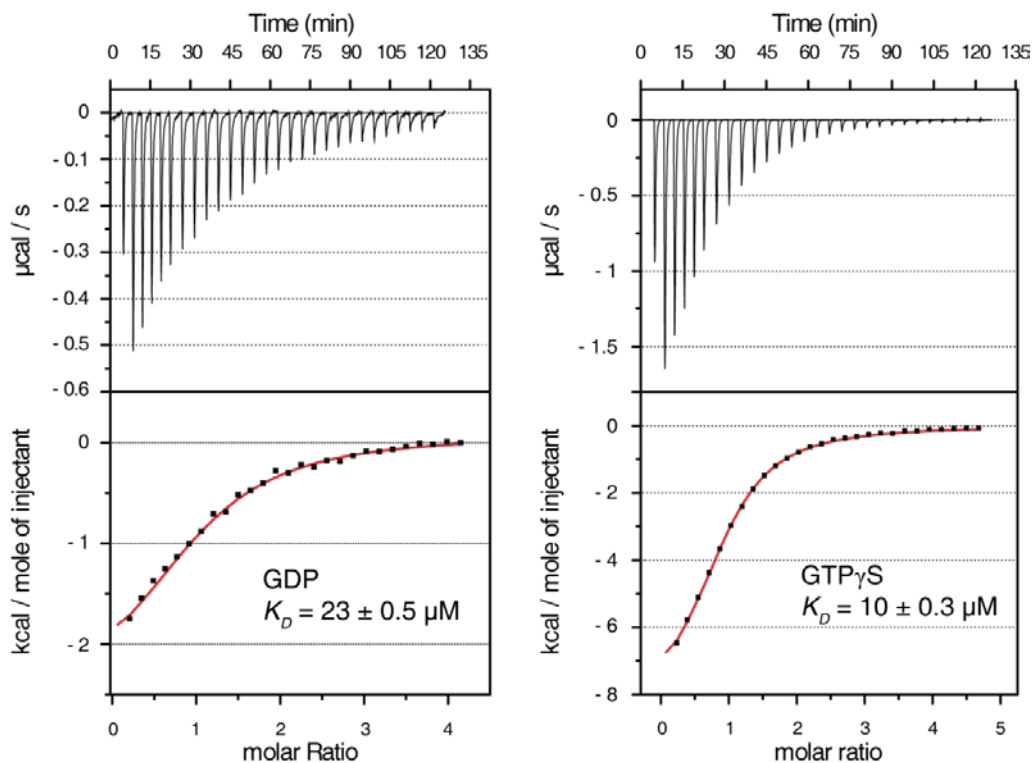
Figure 25:   ITC experiments. Nucleotide-binding affinities of DNM1L for GTP-γ-S and GDP were determined by isothermal titration calorimetry. The following values were obtained from the fits: GTP-γ-S: K_d = 23 ± 0.5 µM, n= 0.90± 0.01; GDP: K_d = 10 ± 0.3 µM, n= 1.05± 0.05.

3.2.   Structural analysis of DNM1L

3.2.1.   Crystallization and structure determination

To obtain insights into atomic structure of DNM1L, purified full length DNM1L was subjected to crystallization trials (see 2.4.1). Despite extensive screening efforts in the absence and presence of various nucleotides no crystals were obtained for this construct.

Crystallization of other dynamin superfamily members dynamin [68, 69] and MxA [50] was successful by introducing a mutation in a highly conserved amino acid stretch in the predicted interface 3 (GPRP401-404AAAA, from here on to referred to as 4A mutation). Also in yeast Dnm1, a mutation in the first glycine residue in this motif prevents mitochondrial targeting [69]. However, DNM1L 4A never crystallized in any condition tested. Additionally, an insertion of 100 amino acids residues at the tip of the stalk, the B insert, was deleted (aa 514 - 613), since it was predicted to be unstructured and might thus interfere with crystallization (as predicted with Jpred3, [148]).

Using the sitting drop method, platelet-shaped crystals of this construct (DNM1L 4A ΔB) were grown in the absence of nucleotide using 20-25 % (w/v) PEG3350, PEG1500, PEG3000, PEG3350, PEG4000, PEG8000, or PEG10000 as precipitant. Crystals appeared after 1-4 days at 4 °C and were surrounded by precipitate and phase separation. A PEG versus pH fine screen using increasing PEG concentrations and different molecular weight PEGs (PEG100 - PEG20000) against a wide variety of different buffer substances (linear pH range between 4 and 9) was conducted to improve crystal quality. The platelets could be optimized in size and robustness using the following condition: 10 % (w/v) PEG3350 and 100mM HEPES pH 7.5. However, the obtained platelets were still partially stacked and surrounded by precipitate and/or phase separation. After testing 48 different ions (from a self-made ion screen) and 96 commercially available reagents as additives (from the JBScreen Plus HTS kit) at final concentrations of 50mM - 200mM, dragonfly wing-shaped platelet clusters could be grown in 12 % PEG3350 and 50 mM K(HCOO) (Figure 26, left). A single plate (150 μm x 80 μm x 10 μm) could be broken off and, to reduce radiation damage during X-ray exposure, was transferred into a cryo-solution containing mother liquor and additionally 27 % PEG3350 (see 2.4.2, Figure 26 right).
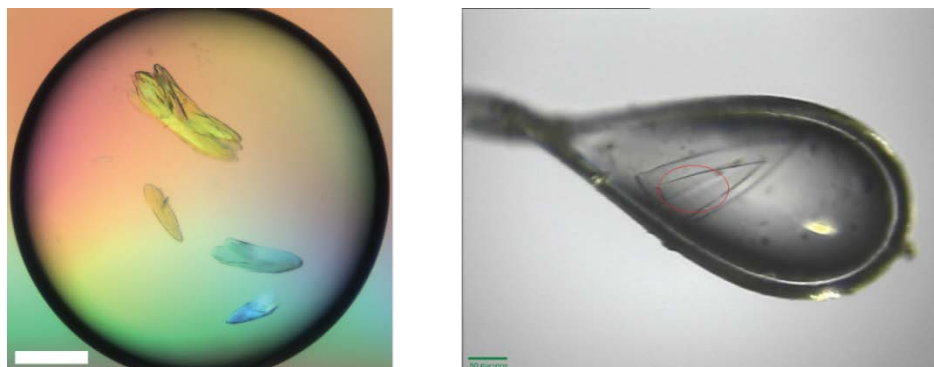
Figure 26: DNM1L crystals. Left panel: Crystals of nucleotide-free DNM1LΔ514-613 4A in the presence of PEG3350. Right panel: Cryo loop mounted at BESSY Beamline 14.1 containing one crystal of DNM1L. The red oval indicates the direction of the X-ray beam. Scale bars = 50 µm.

Immediately after the transfer into the cryo-protectant, the crystals were flash-cooled using $N_{2,l}$ according to [149]. Using the same construct and more than 4000 different crystallization conditions, however, no crystals could be obtained in the presence of any nucleotide.

X-ray data were collected as described (see 2.4.3). The crystals diffracted X-rays to a maximum resolution of 3.5 Å and belong to the monoclinic space group P2 with cell dimensions a = 101.47 Å, b = 80.77 Å, c = 208.27 Å, α = 90°, β = 93.45°, γ = 90° (Table 3). The structure was solved by molecular replacement (see 2.4.4) und subsequently refined in order to obtain a molecular model suitable for structural analysis (see 2.4.5).

Data collection	DNM1L native
Beamline	BESSY 14.1
Wavelength [Å]	0.91841
Space group	P2
Cell dimensions	
a, b, c [Å]	101.47, 80.77, 208.27
α, β, γ [°]	90.00, 93.45, 90.00
Resolution [Å] †	50.00 (3.69) - 3.48
R_{sym} (%)	13.6 (56.6)
I / σ	10.2 (2.4)
Completeness (%)	97.3 (84.3)
Redundancy	3.9 (3.7)

Table 3: Data collection statistics of native DNM1LΔ514-613 4A. † Numbers in parentheses apply for the highest resolution shell.

Refinement	DNM1L native
Resolution [Å]	50.00 - 3.46
No. reflections	42,384
R_{work}[†] / R_{free}[‡] [%]	25.1 / 27.6
Protein molecules / asymmetric unit	4
No. protein atoms	17,076
B-factor protein [Å^2]	56.4
R.m.s. deviations	
Bond lengths [Å]	0.007
Angles [°]	1.618

Table 4: Refinement statistics of native DNM1LΔ514-613 4A. [†] $Rwork = \frac{\sum_{h,k,l}||F_{obs}(h,k,l)|-|F_{calc}(h,k,l)||}{\sum_{h,k,l}|F_{obs}(h,k,l)|}$. [‡] $Rfree$ was calculated with 5 % of reflections excluded from the refinement.

In the final model, chain A consists of residues 1-54, 58-71, 85-118, 125-152, 161-231, 234-251, 256-350, 360-401, 408-449, 454-507, 616-703, chain B of residues 1-73, 84-119, 124-152, 160-350, 361-401, 408-449, 455-504, 616-675, 679-701, chain C of residues 1-55, 58-71, 88-118, 124-249, 255-326, 329-350, 360-399, 408-450, 455-503, 617-676, 683-704, chain D of residues 1-52, 58-71, 88-117, 125-153, 159-323, 329-350, 358-401, 406-449, 454-502, 615-705. 94.3% of all residues are in the favored regions of the Ramachandran plot and there are nine out-

In preferred regions: 1960 (94.3 %)
In allowed region: 110 (5.27 %)
Outliers: 9 (0.43 %)
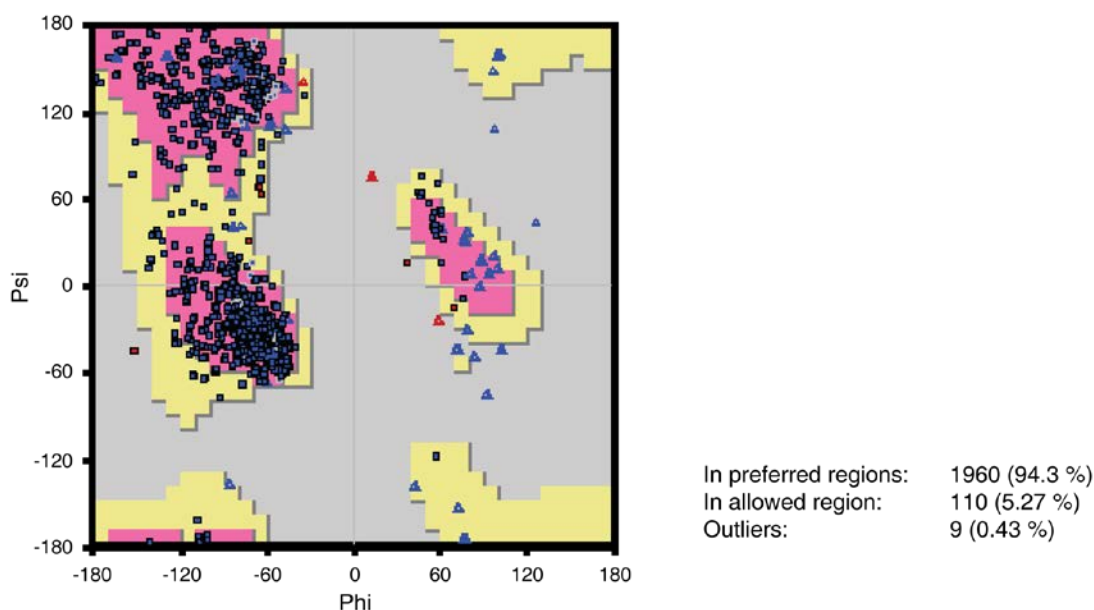
Figure 27: Ramachandran plot of the DNM1L 4A ΔB structure. Of all residues 94.3 % exhibit preferred and 5.27 % exhibit allowed Psi- and Phi-angle values (blue Δ/□). There are nine outliers in the structure (red Δ/□).

liers, as analyzed by MolProbity [150] (Figure 27). The structure was refined to an R_{work} / R_{free} of 25.1 % / 27.6 % (Table 4) (see 2.4.5). Data collection and refinement statistics are given in Table 3 and Table 4, respectively.

3.2.2. Structure of DNM1L
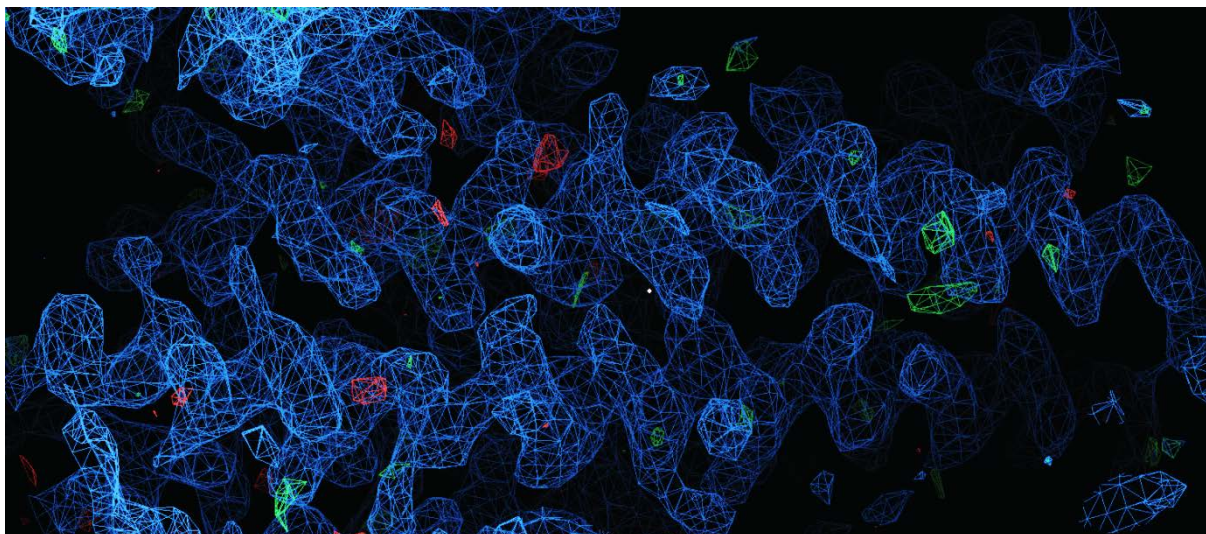
Figure 28: Electron density of the DNM1L stalk. Final $2F_0 - F_c$ and $F_0 - F_c$ maps from the DNM1L 4A ΔB crystal showing stalk helices. The $2F_0 - F_c$ map is shown in blue mesh at contour level of 1.2σ, the $F_0 - F_c$ map is shown in green (positive) and red (negative) mesh at 3σ.

The asymmetric unit of the crystal contained four DNM1L molecules (chain A-D), and the use of non-crystallographic symmetry during refinement resulted in improved electron density maps (Figure 28). Accordingly, the BSE and several loop regions not present in the initial search model could be built in the electron density (Figure 29). If not otherwise mentioned, the best defined monomer in the asymmetric unit (chain A of the tetramer) is described in the following.
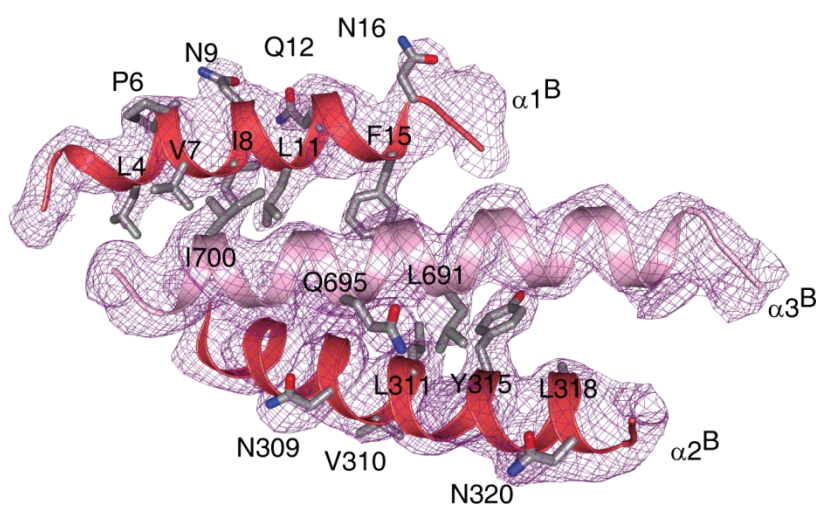
Figure 29: Electron density of the DNM1L BSE. Refined $2F_0-F_c$ electron density of the BSE at a contour level of 1.2 σ. Well-defined residues are shown in stick representation.
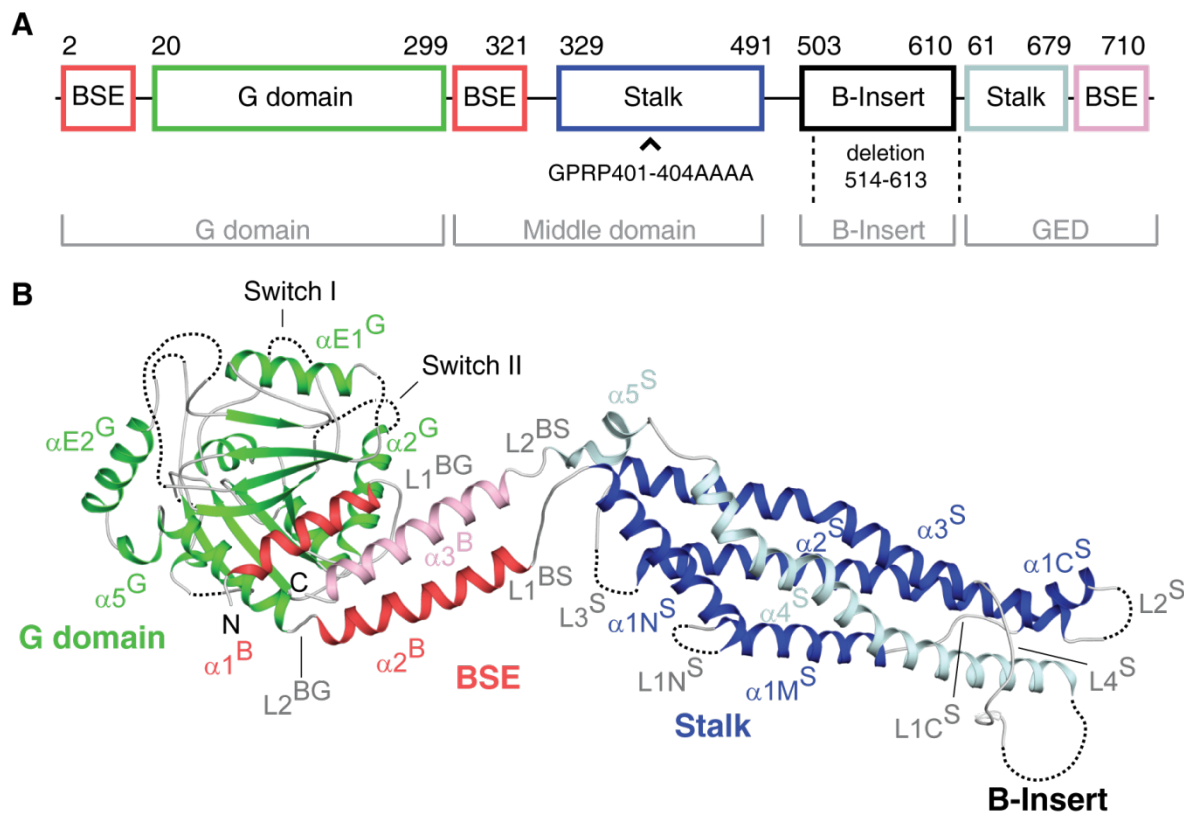
Figure 30: The structure of DNM1L. **A:** Structure based domain architecture of DNM1L. The first and the last residue of each domain are labeled. The classic domain assignment is shown below. **B:** Ribbon-type representation of DNM1L. Regions not resolved in the crystal structure, such as the B insert, are indicated by dotted lines. N- and C-termini are labeled.

DNM1L has a typical dynamin superfamily architecture composed of a G domain, a BSE and a stalk (annotated as superscript G, B, S). These domain boundaries deviate from the sequence-derived domain boundaries (Figure 30A). The amino terminal G domain of DNM1L is composed of a central β-sheet of eight β-strands surrounded by 8 α-helices. Structural elements of the G interface mediating GTP-dependent dimerization in dynamin, including switch I and II and the trans stabilizing loop, are only weakly defined in the electron density. The G domains in the crystals do not interact with each other via this G interface, as expected for the nucleotide-free state of a dynamin superfamily member. Adjacent to the G domain, the BSE is composed of a three helix bundle (Figure 30B) [62]. $\alpha 1^B$ at the N-terminus, $\alpha 2^B$ at the C-terminal of the G domain and $\alpha 3^B$ at the C-terminus of the same DNM1L molecule assemble via hydrophobic contacts. Additionally, $\alpha 1$ and $\alpha 3$ interact via hydrophilic and hydrophobic contacts with the G domain (Figure 31). The central localization in the DNM1L molecule and the architecture involving elements from widely dispersed regions in the DNM1L sequence suggest a function of the BSE as transmitter of conformational changes between the G domain and stalk. The stalk is composed of
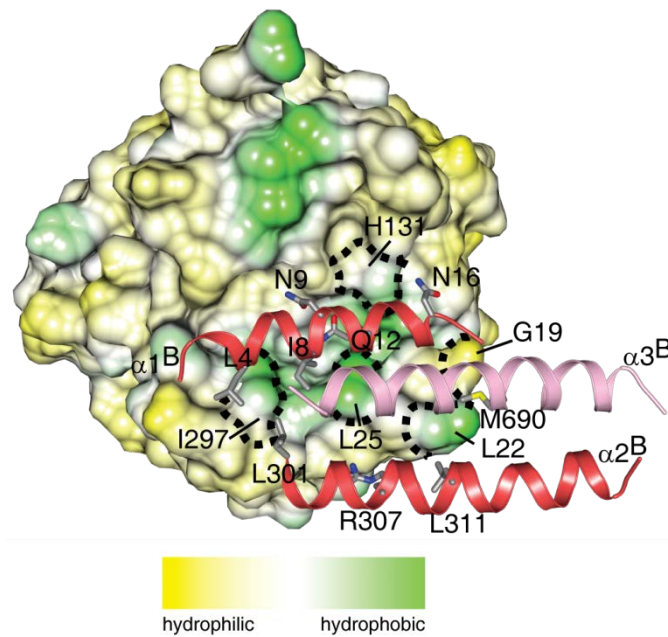
Figure 31: The G domain-BSE interface of DNM1L. Surface hydrophobicity plot of the DNM1L G domain showing the interaction with the BSE (in cartoon representation). Selected residues of the G domain and BSE are indicated.

of an elongated four helix bundle (Figure 30B). $\alpha1^S$ is subdivided into $\alpha1N^S$, $\alpha1M^S$ and $\alpha1C^S$ by the two disordered loops $L1N^S$ and $L1C^S$. Interestingly, mutations in and around $L1N^S$ in Dnm1 [117, 151], dynamin [152], and MxA [50] prevent oligomerization and lead to the formation of stable dimers suggesting that this loop is involved in oligomerization (see [68] for a model in dynamin). $\alpha3^S$ is extended by the conserved loop $L4^S$ which passes over into the B insert.

The B insert is interspersed between $L4^S$ and $\alpha4$ at the equivalent sequence position as the PH domain of dynamin [68] and the membrane binding loop L4 of MxA [80]. It is predicted to be unstructured and was proposed as putative membrane interaction site [118] although it was reported not to be essential for mitochondrial targeting and membrane binding [153, 154].

The DNM1L monomer in the asymmetric unit showed two different orientations of the G domain and BSE relative to each other. Upon comparison of chains A/B with chains C/D, the G domain - BSE unit was 17.5° rotated with respect to the stalk, around the two loops $L1^{BS}$ and $L2^{BS}$ connecting BSE and stalk (Figure 32). It was previously suggested that these loops constitute a hinge in dynamin and MxA (hinge 1), which allows for flexible domain interplay during mechano-chemical
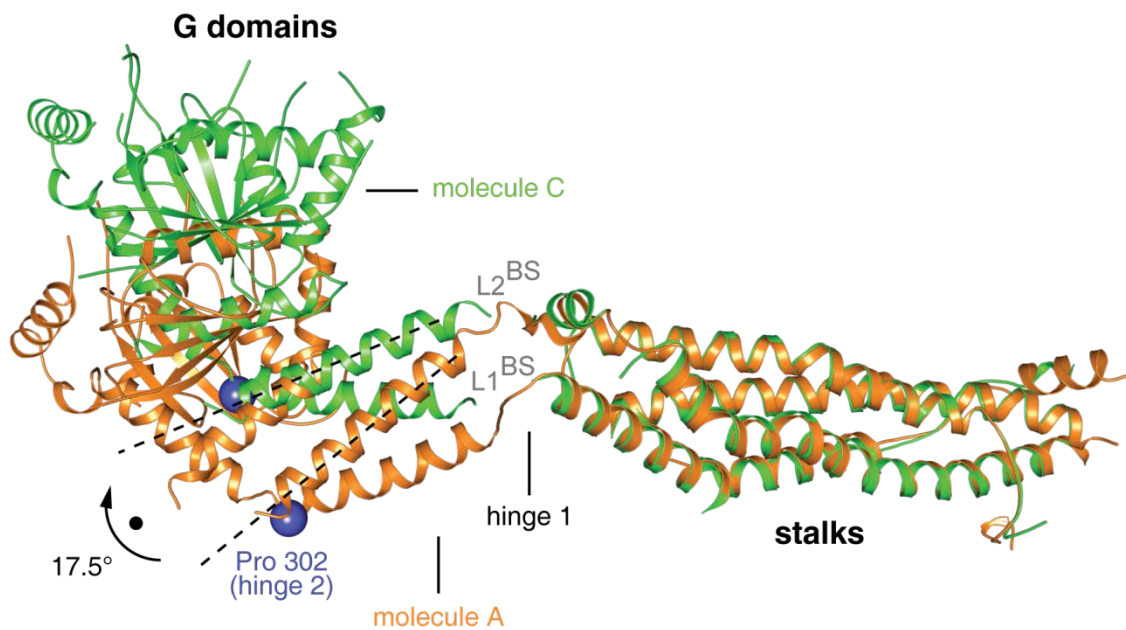
Figure 32: The DNM1L hinge regions. Superposition of molecules A and C of the DNM1L tetramer. A 17.5° rotation of the G domains around hinge 1 is evident. The conserved proline residues constituting the predicted hinge 2 are indicated as blue spheres.

coupling [68, 79] (see 1.3.1.2 and 1.3.2.2) The two conformations seen here indicate that such large scale conformational movements around hinge 1 are indeed possible. Taken together, the overall structure of DNM1L is similar to the full length structures of dynamin (Figure 10A) and MxA (Figure 13). The main differences originate from different conformations in hinge 1.

3.2.3. The stalk interfaces

The four DNM1L molecules in the asymmetric unit assembled into two dimers via a symmetric interface of 1000 Å^2 in the center of the stalks (Figure 33 left, Figure 34A, C). This dimerization interface included both hydrophobic contacts and salt bridges resulting in an X-shaped stalk dimer involving $\alpha 3^S$ and $\alpha 4^S$. Residues in this interface are highly conserved in dynamin and partly conserved in MxA (Figure 35). Accordingly, a similar X-shaped stalk dimer was found in dynamin and MxA [50, 68, 69]. With respect to the dynamin-nomenclature, this interface was termed interface 2 (Figure 34C).

The DNM1L dimers in the crystals were stacked on each other via an additional heretofore not described interface in the stalk (termed interface 4) which was located at the opposite side of interface 2 (Figure 33 right, Figure 34B, D). This interaction

_____

was mediated by non-crystallographic symmetry and was present twice in the asymmetric unit. Interface 4 had a size of 430 $Å^2$, was dominated by ionic interactions and showed only limited sequence similarity to dynamin and MxA (Figure 35). The alternating assembly of DNM1L via interfaces 2 and 4 led to the formation of linear stacked DNM1L filaments in the crystals. In this oligomer, all G domains were located on one side of the filament whereas all B-inserts pointed to the opposing side. The organization of this filament is different from that of dynamin1 and MxA.
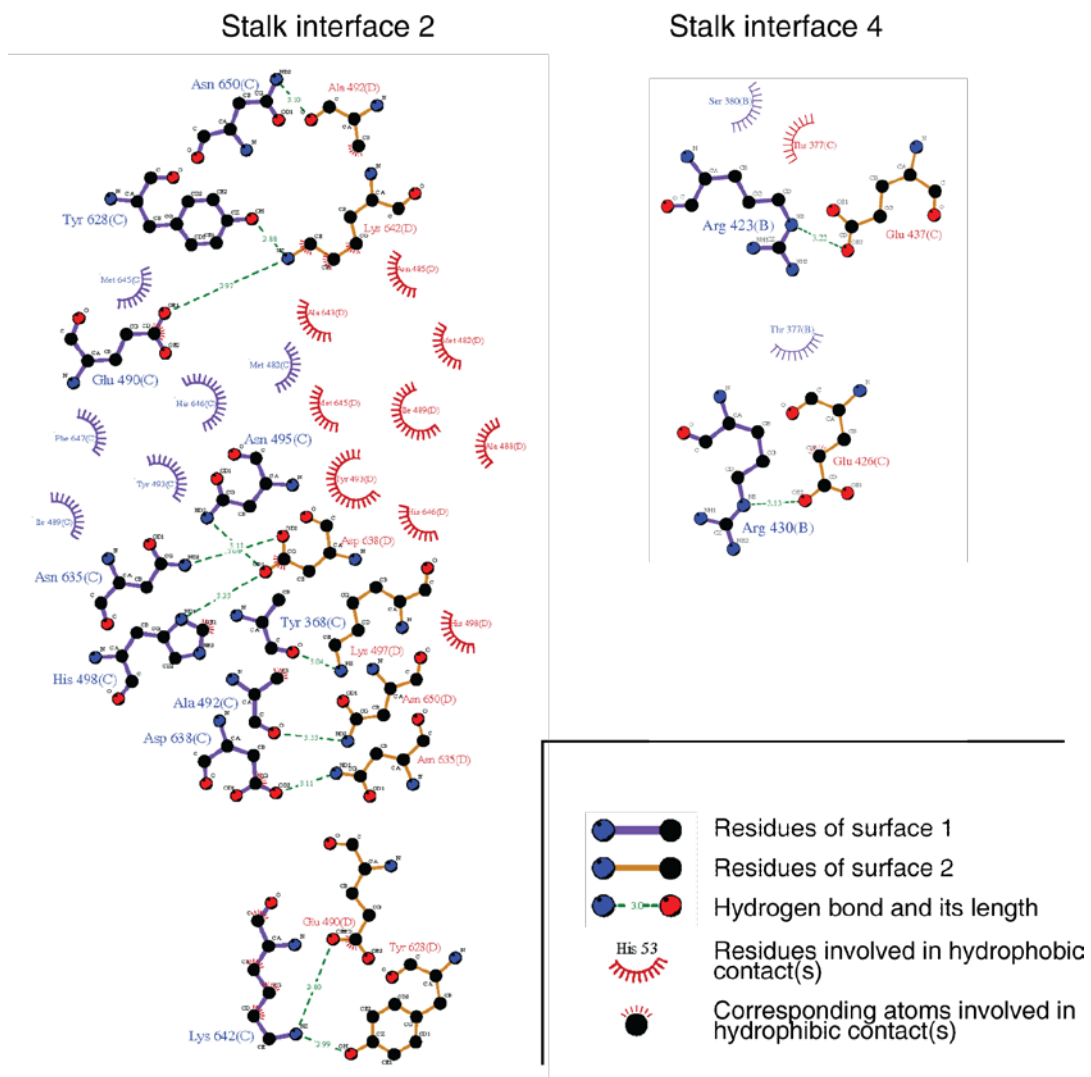
Figure 33: Schematic representation of the DNM1L stalk interfaces. Interface plots showing interacting residues of molecules C and D constituting stalk interface 2 and of molecules B and C constituting stalk interface 4.
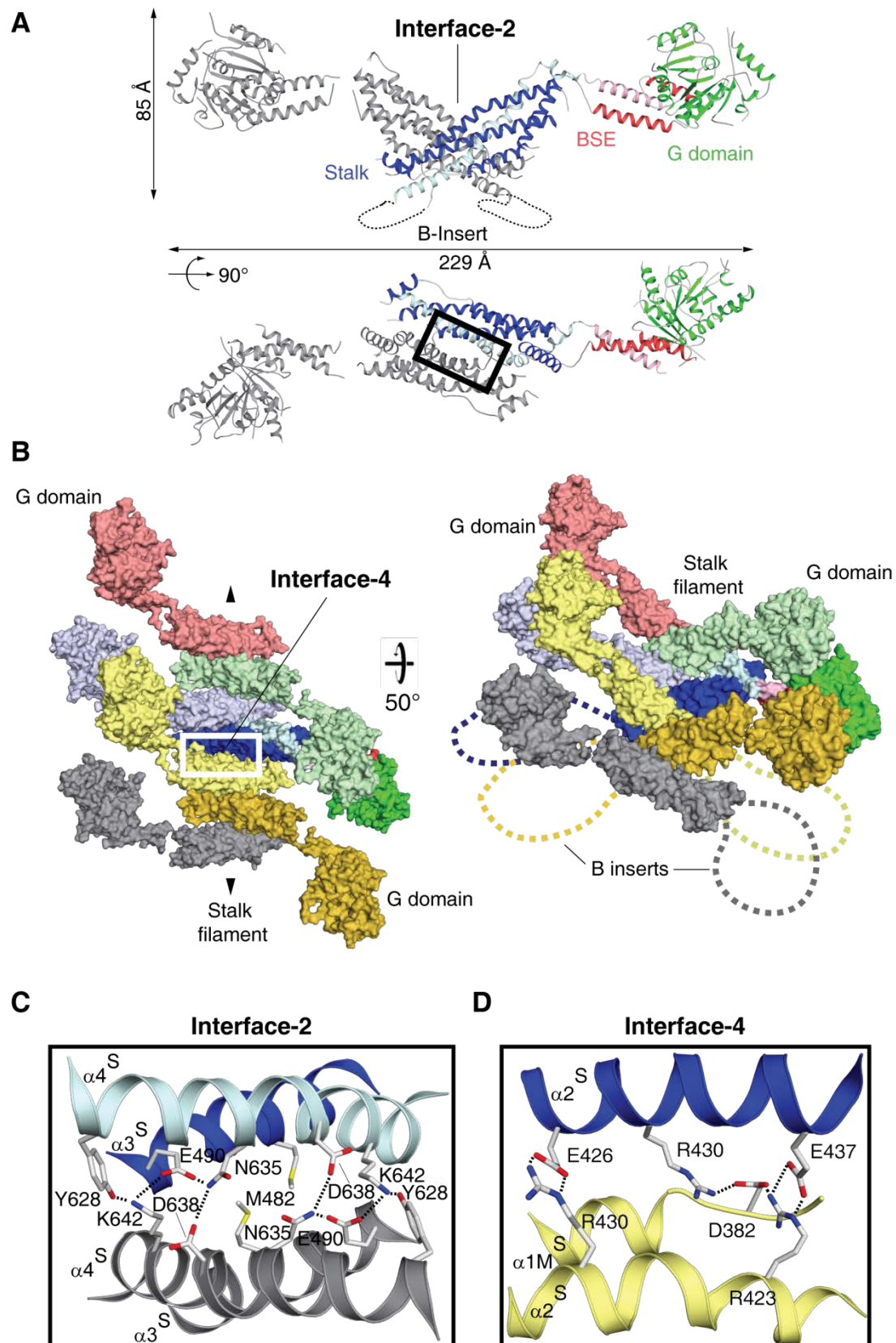
Figure 34: Structural representations of the DNM1L stalk interfaces. **A**: Two views on the DNM1L dimer which assembles via the central stalk interface 2 (black box). **B**: Two views on a surface representation of the DNM1L oligomer in the crystal. Interface 4 is indicated (white box). The direction of the oligomer is indicated by arrows. **C**: Close-up views into interface 2 **D**: Close-up view into interface 4. Hydrogen bonds are indicated as dotted lines.

_____
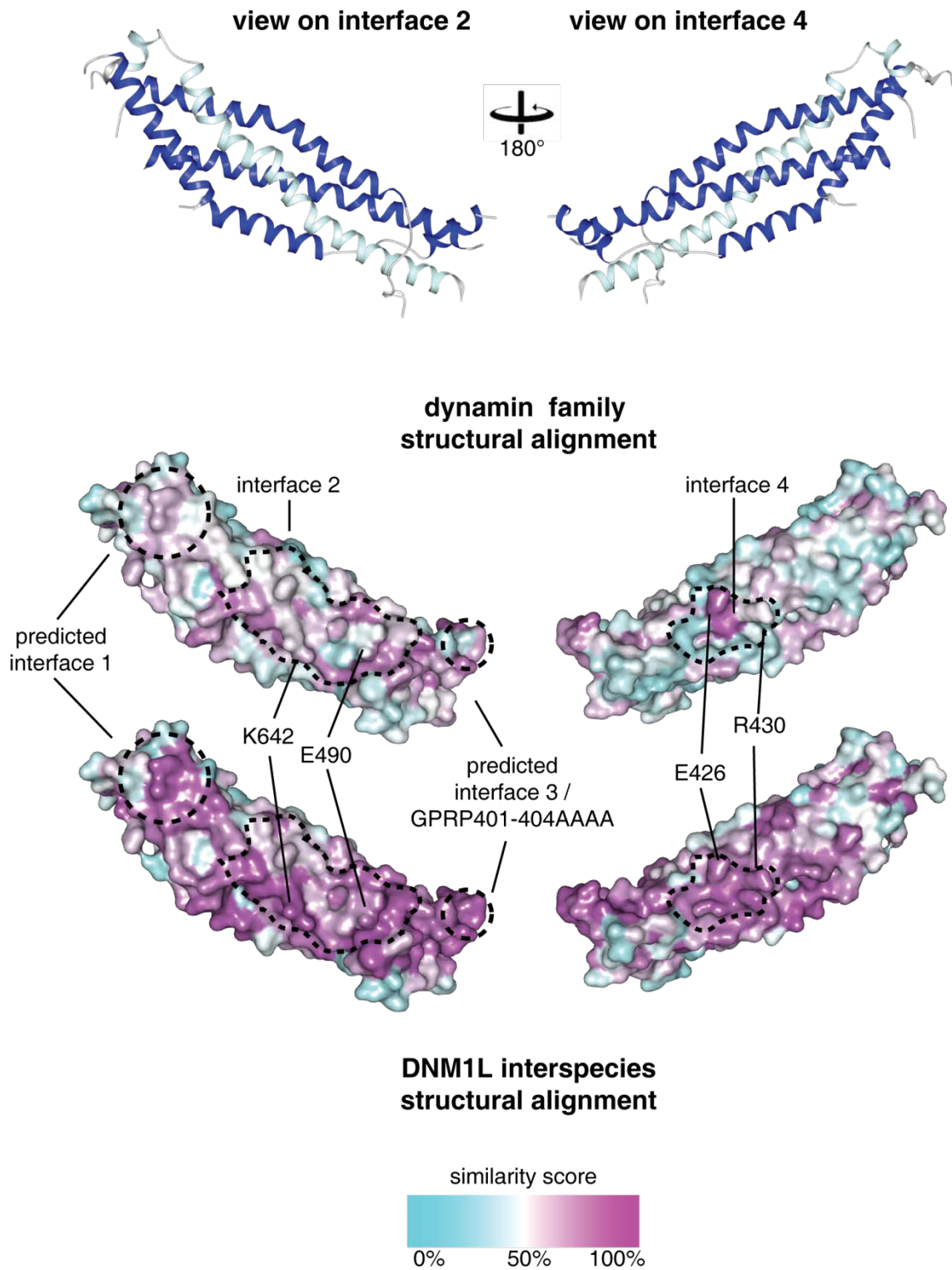
Figure 35: Surface conservation plot of the DNM1L stalk. Upper panel: Ribbon-type representation of the DNM1L stalk. Middle panel: Surface conservation plot of the DNM1L stalk in the same orientation as in the upper panel, based on the alignment of 4 dynamin superfamily members, as shown in appendix D. The determined and predicted oligomerization interfaces are indicated. Lower panel: Surface conservation plot of the DNM1L stalk, based on a sequence alignment of seven DNM1L sequences (*H. sapiens, M. musculus, D. rerio, A. thaliana, D. melanogaster, C. elegans, S. cerevisiae*).

3.2.4. Localization of the B insert and the GPRP motif

It was previously suggested that the B insert allosterically modulates DNM1L assembly [153, 154]. However, structural data of the present study also point to a function of the B insert in targeting DNM1L to the mom. The deduced position of the B insert is in direct vicinity of the highly conserved GPRP motif in loop L2^S (residues 400 - 408) at the tip of the stalk containing the 4A mutation in the crystallized construct (Figure 36). The B insert is not resolved in the present structure as it is predicted to be unstructured [148], hence potentially inhibiting crystallization. Therefore it was deleted from the sequence to get diffraction-quality crystals. As can be seen in Figure 36 the B insert contains most of the reported post-translational modifications sites involving SUMOylation, phosphorylation, and S-nitrosylation. SUMOylation occurs at two lysine clusters within the B insert [155]. There are eight
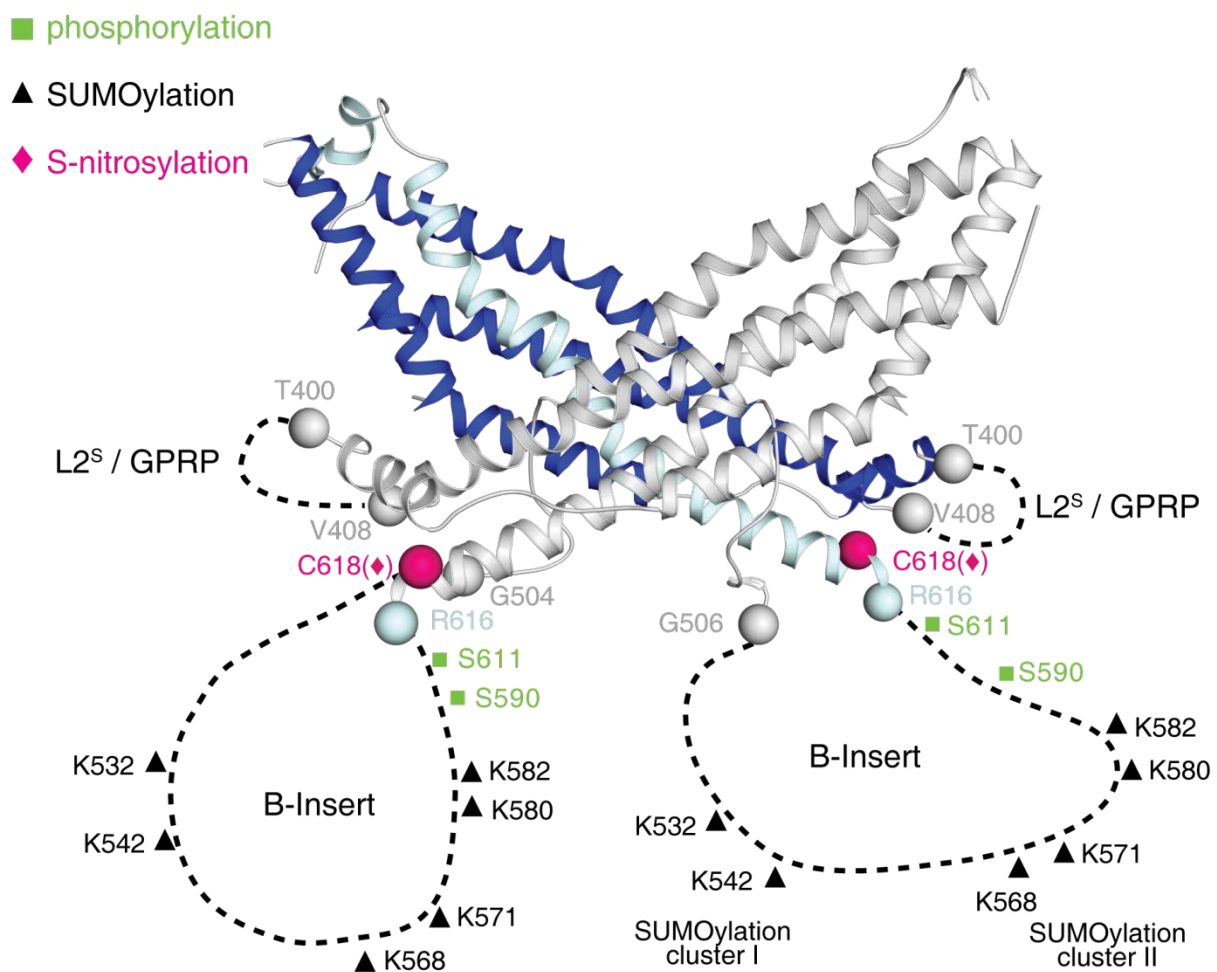
Figure 36:   The B insert and the GPRP motif. Ribbon-type representation of the DNM1L monomer showing the localization of the B insert and the GPRP motif, and the known post-translational modifications (black, green, magenta), respectively. The first and the last visible residues of the B insert and L2^S are indicated as spheres.

lysines in the two clusters, four of which are located in the differentially spliced regions of DNM1L. DNM1L is modified by SUMOylation by all three SUMO isoforms. The E2 SUMO-conjugating enzyme Ubc9 binds to the G domain and the B insert of DNM1L. Two phosphorylation sites are described at serine 590 and at serine 611 [156-160], both of which are located within the B insert, too. Phosphorylation of S590 was shown to induce mitochondrial scission [156] and CaMKIα-dependent phosphorylation of S611 was shown to facilitate its interaction with Fis1 thereby targeting DNM1L to the mom leading to increased mitochondrial fission (Han *et al.*, 2008) An S-nitrosylation site was found at C618 which is located in $\alpha 4^S$ in close proximity to the C terminal end of the B insert. S-nitrosylation of C618 was reported to play a role in Alzheimer's disease although these findings are controversially discussed [24, 25].

3.3.   Structure-based mutational analysis

3.3.1.   Stalk interface 2 mediates dimerization

The four DNM1L molecules in the asymmetric unit assembled into two dimers via a symmetric interface of 1000 Å^2 in the center of the stalks (Figure 34A, C). This dimerization interface includes hydrophobic contacts in the center and salt bridges at the periphery, resulting in an X-shaped stalk dimer. Residues in this interface are highly conserved in dynamin and partially conserved in MxA (Figure 35). Accordingly, a similar X-shaped stalk dimer assembled via interface 2 was found in dynamin (Figure 10B) and MxA (Figure 14) [50, 68, 69].

To probe the functional relevance of interface 2 for assembly of DNM1L in solution, point mutations were introduced in the interface and analytical ultracentrifugation (AUC) and analytical gelfiltration experiments (see 2.3.13) in combination with right angle light scattering (RALS) were performed (see 2.3.14). DNM1L in solution was in a dynamic oligomerization equilibrium (Figure 37A). Also in RALS experiments, DNM1L displayed a dimer-tetramer equilibrium (Figure 37B). Mutations M482D, N635A or D638A led to aggregated or partially aggregated protein. However, introduction of a charge reversal in the center of interface 2 by the K642E and E490R mutations interfered with dimerization, resulting in a mostly monomeric species, whereas the E490A mutation had no effect on the native assembly (Figure 37A, B).
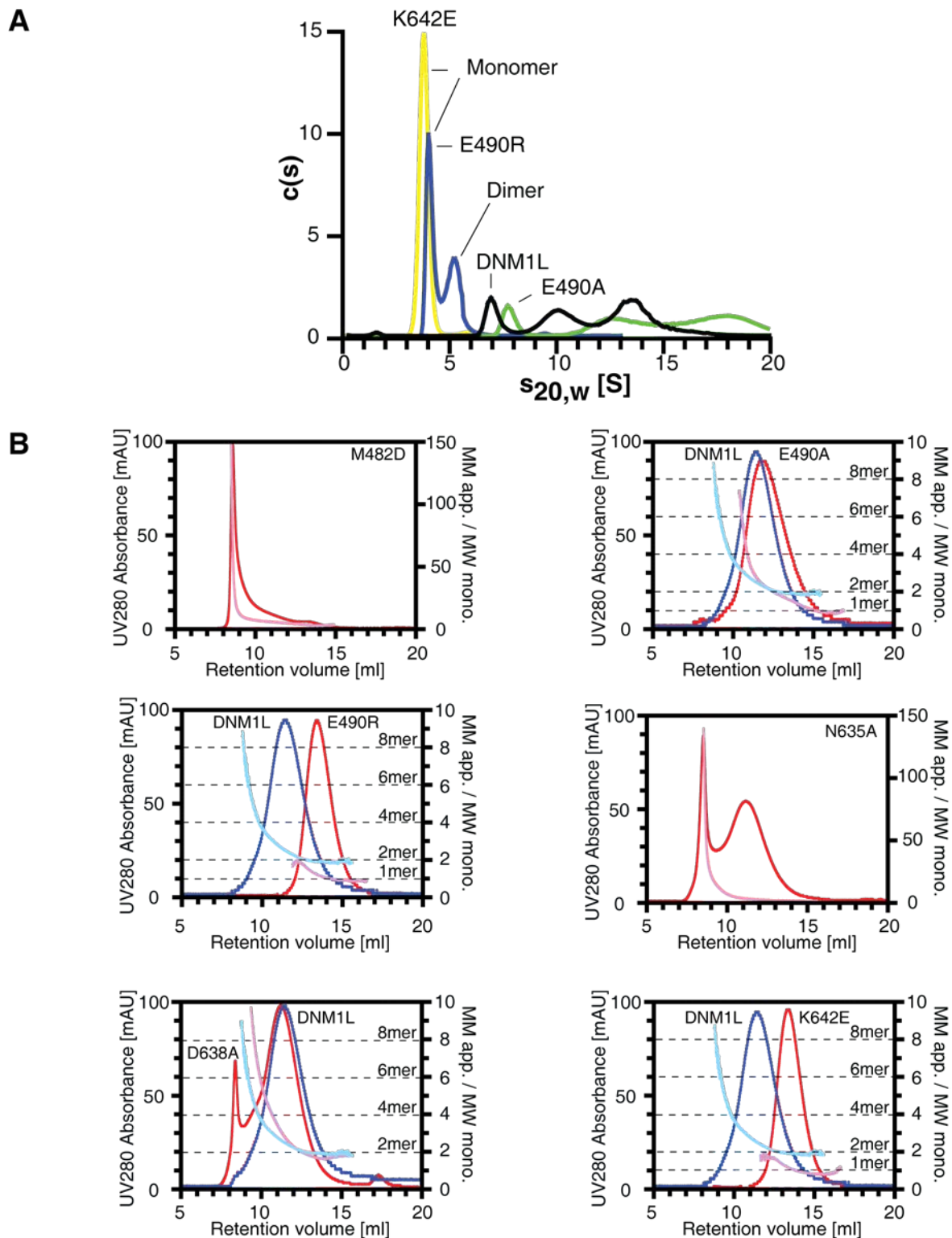
Figure 37: RALS and AUC data of DNM1L interface 2 mutants. **A:** Analytical ultracentrifugation sedimentation velocity experiments for DNM1L and indicated mutants. Plotted is the relative protein concentration c(s) as function of the normalized sedimentation coefficient $s_{20,w}$. Monomer and dimer peaks for E490R and K642E are indicated. Peaks in the wild type sedimentation profile could not be assigned to single oligomeric species as the protein is in a fast equilibrium between different oligomeric states. Similar to DNM1L, the E490A mutant undergoes rapid exchange reactions between different oligomeric species. **B:** Analytical gelfiltration experiments for DNM1L and indicated mutants. 0.2 mg of protein was separated on an analytical S200 10/300 GL column. The darker colored curves indicate the UV absorbance (see left y-axis). The calculated relative molecular masses as determined by RALS are shown in the corresponding lighter colors (see right y-axis). MM app / MW mono corresponds to the quotient of the apparent molecular mass divided by the molecular weight of the monomer.

To analyze oligomerization of DNM1L, sedimentation assays were performed, as previously established for MxA (see 2.3.15) [50]. In the nucleotide-free state, DNM1L was found predominantly in the supernatant after ultracentrifugation. Addition of GDP had no effect on the sedimentation whereas addition of GTP-γ-S led to the formation of higher-order oligomers which could be sedimented (Figure 38A, B). The monomeric K642E mutant sedimented only weakly, even after addition of GTP-γ-S, suggesting that higher order oligomerization requires an intact interface 2.

In liposome co-sedimentation assays, DNM1L bound to negatively-charged liposomes composed of phosphatidylserine (PS) (Figure 38A, B) or of a typical mitochondrial membrane mixture (Figure 38C) [8]. When analyzing the effects of different nucleotides, the greatest sedimentation differences in the absence and presence of liposomes were observed with GDP (Figure 38C), which was used in all further experiments (Figure 38A). In contrast to DNM1L, the K642E mutant co-sedimented only weakly with liposomes, underpinning the importance of dimerization via interface 2 for further oligomerization and/or liposome binding. We also tested liposome floatation assays to demonstrate membrane binding of DNM1L (Figure 38D). However, addition of DNM1L to PS liposomes prevented their floatation. This effect might be caused by extensive remodeling of these liposomes by DNM1L (see below).
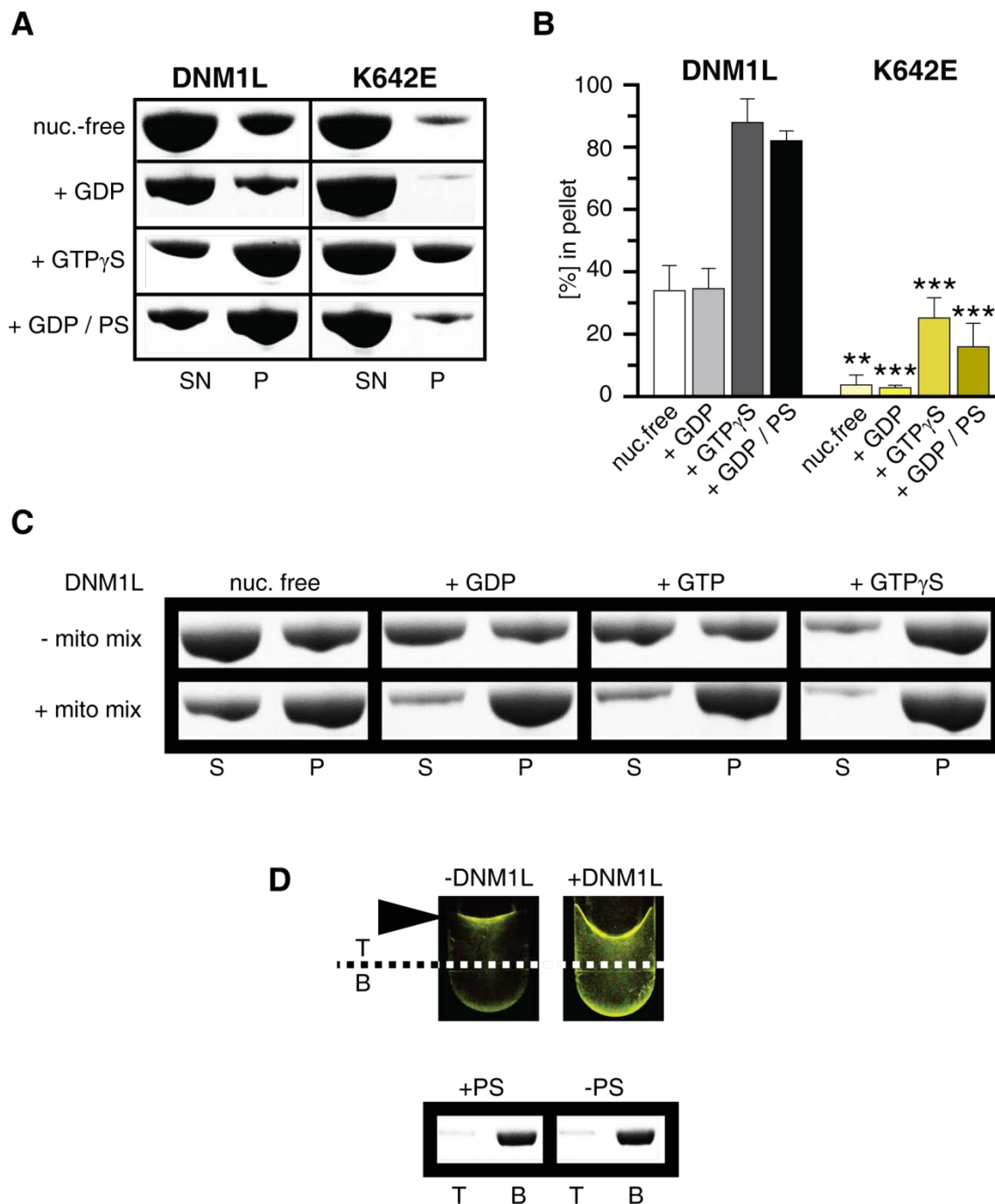
Figure 38: Sedimentation experiments and liposome binding assays for DNM1L and DNM1L K642E. **A:** Sedimentation experiments were performed in the absence and presence of 2 mM GTP-γ-S in the absence of liposomes. Liposome co-sedimentation assays were carried out in the presence of 2 mM GDP, and in the presence or absence of PS liposomes. Lanes are representative for three independent experiments. Boxed lanes are from the same gel. P, pellet fraction; SN, supernatant. **B:** Quantification of sedimentation and liposome binding assays (n = 3 for each experiment, error bars represent the SEM). Bars show percentage of protein found in the pellet with respect of total protein applied on gel. The statistical significance was calculated with respect to the corresponding DNM1L experiments. *** - p < 0.001; ** - p < 0.01. **C:** Nucleotide-dependent co-sedimentation of DNM1L with liposomes composed of 40% phosphatidylcholine, 30% phosphatidylethanolamine, 10% phosphatidylinositol 4,5-bisphosphate, 10% cardiolipin, 5% phosphatidylserine, and 5% phosphatidic acid. The greatest sedimentation difference in the absence and presence of liposomes was observed with GDP. **D:** Upper panel: Floatation assay with 100 µM PS liposomes spiked with 1% dansyl-labeled PS in the absence and presence of DNM1L. Floatation assays were carried out in a 1:80 protein:lipid molar ratio. Two different floatation agents (sucrose and Accudenz) and two different temperatures (4 °C and 20 °C) were tested and showed the same results. After centrifugation for 1 h at 200,000 x g, fluorescent liposomes were visualized by UV. Whereas PS liposomes on their own floated under these conditions (visible as sharp line, as indicated by the arrow), addition of DNM1L led to a disperse distribution of the liposomes in the test tube. Lower panel: SDS-PAGE showing the distribution of DNM1L in the top (T) and bottom (B) fractions in the absence and presence of PS liposomes.

DNM1L showed a low basal GTP hydrolysis rate of 1.5 min^{-1} which was stimulated approximately 10-fold in the presence of PS liposomes (see 2.3.12) (Figure 39). This stimulated GTPase rate is still 20-fold slower than the maximal reported GTPase rate of dynamin under similar conditions [55, 68]. Interestingly, this extent of GTPase stimulation was only observed at low (0.5 mM), but not at high (>2 mM) MgCl$_2$ concentrations (Figure 40A). This effect is likely related to the observed fusion and aggregation of PS-liposomes at higher MgCl$_2$ concentrations (Figure 40B).

The K642E mutant displayed a similar basal GTPase rate, but only 2.5-fold stimulated GTPase activity at 0.5 mM MgCl$_2$ in the presence of liposomes, confirming the importance of assembly via interface 2 for membrane binding and the resulting GTPase activation (Figure 39).
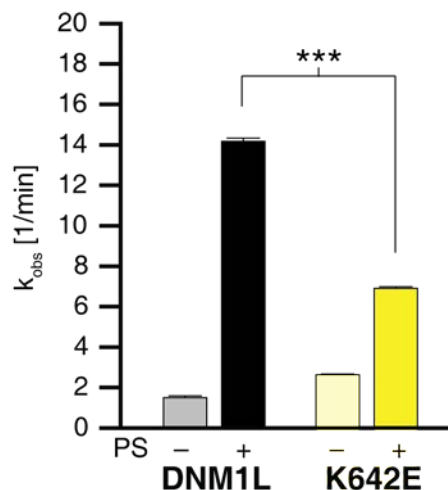
Figure 39: GTPase activity of DNM1L and one DNM1L interface 2 mutant. Basal and PS liposome-stimulated GTPase activities of DNM1L and the K642E mutant were determined at 37 °C (n=3 for each experiment, error bars represent the SEM). The statistical significance was calculated with respect to the corresponding DNM1L experiments. *** - p < 0.001.

_____
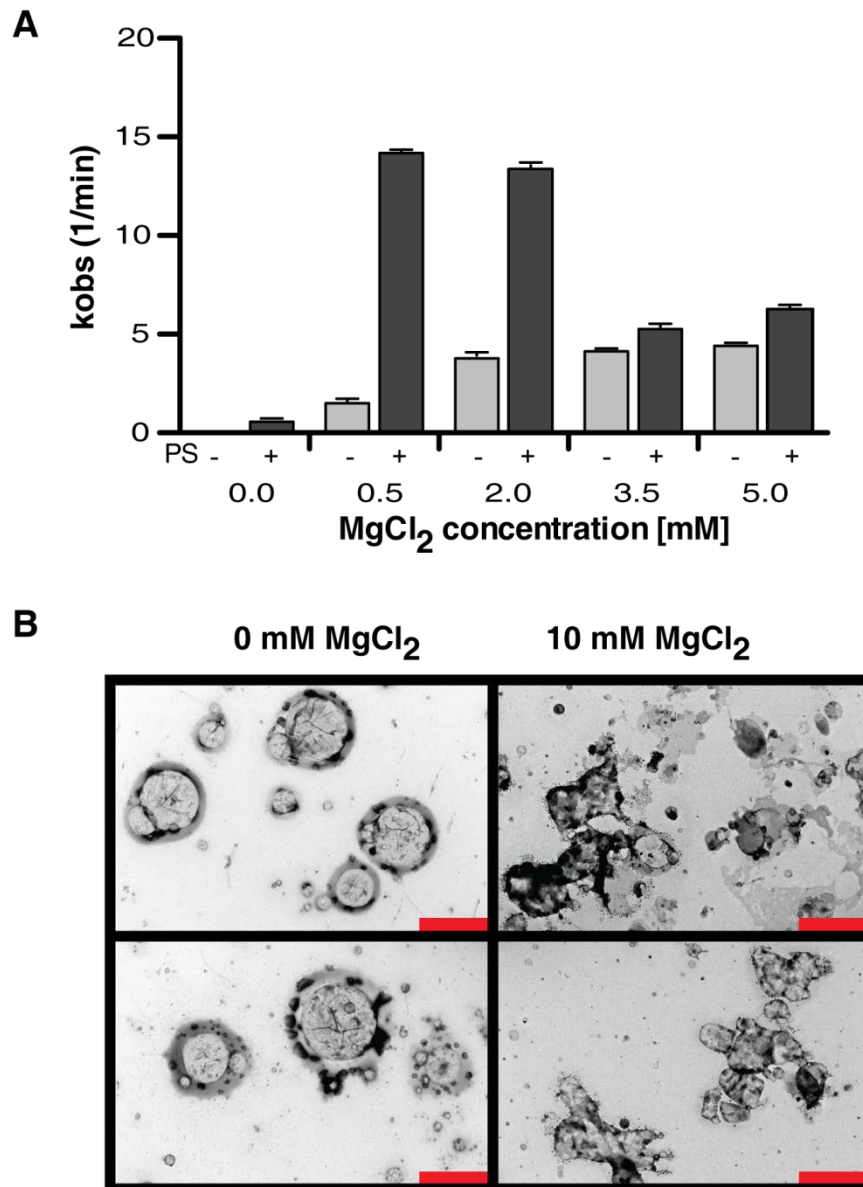
Figure 40: MgCl$_2$-dependent GTPase activity of DNM1L and MgCl$_2$-dependent liposome deformation **A:** MgCl$_2$-dependent GTPase activity of 10 µM DNM1L in the absence and presence of 0.5 mg/ml PS liposomes was analyzed at a GTP concentration of 1 mM and increasing MgCl$_2$ concentrations. Initial GTPase rates from three independent reactions were determined by an HPLC-based assay. **B:** Representative micrographs of negatively-stained PS liposomes in the absence and presence of 10 mM MgCl$_2$. At 10 mM MgCl$_2$, PS liposomes fuse and aggregate. Scale bar = 5 µm.
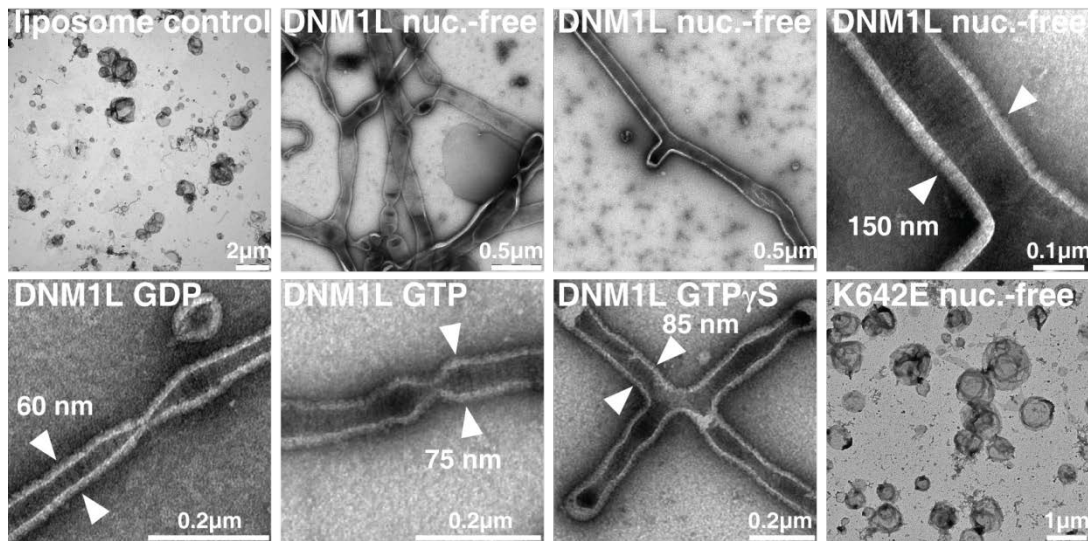
Figure 41: Liposome tubulation assays of DNM1L and one interface 2 mutant. Negative-stain electron microscopic analysis of DNM1L in the presence of PS liposomes and different nucleotides. The K642E mutant did not show any tubulation in the absence and presence of nucleotides.

In the absence of nucleotides, DNM1L deformed PS liposomes into long tubular structures and formed a tight protein coat with pronounced striations around the liposomes, as observed in negative-stain EM (see 2.3.17) (Figure 41). These oligomers had a diameter of 130 - 150 nm, similar to that of yeast Dnm1 oligomers [118]. In the presence of GTP-γ-S, the oligomer constricted to approximately 85 nm, and further constricted in the presence of GTP and GDP to approximately 75 nm and 60 nm, respectively, similar to the results reported for yeast Dnm1 [118]. The K642E mutant was unable to deform liposomes either in the absence or presence of nucleotides (Figure 41), indicating the importance of interface 2 for membrane binding and/or remodeling.

To analyze the function of interface 2 *in vivo*, mitochondrial dynamics and morphology were analyzed (see 2.5.2) in the monkey kidney-derived fibroblast cell line COS-7 (see 2.1.5) [108]. Mitochondria were labeled by expression of a red fluorescent protein targeted to the mitochondrial lumen (mito-dsRed, see 2.1.6). In control cells, mitochondria showed both punctate and elongated shapes (Figure 42A, upper left). siRNA depletion of endogenous DNM1L induced the formation of long interconnected mitochondrial networks and perinuclear clusters (Figure 42A, upper right), in agreement with previous results [161]. Upon expression of an siRNA
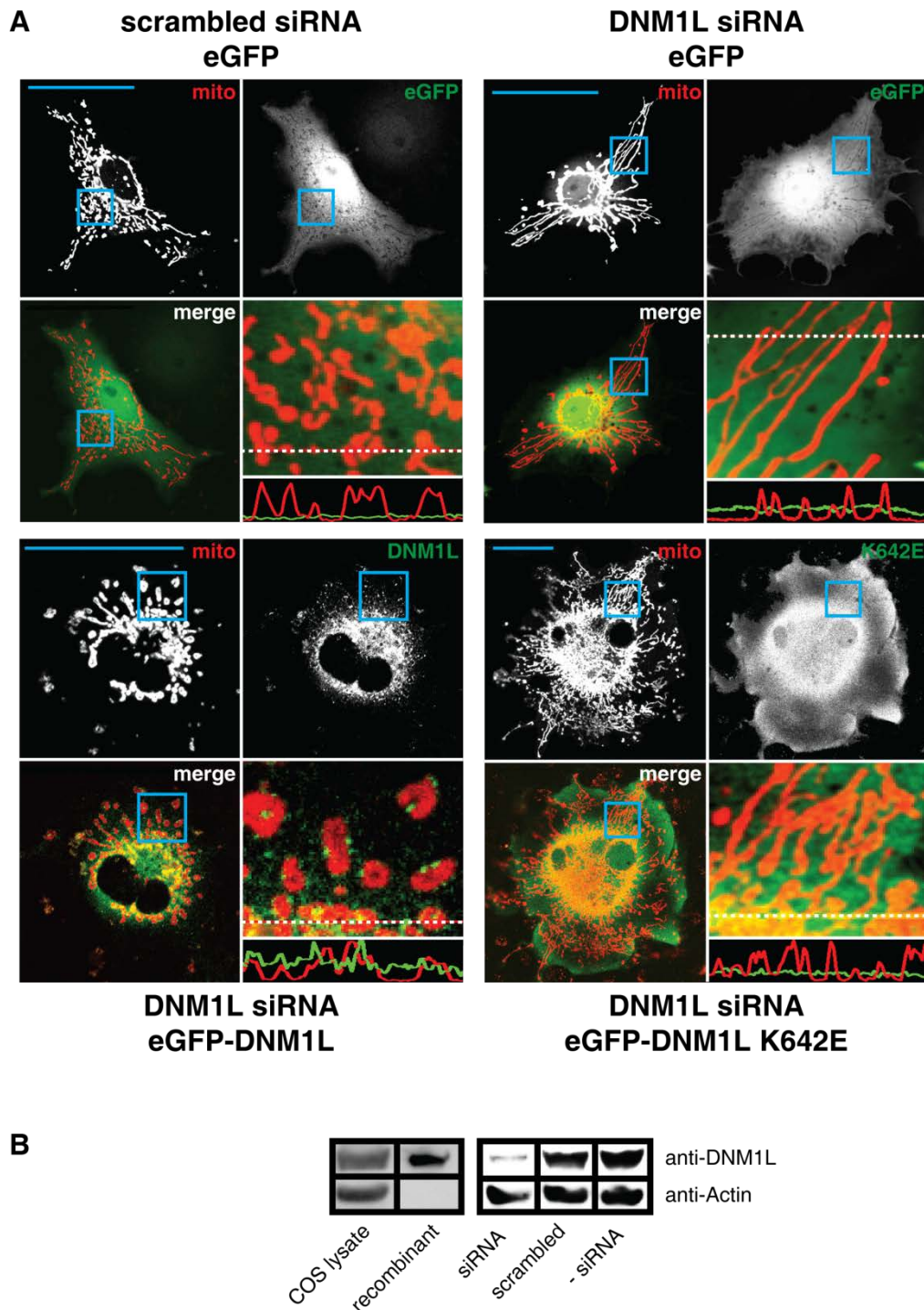
Figure 42: *In vivo* functional assays of DNM1L and one interface 2 mutant. **A:** Cellular localization and mitochondrial morphology studies in mito-dsRed expressing COS 7 cells. Cells depleted of DNM1L by siRNA were co-transfected with GFP, siRNA-resistant GFP-DNM1L or GFP-DNM1L K642E, respectively. Scrambled siRNA and co-transfected GFP was used as a control. Magnified boxed regions and a line scan plot with the relative fluorescence of the indicated GFP constructs and mito-dsRed are shown to the lower right of each subpanel. Scale bars: 50 µm. **B:** Western blot showing efficient siRNA-mediated knock down of endogenous DNM1L. Scrambled siRNA was used as a control. Actin was stained as a loading control. Antibody efficiency was monitored using a COS cell lysate and recombinant DNM1L in a separate Western Blot.

resistant eGFP-tagged DNM1L construct, the protein was found in punctate structures which mostly co-localized with mitochondria (Figure 42A, lower left). Transfection of this construct led to a reduced length of mitochondrial tubules which appeared even more fragmented than in control cells. In contrast, eGFP-tagged DNM1L K642E did not localize to mitochondria but was diffusely distributed throughout the cytosol. Accordingly, the K642E mutant also did not rescue the aberrant mitochondrial phenotype induced by DNM1L depletion (Figure 42A, lower right). These results indicate a role of stalk dimerization for the recruitment of DNM1L to the mitochondrial membrane.

To quantify these experiments, fluorescence recovery after photobleaching (FRAP) experiments were established (see 2.5.3) (Figure 43) [162]. Mito-dsRed was photobleached in a circular region of interest (ROI) and fluorescence recovery followed over time. In control cells, only a small percentage of fluorescence recovered within 90 sec, indicating only marginal connectivity of mitochondria in and outside the ROI. However, upon down-regulation of DNM1L by siRNA, fluorescence rapidly recovered to 67 % of the pre-bleach value (Figure 43). In these cells, the elongated mitochondrial network extended beyond the ROI, allowing fast diffusion of dsRed within the mitochondrial lumen. Expression of siRNA-resistant DNM1L in
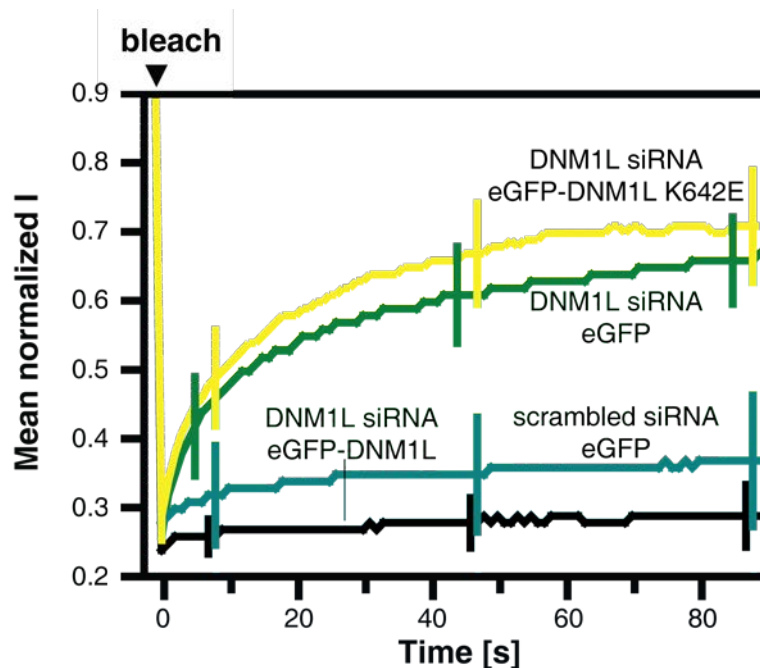
Figure 43: FRAP assay for mitochondrial network connectivity of DNM1L and one interface 2 mutant. Mito-dsRed in an ROI (d = 6 μm) containing multiple mitochondria was photobleached and its fluorescence recovery monitored for 90 s. Curves show mean values from 20 independent experiments under the indicated conditions. Pre-bleach intensities were normalized. For clarity, only three representative error bars are shown for each experiment.

DNM1L in DNM1L-depleted cells decreased the extent of fluorescence recovery to a value slightly lower than that of control cells (Figure 43). Expression of the K642E mutant, however, did not revert the high FRAP recovery rate in DNM1L-depleted cells (Figure 43). We conclude that dimerization of the stalk via interface 2 is crucial for the function of DNM1L in catalyzing mitochondrial division.

3.3.2. Functional importance of the B insert and the GPRP motif

To test the importance of these two structural elements (see 3.2.4), the 4A mutant carrying a quadruple alanine mutation and the ΔB mutants lacking the B insert (aa 514-613) were functionally analyzed. AUC (see 2.3.13) and RALS experiments (see 2.3.14) showed that the 4A mutation led to a dimeric DNM1L species which was unable to further oligomerize. However, deletion of the B insert did not interfere with formation of higher ordered oligomers, although oligomerization appeared somewhat reduced (Figure 44A+B).
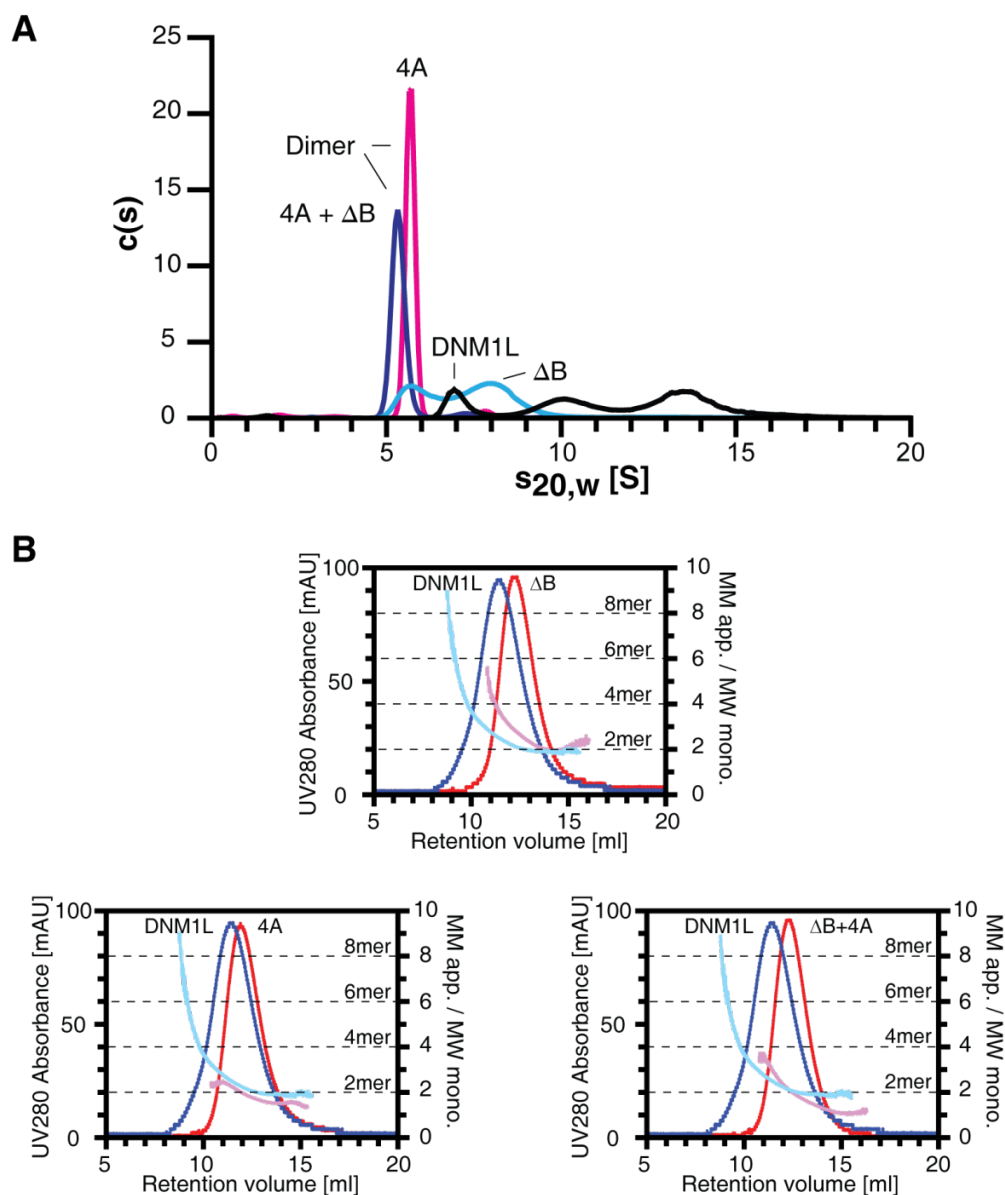
Figure 44: RALS and AUC data of the DNM1L 4A mutant, the ΔB insert construct and the combined mutant. **A:** Analytical ultracentrifugation sedimentation velocity experiments for DNM1L, DNM1L ΔB-insert, DNM1L 4A and the combined mutant (4A + ΔB) as described in Figure 37. Dimer-peaks for DNM1L 4A and the combined mutant are indicated. Peaks in the wild type sedimentation profile could not be assigned to single oligomeric species as the protein is in a fast equilibrium between different oligomeric states. **B:** Analytical gelfiltration experiments for DNM1L and indicated mutants as shown in Figure 37B.
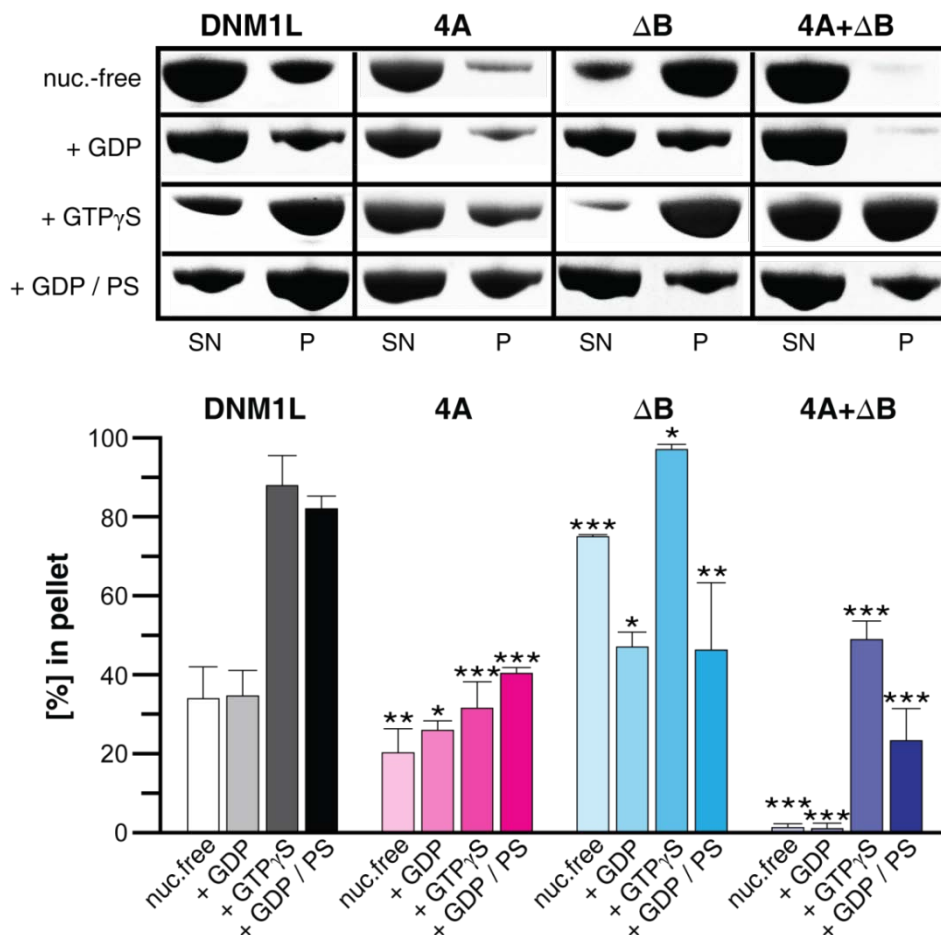
Figure 45: Sedimentation experiments and liposome binding assays for DNM1L, the 4A mutant, the ΔB insert construct, and the combined mutant. Upper panel: Oligomerization experiments and liposome binding assays as in Figure 38A for DNM1L, DNM1L ΔB insert, DNM1L 4A and the combined mutant (4A+ΔB). Lanes are representative for three independent experiments. P, pellet fraction; SN, supernatant. Lower panel: Quantification of sedimentation and liposome binding assays as in Figure 38B (n = 3 for each experiment, error bars represent the SEM). *** - $p < 0.001$; ** - $p < 0.01$; * - $p < 0.05$.

In oligomerization assays (see 2.3.15), the 4A mutant assembled with reduced efficiency compared to DNM1L (Figure 45). Similar to the corresponding mutation in MxA [50], some residual assembly was still observed in the presence of GTP-γ-S, suggesting that the 4A mutation on its own is not fully disruptive. Liposome co-sedimentation was also diminished. In line with the AUC data (Figure 44A), these observations support a model in which interface 3 (i.e. L2^S) mediates oligomerization as a prerequisite for membrane binding.

In oligomerization assays, the ΔB variant sedimented already in the absence of nucleotide (Figure 45). This might be explained by to the lower solubility of this mutant which was also apparent during its purification. Addition of GTP-γ-S further enhanced sedimentation (Figure 45). In contrast, GDP-binding partially stabilized this protein, as previously reported for other GTPases [163]. This variant showed no enhanced sedimentation in the presence of liposomes.
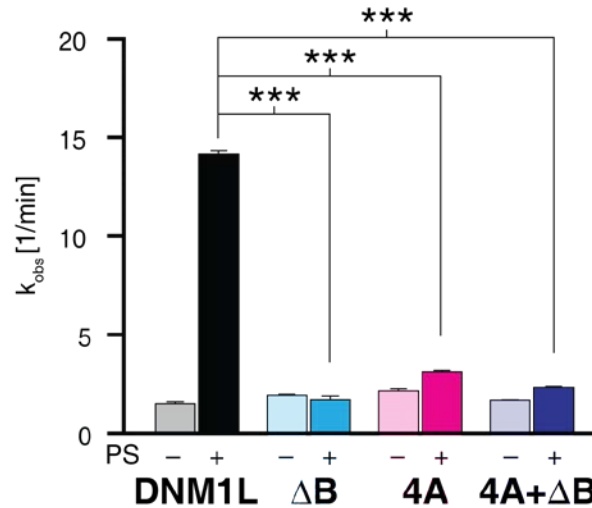
Figure 46: GTPase activities for DNM1L, the 4A mutant, the ΔB insert construct, and the combined mutant. Basal and PS liposome-stimulated GTPase activities of DNM1L and DNM1L mutants were determined at 37 °C (n = 3 for each experiment, error bars represent the SEM). *** - p < 0.001.

Interestingly, the crystallized double mutant (ΔB + 4A) did not sediment at all in the absence of nucleotides and presence of GDP. As the 4A mutant, it still showed some residual sedimentation in the presence of GTP-γ-S and liposomes. Whereas the basal GTPase activity (see 2.3.12) of the 4A, ΔB and the (4A + ΔB) variants lay in a similar range to that of DNM1L, none of the mutants showed a significant GTPase activation in the presence of PS liposomes. Furthermore, neither the 4A nor the ΔB variants were able to tubulate liposomes (see 2.3.17) (Figure 47). These data indicate an essential role of the GPRP motif and the B insert for ordered assembly of DNM1L on membrane surfaces, concomitant with GTPase stimulation.

When expressed in DNM1L-depleted COS-7 cells, both the 4A and ΔB mutants failed
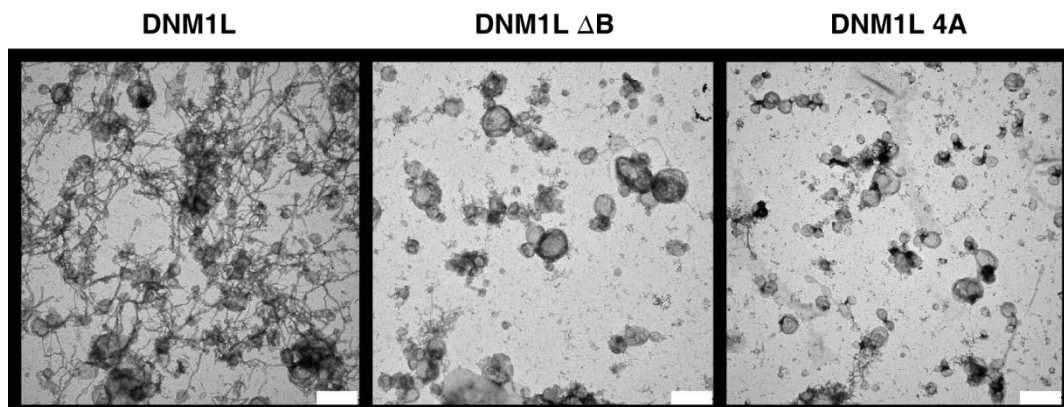
Figure 47: Liposome tubulation assays of DNM1L, the 4A mutant, and the ΔB insert construct. Representative negative-stain electron micrographs of nucleotide-free DNM1L, DNM1L ΔB and DNM1L 4A in the presence of PS liposomes and absence of nucleotides, respectively. Unlike DNM1L, neither mutant tubulated liposomes above background. Scale bar = 2 μm.
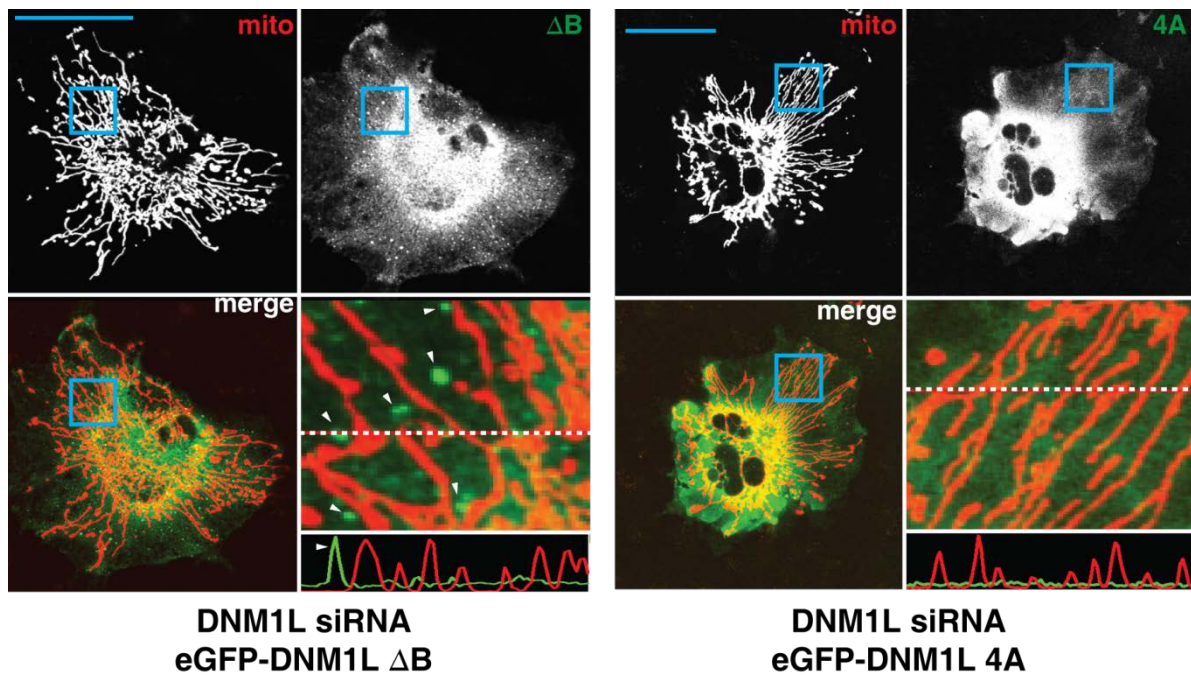
Figure 48: *In vivo* functional assays of DNM1L ΔB and the 4A mutant. Cellular localization and mitochondrial morphology studies as in Figure 42. COS7-cells depleted of DNM1L by siRNA were co-transfected with mito-dsRed and siRNA-resistant DNM1L ΔB-insert and DNM1L interface 3 mutants. Magnified boxed regions and a line scan plot with the relative fluorescence of the indicated eGFP fusion proteins and mito-dsRed are shown at the lower right of each subpanel. Scale bars: 50 μm.

to localize to mitochondria (Figure 48). Instead, the 4A mutant was diffusely present in the cytoplasm, whereas the ΔB mutant was found in large punctate aggregates distributed in the cytoplasm (Figure 48, left panel, white arrowheads). Neither mutant was able to revert the aberrant mitochondrial morphology of DNM1L-depleted cells. In the FRAP-based quantification assay, mito-dsRed-labeled mitochondria in the presence of both mutants showed a high degree of fluorescence recovery after bleaching, underpinning the inability of these DNM1L mutants to catalyze mitochondrial fission (Figure 49). Thus, both the B insert and interface 3 are required for the function of DNM1L in catalyzing mitochondrial fission.

_____
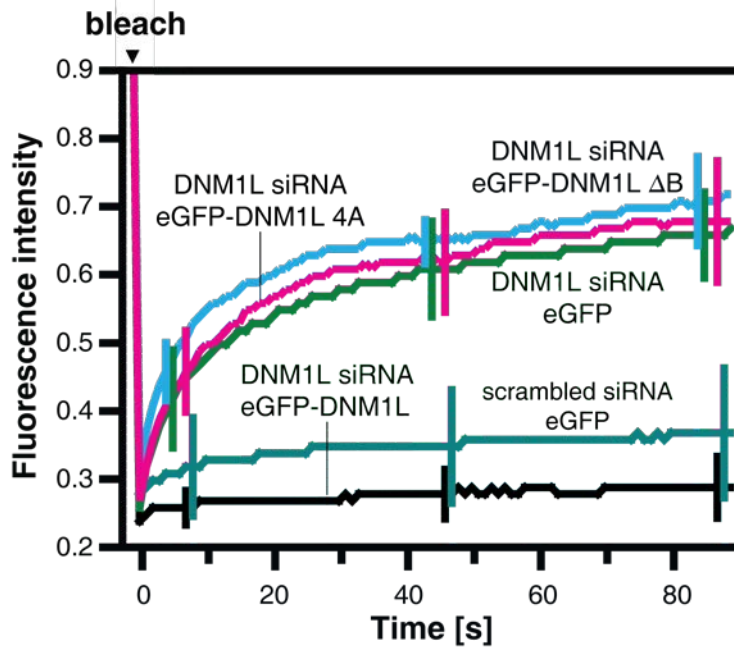
Figure 49: FRAP assay for mitochondrial network connectivity of DNM1L, DNM1L ∆B and the 4A mutant. Mitochondrial network connectivity quantified by a FRAP assay, as in Figure 43.

3.3.3. Stalk interface 4 is important for liposome tubulation *in vitro* and mitochondrial remodeling *in vivo*

To analyze the functional relevance of interface 4, individual mutations E426A and R430D were introduced (see 2.2.10) to break off salt bridges between R430/E426 and R430/D382 (Figure 34D). Unlike DNM1L K642E or DNM1L E490R (Figure 37A, B), E426A or R430D mutations did not alter the assembly status in solution. When analyzed in AUC (see 2.3.13) and RALS (see 2.3.14) experiments both mutants exhibit similar rapidly interchanging oligomeric species as native DNM1L (Figure 50A). RALS experiments for E426A and R430D resulted in almost identical elution profiles when compared to native DNM1L (Figure 50B).
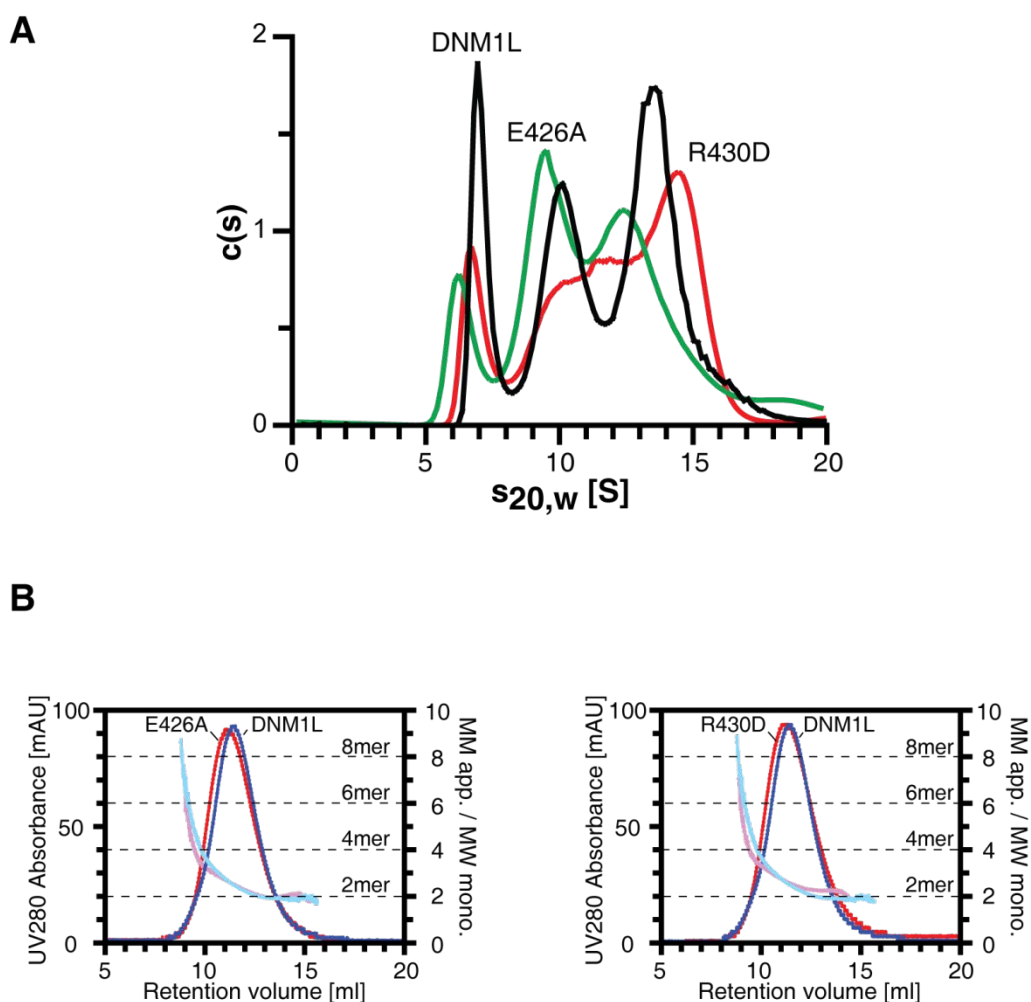
Figure 50: RALS and AUC data of two DNM1L interface 4 mutants **A:** Analytical ultracentrifugation sedimentation velocity experiments for DNM1L, DNM1L E426A, and DNM1L R430D as described in Figure 37A. All three samples contain rapidly interchanging oligomers. Therefore, the peaks could not be attributed to individual oligomeric species. **B:** Analytical gelfiltration experiments for DNM1L and indicated mutants as shown in Figure 37B.
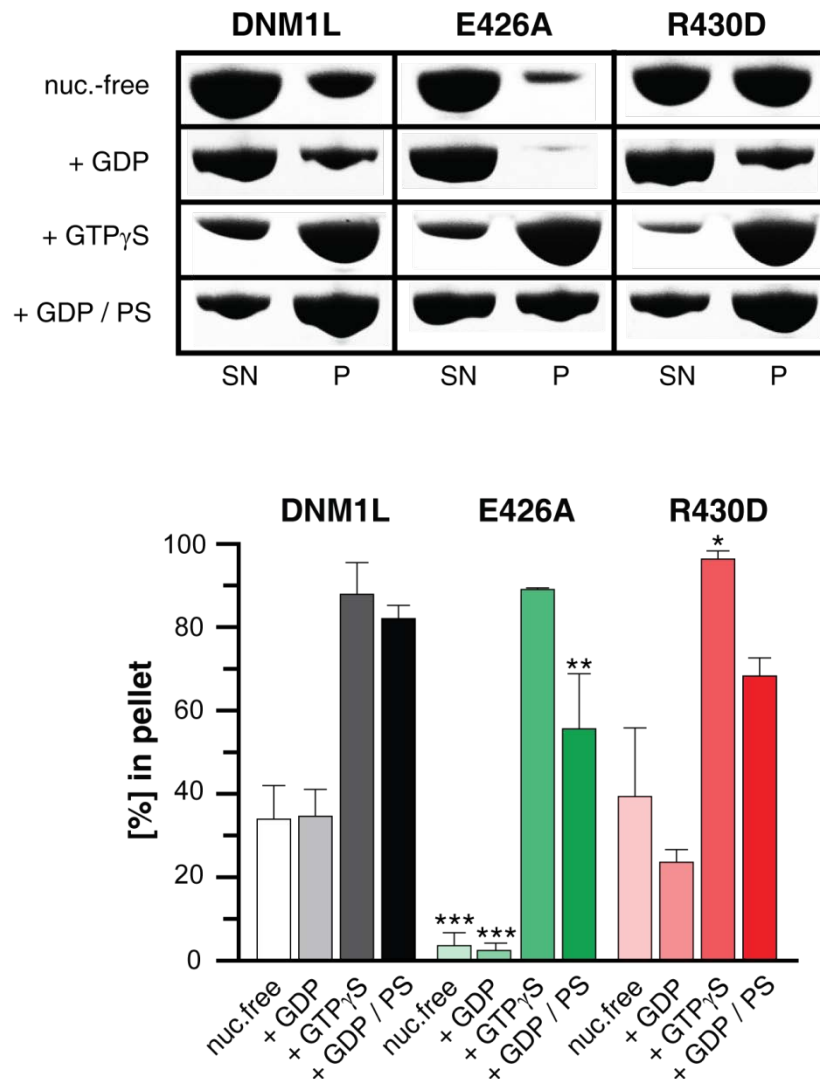
Figure 51: Sedimentation experiments and liposome binding assays for DNM1L and two DNM1L interface 4 mutants. Upper panel: oligomerization experiments and liposome binding assays for DNM1L and interface 4 mutants (E426A, R430D), as in Figure 38A. Lanes are representative of three independent experiments. P, pellet fraction; S, supernatant. Lower panel: quantification of sedimentation and liposome binding assays as shown in Figure 38B. (n = 3 for each experiment, error bars represent the SEM). *** - p < 0.001; ** - p < 0.01; * - p < 0.05.

In oligomerization assays (see 2.3.15), R430D behaved as DNM1L, whereas the E426A mutant showed somewhat reduced sedimentation in the absence of nucleotide and presence of GDP, but not in the presence of GTP-γ-S (Figure 51). Both mutants showed slightly reduced liposome binding (Figure 51), but similar basal and liposome-stimulated GTPase rates (see 2.3.12) (Figure 52).

Strikingly, both mutants failed to tubulate liposomes (see 2.3.17), both in the presence and absence of nucleotide, and a regular protein coat was never observed on these liposomes (Figure 53). These results indicate that interface 4 is required for the formation of an ordered oligomeric coat during membrane remodeling processes.
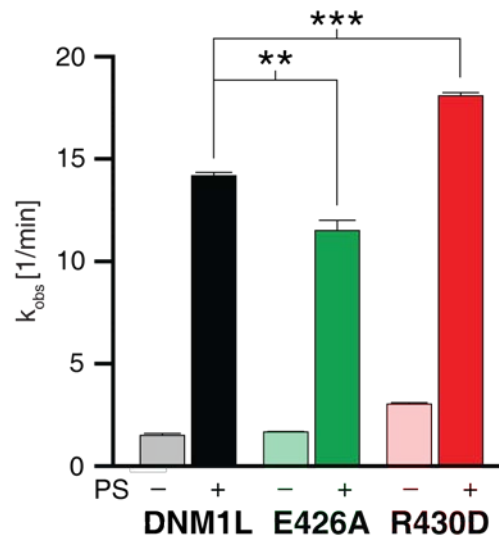
Figure 52:   GTPase assays for DNM1L and two interface 4 mutants. Basal and PS liposome-stimulated GTPase activities of DNM1L and interface 4 mutants were determined at 37 °C (n = 3 for each experiment, error bars represent the SEM). *** - p < 0.001; ** - p < 0.01.

When expressed in COS-7 cells (see 2.1.5) depleted of endogenous DNM1L (see 2.5.1), neither mutant localized to mitochondria and both failed to rescue mitochondrial morphology in DNM1L-depleted COS-7 cells (see 2.5.2) (Figure 54A),
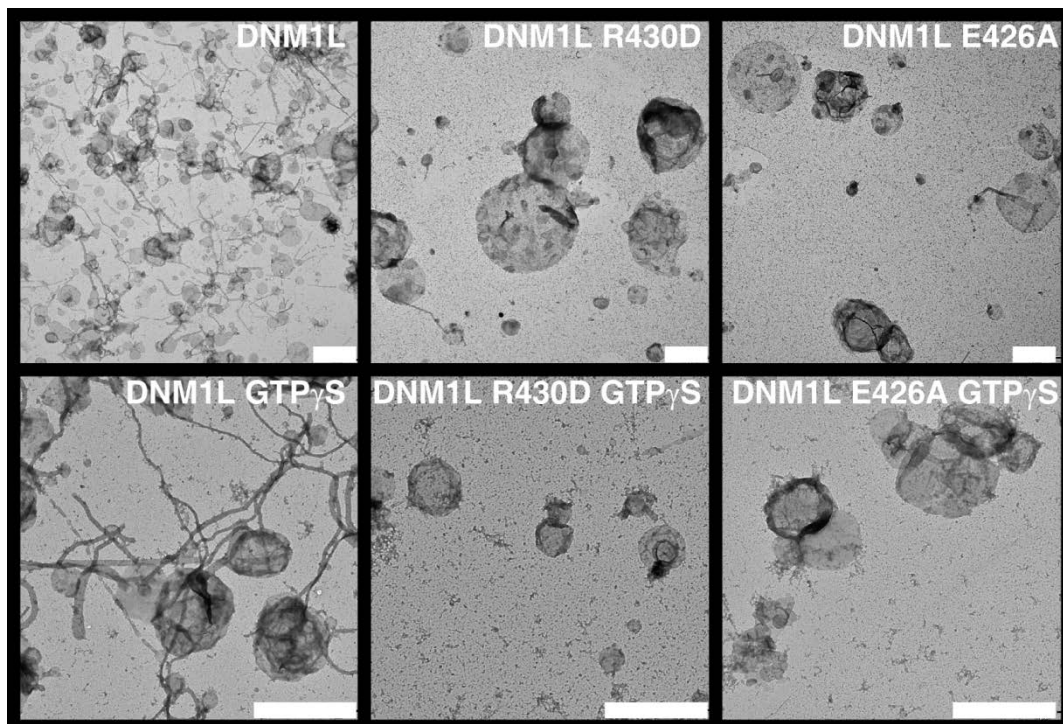
Figure 53   Tubulation assays for DNM1L and two interface 4 mutants. Representative images of negative-stain electron micrographs of DNM1L, DNM1L E426A and DNM1L R430D in the presence of PS liposomes. Neither interface 4 mutant tubulated liposomes, either in the absence or presence of nucleotides. Scale bar = 2 µm.
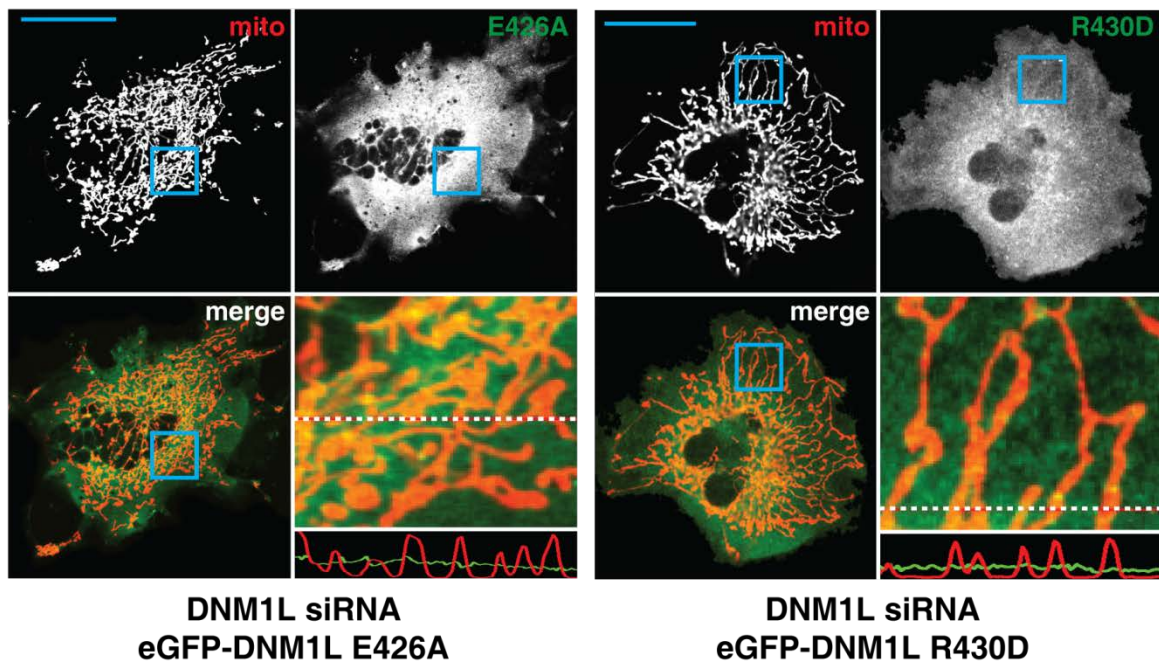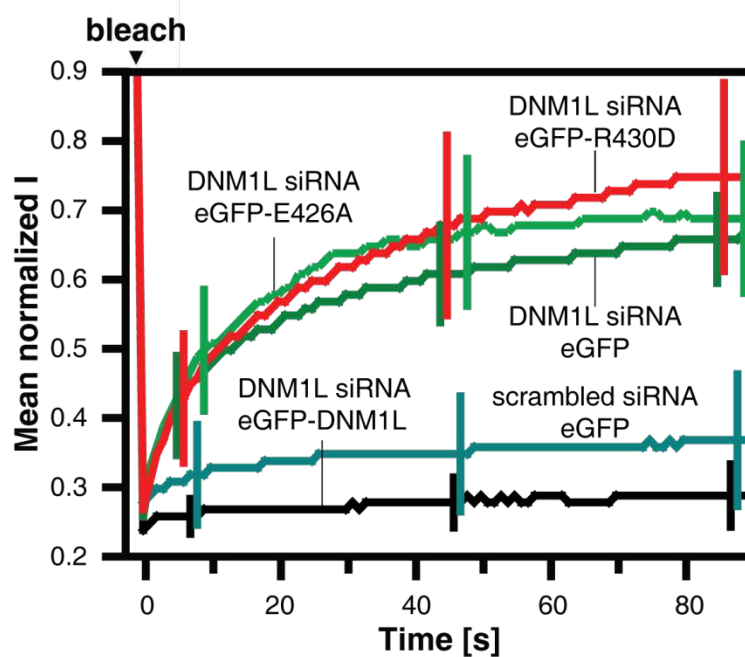
Figure 54: *In vivo* functional assays of DNM1L and two different interface 4 mutants. **A:** Cellular localization and mitochondrial morphology studies in COS-7 cells depleted of endogenous DNM1L by siRNA and co-transfected with mito-dsRed and siRNA-resistant interface 4 mutants, as in Figure 42A. Scale bars: 50 μm.   **B:** Mitochondrial network connectivity quantified by a FRAP assay, as in Figure 43.

which was confirmed by FRAP experiments (see 2.5.3) (Figure 54B). These results also indicate a role of interface 4 in the assembly at membrane surfaces and in mitochondrial division. They are consistent with a function of interface 4 as an additional assembly site (Figure 34B, D).

91

3.4.   A helical model for DNM1L assembly

To obtain further structural insights into DNM1L oligomerization, the DNM1L model was fitted into the EM reconstruction of nucleotide-free yeast Dnm1 (Figure 55A) [118]. The resolution of the EM reconstruction was not sufficient to unambiguously determine the orientation of DNM1L in the electron density. Therefore the following constraints were considered:

(1) As in dynamin and MxA, the G domains were assumed to be located in the outer layer of the oligomer. Since the B insert is likely unstructured, it is not expected to result in a defined electron density in the EM reconstruction. In agreement with previous suggestions [118] and similar to the PH domain in dynamin and the loop L4 in MxA [79], the B insert was placed at its predicted position at the tip of the stalk towards the observed gap between protein and liposome surface in the electron density. (2) Based on the mutagenesis data (see 3.3), it was assumed that DNM1L forms filaments similar to those of dynamin and MxA, employing stalk interfaces 1, -2 and -3. (3) It was hypothesized that the stalks assemble additionally via interface 4. (4) The helical spacing from the EM reconstruction was employed for the fittings.

Using these assumptions, an oligomeric model of DNM1L was constructed in which DNM1L dimers mediated via interface 2 assemble tangentially to the lipid tubule, as observed for dynamin and MxA. Instead of forming a one start filament, however, the stalks assemble with a neighboring stalk via interface 4 to form a double stalk filament (Figure 55A, B). These filaments further assemble via interface 1 and -3 to form a helix with a pitch of 14.4 nm. Two such double filaments, extending around the lipid tubule, account for the observed two start helix of 28.8 nm helical pitch (Figure 21). In this model, the G domains of each double stalk filament dimerize across helical turns with a neighboring filament allowing nucleotide-dependent rearrangements of adjacent filaments.

_____
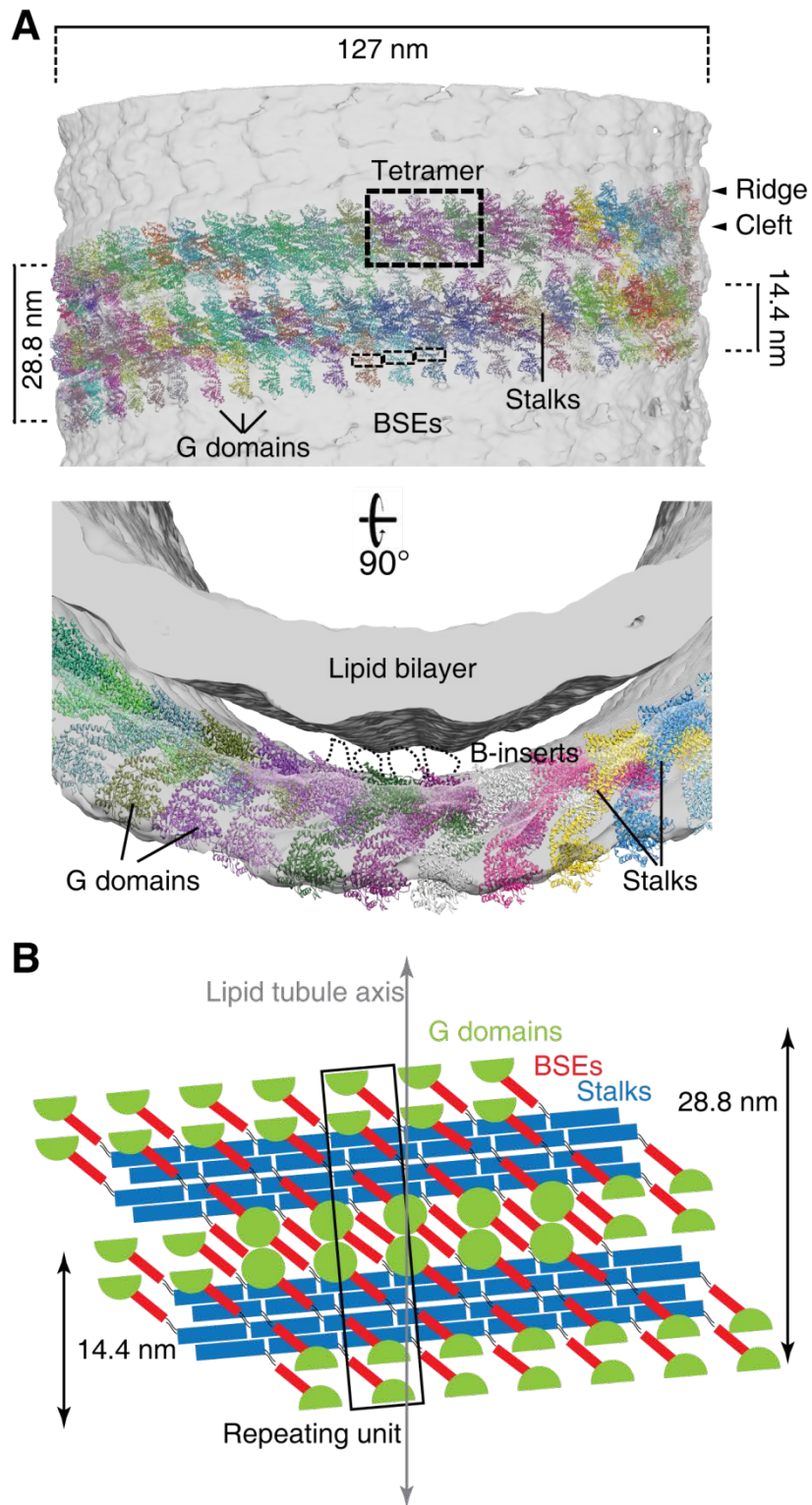
Figure 55: A helical model for DNM1L assembly. **A:** The DNM1L tetramer was manually fit into the EM reconstruction of yeast Dnm1 [118]. In this model, the stalks in the DNM1L tetramer are oriented tangentially to the lipid tubule with the B insert pointing towards the tubule. Oligomerization proceeds via interface 1 and 3, as in dynamin and MxA. Four stacked stalks via interface 2 and -4 build a filament which has a double width compared to filaments of dynamin and MxA. **B:** Schematic arrangement of the DNM1L molecules. The repeating unit of the reconstruction (boxed) contains 8 DNM1L monomers

4. Discussion

4.1. Similarities and differences in the assembly of dynamin superfamily proteins

Structural and functional studies of dynamin (see 1.3.1) and dynamin-like MxA (1.3.2) led to the identification of the stalk as the central assembly hub forming filaments via three distinct interfaces [50, 68-70, 79]. Similar to dynamin and MxA, the stalks of DNM1L assemble via the central interface 2 to form stable dimers which are the minimal building block of DNM1L oligomers (Figure 34A, C) [117]. Charge reversals in interface 2 lead to the formation of stable monomeric DNM1L variants (Figure 37). For dynamin, helix $\alpha 4^S$ of the stalk and/or $\alpha 3^B$ of the BSE were proposed to swap to a neighboring stalk/BSE thereby mediating dimerization [63, 65]. The existence of monomeric interface 2 mutants in DNM1L is not consistent with such a model for DNM1L. The liposome co-sedimentation data for interface 2 mutants also indicate that the affinity of a DNM1L monomer for membranes is low; at least two membrane interaction sites in the DNM1L dimer are required for efficient membrane recruitment (Figure 38A, B).

The mutagenesis data indicate that DNM1L dimers further oligomerize via interface 3 to form higher order assemblies (see 3.3.2). Consequently, mutations in the GPRP motif in loop $L2^S$ prevent formation of higher order oligomers in DNM1L (Figure 44). Interestingly, the G385E mutation next to loop $L1N^S$ of yeast Dnm1 [117, 164] and the corresponding G392D mutation in MxA [50] also prevent higher-order assembly leading to stable dimers. Faelber and colleagues previously suggested a model for interface 3 in dynamin which includes interactions from loops $L1N^S$ and $L2^S$ (see 1.3.1.7) [68]. The mutagenesis data for DNM1L indicate a similar architecture of interface 3. Also residues in interface 1 are highly conserved in dynamin, MxA and DNM1L (Figure 35). These observations strongly suggest that DNM1L uses a similar assembly mode as dynamin and MxA to form filaments via interface 1 and -3.

Finally, a novel assembly surface in the stalk was discovered. Via this interface 4, DNM1L dimers were stacked next to each other in the crystal (Figure 34B, D). This interface has not been observed for other dynamin family members (Figure 56). Mutants in interface 4 can still be recruited to liposomes (Figure 51) but fail to induce
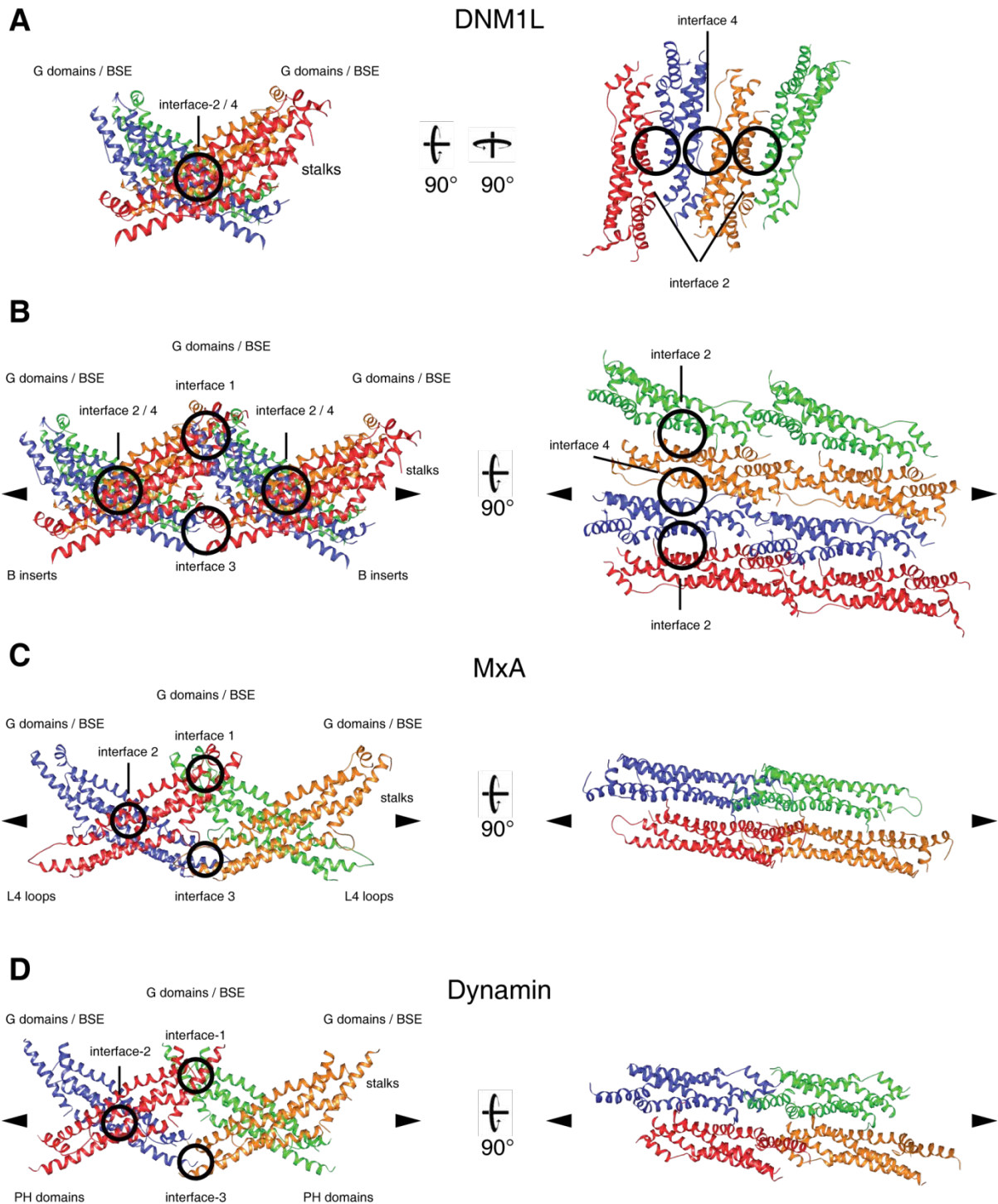
Figure 56: DNM1L contains one additional stalk interface (interface 4) compared to MxA and dynamin 1 **A:** Two views on the tetrameric arrangement of the DNM1L stalks mediated via interface 2 and interface 4, as observed in the asymmetric unit of the crystals. **B:** In the proposed oligomerization model of this study, stalks of a DNM1L tetramer further assemble via stalk interfaces 1 and 3 to form a filament. The width of the filament is determined by four adjacent stalks. **C:** Oligomerization model of MxA via the stalks (pdb 3LJB). Stalk dimers assembled via interface 2 further oligomerize via interface 1 and 3. In contrast to the DNM1L oligomerization model, this filament is composed of two, not of four, adjacent stalks. **D:** Dynamin (pdb 3SNH) filaments form in a similar fashion as in MxA involving a stalk dimer as building block.

membrane remodeling *in vitro* (Figure 53) and *in vivo* (Figure 54), suggesting that assembly via interface 4 is required for the formation of a stable membrane-anchored scaffold with membrane remodeling activity. This observation also points to an intrinsic, adaptor protein-independent functional deficit. Interestingly, the R376E mutation was recently reported to prevent DNM1L recruitment to mitochondria [153]. It was suggested that this mutation affects binding to the adaptor protein Mff (see 1.3.7.2). However, pull-down assays (data not shown) and isothermal calorimetry experiments (Figure 57), did not show a stable interaction of DNM1L and Mff. Arg376 is located in the direct vicinity of stalk interface 4 (see 4.4) and its mutation might thus affect the integrity of this interface.

Taken together the results of this study demonstrate interface 2, -3, and -4 being fundamental for the process of membrane remodeling *in vitro* and for the mitochondrial division process *in vivo*. Thus, DNM1L employs a modified assembly mode with respect to other dynamin superfamily members
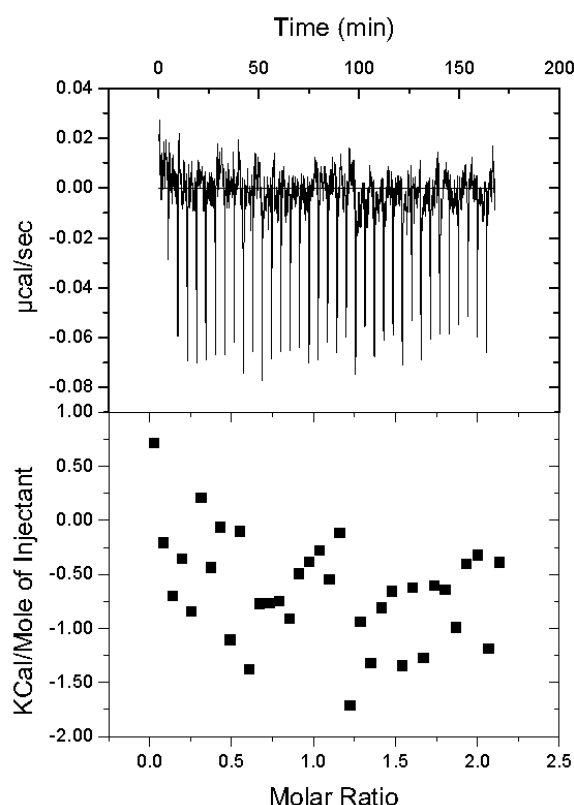
Figure 57:   ITC experiments of DNM1L versus Mff. Isothermal titration calorimetry experiment of Mff versus DNM1L did not show a stable interaction of DNM1L (cell) and Mff (syringe) as can be seen in the low energy change upon injection of Mff into the cell.

4.2.   Mechano-chemical coupling in DNM1L

Despite strikingly different cellular functions and only limited sequence identity (see appendix D) the domain architecture of DNM1L revealed common principles with dynamin 1 (see 1.3.1) and dynamin-like MxA (see 1.3.2). Either protein contains a N-terminal G domain, BSE, and a stalk and these domains are arranged in the same manner (Figure 58). Thus, proteins with similar structures can mediate such diverse processes like clathrin-mediated endocytosis (dynamin 1), antiviral host response (MxA), or the scission of mitochondria (DNM1L).

Structural and functional studies of dynamin (see 1.3.1.5) and MxA (see 1.3.2.3) led to the identification of the stalks as the central assembly hub forming filaments via three distinct interfaces [50, 68, 69]. The G domains, in turn, connect neighboring single stalk filaments via GTP-dependent dimerization across helical turns (Figure 59A). In contrast, the G domains of DNM1L connect neighboring double stalk filaments across helical turns (Figure 59B). The reduced GTPase activity of DNM1L compared to dynamin, despite the related architecture of the G domain, might indicate that the G domains employ a different mode of interaction across helical turns, where not all G domains of one tetrameric subunit are in register at the same time. Alternatively, the conformational changes in DNM1L oligomers induced by GTP
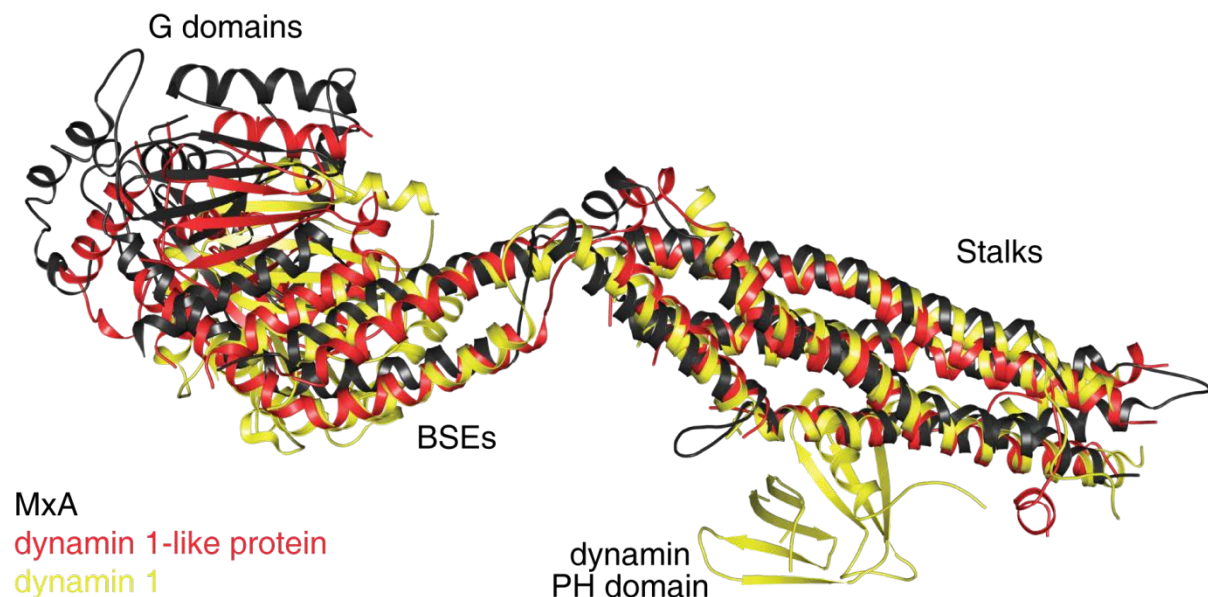
Figure 58:   Structural superposition of MxA (black), DNM1L (red), and dynamin 1 (gold). Besides the PH domain of dynamin 1, the domain arrangement of either of the proteins is very similar.
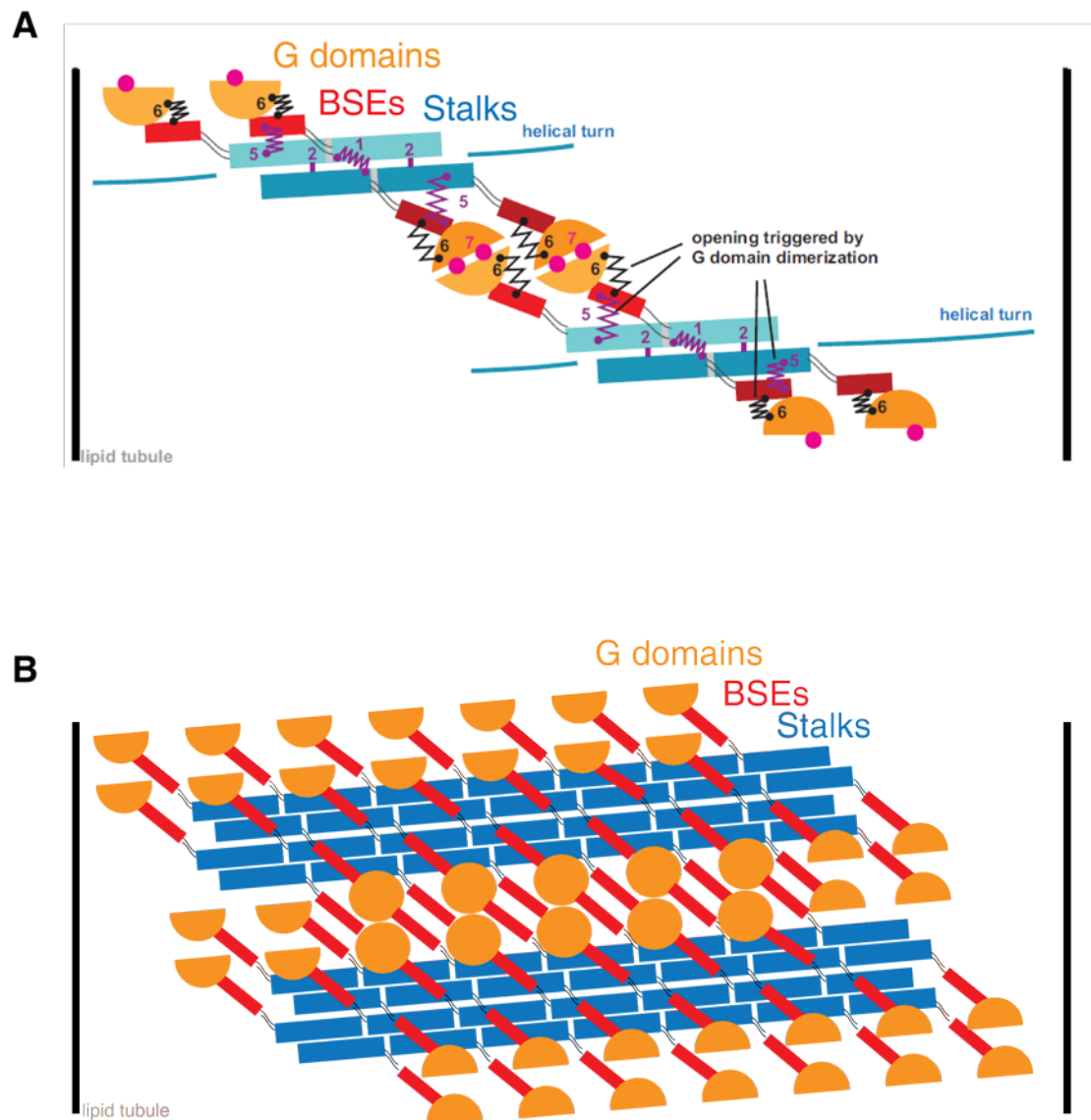
Figure 59: Different oligomerization modes for dynamin and DNM1L **A**: Oligomerization model of dynamin 1 on a lipid tube. When G domains of neighboring dynamin filaments dimerize, the BSE might be released from the stalk (e.g., opening of interface 5) and from the G domains (e.g., opening of interface 6). Figure taken from [70] **B:** Oligomerization model for DNM1L on a lipid tubule. For explanation, see text.

hydrolysis appear to be more dramatic [118] and might take longer compared to dynamin, thus reducing the hydrolysis rate of GTP.

The GTPase reaction is thought to drive a power stroke in the BSE [63, 65] which mediates the dynamic rearrangement of filaments leading to remodeling of the underlying membrane (see 1.3.1.3). In contrast to nucleotide-free dynamin 1 (Figure 11) no BSE-stalk interface was observed for DNM1L in the crystals. However, similar to dynamin and MxA a conserved interface of hydrophilic and hydrophobic contacts was observed between the G domain and the BSE of the same DNM1L molecule (Figure

31). This interface most likely adopts an regulatory function and - as observed for dynamin (Figure 08B) - opens upon GTP-dependent G domain dimerization (the power stroke).

Finally, the B insert is suggested to mediate mom binding of DNM1L as it is in an ideal position to dock DNM1L to the mom (see 3.4). Furthermore, it is located at an equivalent position like the lipid binding PH domain in dynamin or the substrate binding loop in MxA. Deletion of the B insert leads to dysfunctional DNM1L *in vitro* and *in vivo* (see 3.3.2). However, since the B insert had to be deleted to enhance crystallizability of DNM1L, its exact position in the structure is unknown. Thus, it remains to be elucidated if an interaction between the B insert and the stalk fulfills an autoinhibitory and / or regulatory function similar to that observed between the PH domain and the stalk in dynamin.

4.3.   DNM1L oligomers might be adapted to the size of mitochondria

Given the results of this study, a model is proposed where stalk interface 4 is used to assemble two neighboring DNM1L filaments (Figure 55). Such a model is in agreement with EM reconstructions of yeast Dnm1 showing a broader filament size (14.4 nm versus 10.6 nm) and different oligomer architecture compared to dynamin [118] (Figure 60). Since the basic architecture of such DNM1L and dynamin filaments is similar, this model would allow a related mechanism for DNM1L in membrane constriction involving G domain dimerization of double filaments across helical turns, leading to GTP hydrolysis and dynamic rearrangements.

The proposed double helical filament mediates a higher degree of mechanical stability which might be necessary for constricting mitochondria. Thus, the architecture of the stalk filament might be an adaption to the relevant lipid template. The neck of a clathrin-coated vesicle has a typical diameter of 40 nm [165] and can be encircled by approximately 14 dynamin dimers. Electron microscopic studies indicated that mitochondrial constriction sites have diameters of about 110 nm [117]. The model proposed here predicts that around 48 tetramers are assembled around a mitochondrial constriction site. The diameter of non-constricted mitochondria is even higher; typically around 0.5 µm [166]. To apply force on a membrane template of this size for membrane constriction and scission, a more rigid filament might be required

_____
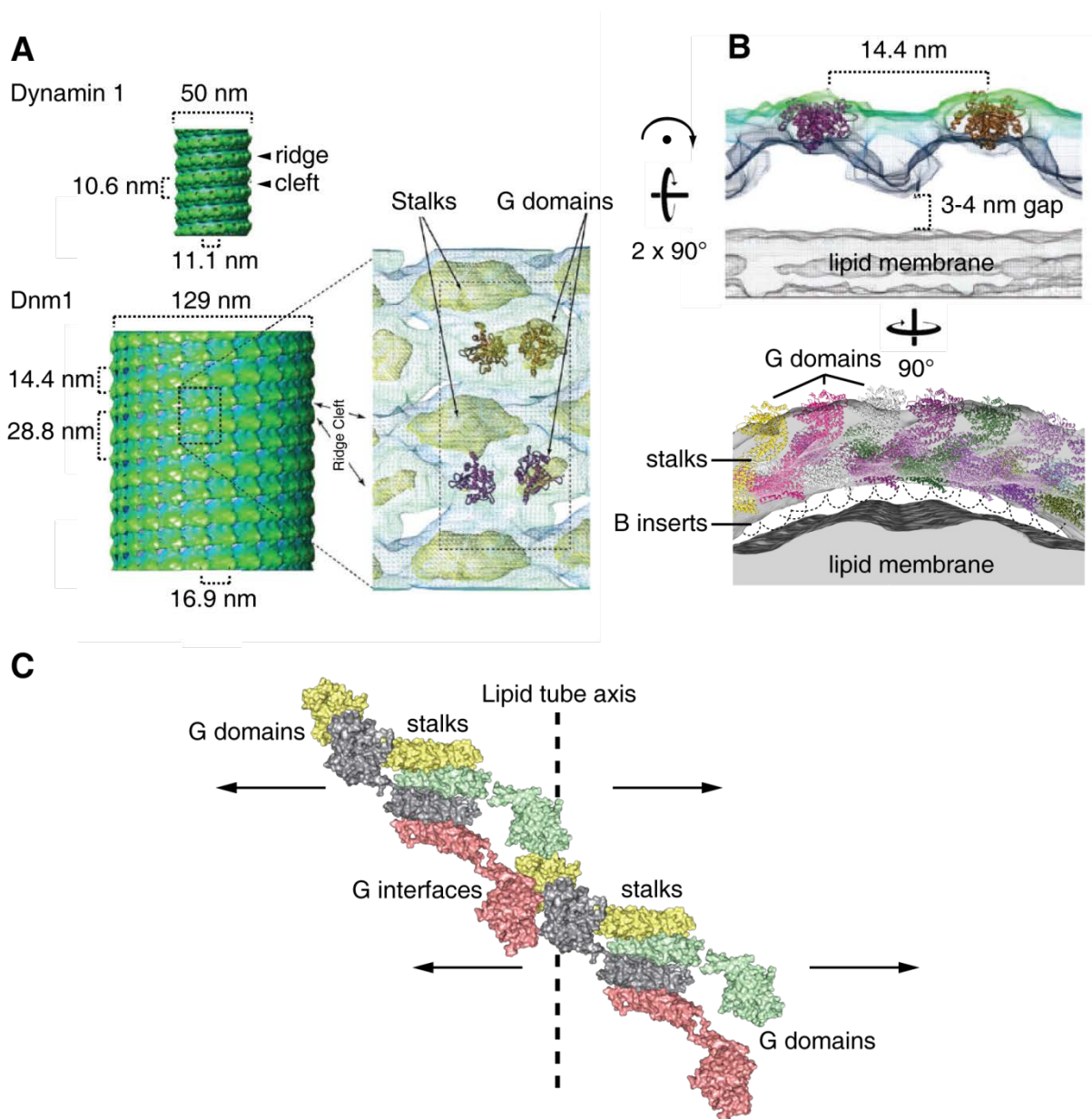
Figure 60: The DNM1L oligomer might be adapted to the size of mitochondria. **A:** Helical packing of human dynamin 1 ΔPRD compared to yeast Dnm1. The helical pitch is 28.8 nm for Dnm1 and 10.6 nm for dynamin. The axial spacing between the two starts of the Dnm1 helix is 14.4 nm. The outer diameters (129 nm and 50 nm, respectively), radial path lengths (16.9 nm and 11.1 nm, respectively), ridge and cleft features are indicated. G domains and stalks are depicted in the density. Four G domain crystal structures from dynamin 1 (PDB 1JX2) were manually fitted to one asymmetric subunit of the Dnm1 helical structure. Two dimers in separate helical starts of the asymmetric subunit are colored purple and orange, respectively. The dashed box highlights the region presented in B (upper panel). **B:** Fitting of the G domains as in A (upper panel) and fitting of the human DNM1L oligomer in the same electron density (lower panel). The gap between the lipid tube surface and the protein electron density would ideally correspond to the predicted position of the B insert. **C:** Space filling representation of 2 DNM1L tetramers aligned tangentially to the lipid tube axis. G domains of either tetramer interact across helical filaments to form a double filament around the lipid tube. This double filament might be an adaption to the larger size of mitochondria compared to the neck of a vesicle during endocytosis. Furthermore, mitochondria are double membrane enclosed cell organelles and the mechanical energy needed for scission is likely to be much higher than for budding off vesicles from the cell membrane. Figures A and B (upper panel) modified from [118]

than for the scission of clathrin-coated vesicles. A double stalk filament might enhance the mechanical force applied to the mitochondrial membrane in several orders of magnitude compared to the dynamin helical filaments in CCE. Also, mitochondria are double-membrane enclosed cell organelles, and at present no protein has been identified responsible for mim scission besides DNM1L. Hence, development of a more powerful protein scaffold to cleave the two membrane system of mitochondria seems to be evolutionary favorable.

Mutations in interface 4 do not affect DNM1L recruitment to liposomes *in vitro* (Figure 45) but these mutations fail to induce tubulation of these liposomes (Figure 47), suggesting that assembly via interface 4 is required for the formation of a stable membrane-anchored scaffold with membrane remodeling activity. The data presented here indicate that despite their related domain architecture, dynamin superfamily proteins can follow alternative oligomerization strategies. Thus, depending on the cellular context and the specific requirements of the cell, different assembly modes have evolved.

4.4. The molecular basis for DNM1L caused diseases

The stalk of DNM1L constitutes the central assembly domain (see 3.2.3) and mutations in the stalk interfaces were shown to interfere with higher order oligomerization and / or membrane remodeling, both *in vitro* and *in vivo* (see 3.3.1. and 3.3.3). Also mutations in L2^s (predicted interface 3) and the B insert (the proposed mom binding mediator) were shown to impair with DNM1L function (see 3.3.2). Regarding the structural information of DNM1L gained in this study, diseases caused by mutated DNM1L can be now explained on a molecular level (Figure 61).

A dramatic example of dysfunctional DNM1L was described recently where a newborn girl with a mutation in Ala395 died at the age of 37 days [26]. The reported A395D mutation is in direct vicinity to loop L2^s (i.e. interface 3). Mutations in this loop where shown to change the equilibrium between different oligomeric states in solution to a discrete dimeric species (Figure 44). Furthermore, *in vitro* and *in vivo* data presented here, clearly show that loop L2^S is indispensable for proper function of DNM1L (see 3.3.2). Given these facts and considering the close proximity of A395 to L2^s, it is plausible that the A395D mutation might disrupt the predicted interface 3
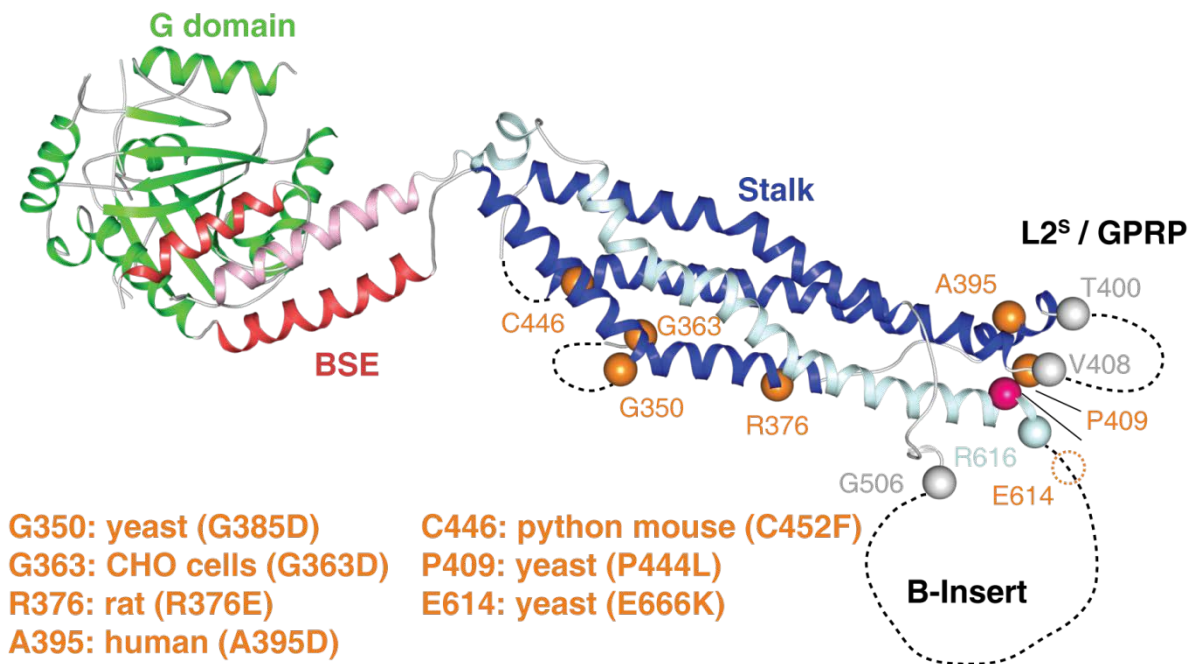
Figure 61: DNM1L in disease. Ribbon-type representation of the DNM1L monomer showing the positions of the B insert and the GPRP motif and non-functional or disease-related mutations (yellow). The first and last visible residues of the B insert and L2^S are indicated. The proposed S-nitrosylation site implicated in Alzheimer's disease is indicated as a pink sphere.

thereby inhibiting or at least diminishing the ability of DNM1L to divide mitochondria. It is well known that cells of newborn proliferate at much higher rates compared to adults. Many organ systems including brain, nervous system, digestive system, and cardiovascular system are still developing. It is obvious that functional mitochondrial dynamics during this phase are especially important and their disturbance can lead to severe defects including ultimately death.

Another mutation in DNM1L leading to severe defects was reported in mice [167]. A homozygote allele carrying a C452F mutation leads to death of the mouse embryo midway through gestation. Heterozygote mutation was reported to cause dilated cardiomyopathy, reduced levels of mitochondria enzyme complexes in heart, and cardiac ATP depletion. The corresponding phenotype was termed Python mouse because of the enlarged body size of the mice (Figure 62). Cys452 in mice corresponds to Cys446 in humans which is located in $\alpha2^S$ in the stalk pointing into the hydrophobic inside of this region of the stalk (Figure 63). The CF mutation could lead to hydrophobic stacking of the aromatic ring systems of Phe446 and Phe340 and/or

_____
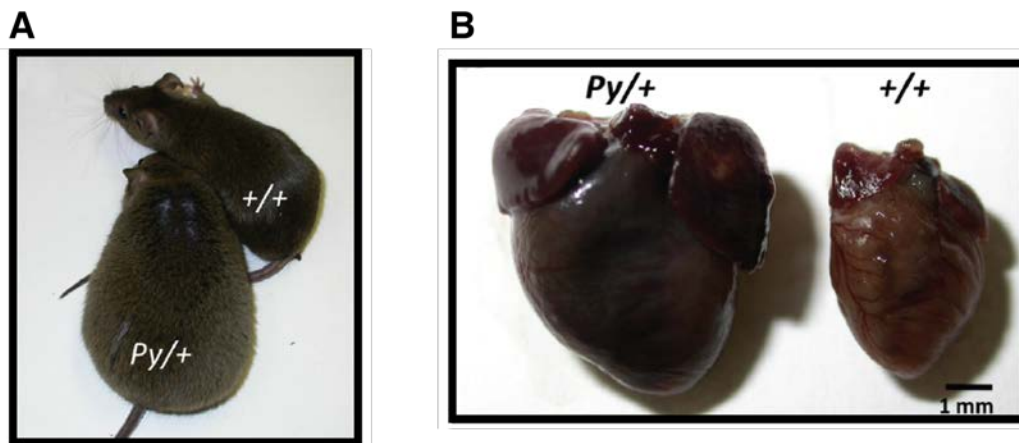
Figure 62: The Python mouse. **A:** 13-week-old Python mouse (Py/+) carrying the C452F mutation in α1N^S of DNM1L compared to a wild-type littermate control (+/+). **B:** Photo of the excised hearts from the same mice shown in A. Note the grossly enlarged ventricles and atria. Figure taken from [167].

Tyr344 in α1N^S, since these residues are located in close proximity to each other (Figure 63). Hydrophobic stacking, in turn, might agglutinate α1N^S and α2^S, thereby inhibiting conformational changes which might be necessary in the corresponding stalk region upon GTP hydrolysis. This might disturb the proposed fine-tuned domain interactions of DNM1L during mitochondrial remodeling (see 3.4). Accordingly, mitochondria in Python mice fibroblast cells appeared to be enlarged and more connected when compared to wild type mice, leading to the reported phenotype.
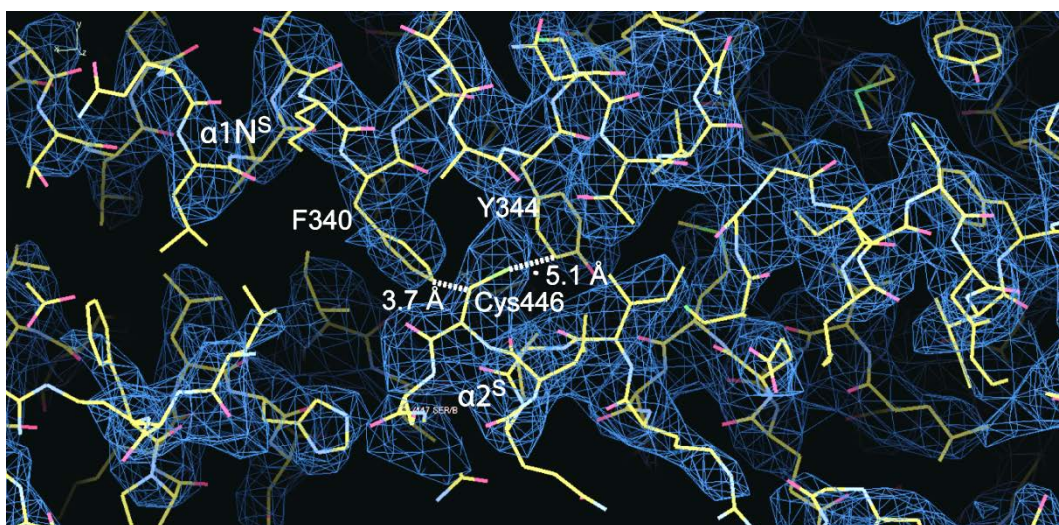
Figure 63: Position of the Python mouse mutation in DNM1L. Final 2F$_0$ - F$_c$ map from the DNM1L 4A ΔB crystal showing electron density and modeled residues of stalk helices α1N^S and α2^S. Distances between F340 and Cys446 and between Cys446 and Y344 are indicated (dotted lines). As can be seen, a CF mutation would most likely lead to the hydrophobic stacking of residues Y344, F446, and F340. The 2F$_0$ - F$_c$ map is shown in blue mesh at contour level of 1.2σ.

Interestingly, another mutation in the stalk helix 1 was reported in rat. The R376E mutation in α1M^S was reported to inhibit mitochondrial targeting of DNM1L via its adaptor Mff [153]. However, since Arg376 is in close proximity to interface 4 (Figure 61), its mutation to the opposite charged residue Glu376 might disturb electrostatic equilibrium in this region leading to collapse of interface 4. This, in turn, might inhibit proper oligomerization on the mitochondrial membrane which might be the reason for decreased localization of DNM1L to mitochondria as reported in the study.

Two other mutations in stalk helix 1 around L1N^S were reported for yeast (G350D) [164] and for a specific CHO cell line (R363D; CHO-ZP121) (Figure 61) [168]. L1N^S was already shown to be important for oligomerization in yeast [117, 151], MxA [50] and dynamin [152] and it is not surprising that mutations in and around this loop lead to assembly defects as most stalk mutations reported do (see above).

Finally, there are two mutations reported in yeast located near interface 3 (P409L) and at the C-terminal and of the B insert (E614K), respectively (Figure 61) [164], interfering with mitochondrial targeting leading to significantly enlarged mitochondria. The B insert was shown to be crucial for both, membrane remodeling *in vitro* and *in vivo* (see 3.3.2). The data of this study appear to indicate that the B insert contains the lipid binding domain. Therefore mutations in that region are likely to disturb mitochondrial targeting of DNM1L.

Taken together, the results of present study fundamentally contribute to our understanding of the molecular principles of dysfunctional DNM1L and the corresponding mitochondria-related diseases. Interestingly, all of the DNM1L mutations related to diseases or partial loss of function are reported to be located in the stalk or B insert and none is located in the G domain. The reason for that remains elusive.

4.5. Open questions and outlook

The structure of dynamin 1-like protein (DNM1L) presented here confirms common principles with respect to domain design and arrangement in dynamin superfamily proteins. Members of this family are molecular machines converting chemical energy stored in phosphoanhydride bonds of GTP (or ATP in the case of EHD) into mechanical energy. DNM1L transduces this mechanical energy to the mitochondrial membrane ultimately leading to scission of the organelle.

DNM1L is composed of a N-terminal G domain, a BSE, and a stalk. Higher order assembly necessary for its function was shown to be mediated in a similar way like for dynamin or MxA via conserved interfaces within the stalk. Affinity towards GTP and GDP is in the lower micromolar range as it was reported for dynamin and MxA, too. Furthermore, assembly was shown to be lipid-template dependent. Thus, a similar model for oligomerization at the underlying lipid template was assumed for DNM1L. In contrast to dynamin and MxA, however, DNM1L exhibits a novel stalk interface (interface 4), which is also involved in oligomerization. In the model suggested here, DNM1L filaments contain four stalks aligned in parallel (compared to two stalks in dynamin 1 and MxA), making the filament more stable in a mechanical sense. However, in such a filament G domains would have to dimerize across one single stalk filament to trigger GTP hydrolysis. Since a higher resolution EM reconstruction of human DNM1L oligomerized at its lipid template is not available at present, it remains speculative if such a large inter-domain interaction is possible. Furthermore, it is not clear how such an oligomer constricts to reduce its diameter (i.e. circumference) for mitochondrial scission. Another open question is how the DNM1L oligomer interacts with its known membrane receptors at the mom. Is the interaction between DNM1L and its receptors GTP dependent and if so what happens when GTP is hydrolyzed? Why is there more than one receptor for DNM1L and how many receptors interact at the same time with the DNM1L oligomer at the mom? Are interactions between DNM1L and its receptors triggered by post-translational modifications (PTMs)? *In vitro* data show that membrane remodeling activity of DNM1L is PTM-independent. Is the torque of the DNM1L double stalk filament higher compared to the torque of dynamin 1?

To answer all these questions, more structural and biochemical data are needed. A nucleotide-bound structure of DNM1L would shed more light into the structural

rearrangements of the oligomers induced by GTP-hydrolysis. This would allow for a less speculative model of DNM1L induced membrane remodeling. Also, a structure of DNM1L bound to its receptors would be very helpful to understand the receptor interplay at the mom. The results presented here are a first step for elucidating the molecular principles of mitochondrial division and to understand DNM1L caused mitochondrial disease.

_____

Appendix A - Instruments

Instrument	Manufacturer
24-well crystallization plates	Hampton Research, Aliso Viejo, USA
35 mm glass bottom dishes	MatTek, Ashland, USA
45 Ti rotor	Beckman Coulter, Krefeld, D
96 well 107rilliant107ation plates	Sigma-Aldrich, Steinheim, D
Agarose Gel Electrophoresis System	OLS, Bremen, D
Amicon centrifugal filter device	Millipore, Billerica, USA
An 50-Ti rotor	Beckman Coulter, Krefeld, D
Automated imaging and storing system Rock Imager	Formulatrix, Waltham, USA
Benchtop Centrifuge 5415 R	Eppendorf, Hamburg, D
Benchtop Centrifuge 5804 R	Eppendorf, Hamburg, D
Block Heater Rotilabo H250	Roth, Karlsruhe, D
Cell culture incubator CB150	Binder, Tuttlingen, D
Cell culture microscope Leica DM IL	Leica, Wetzlar, D
Centrifuge Avanti J-26 XP	Beckman Coulter, Krefeld, D
Chromatography column HisTrap HP 1 ml	GE Healthcare, Piscataway, USA
Chromatography columns Superdex 200 16/60, 26/60	GE Healthcare, Piscataway, USA
Chromatography columns Superdex 75 16/60, 26/60	GE Healthcare, Piscataway, USA
Chromatography columns XK 16/20, XK 26/20	GE Healthcare, Piscataway, USA
Cryo-Fridge VIP Series -86°C	Sanyo, Moriguchi, J
CryoLoops, various sizes	Hampton Research, Aliso Viejo, USA
Double-sector flow-through centerpiece AUC cell	Beckman Coulter, Krefeld, D
FCF150-Cu-50 carbon-Coated copper grids	Electron microscopy science, Hatfield, USA
Fluidizer M-110 L Pneumatic	Microfluidics, Newtown, USA
FPLC Äkta Prime Plus / Purifier	GE Healthcare, Piscataway, USA
Fridge N3956 4°C/-20°C	Liebherr, Biberach an der Riss, D
HPLC system 1260 Infinity LC	Agilent Technologies, Santa Clara, USA
Imaging system LAS4000 mini	FujiFilm, Düsseldorf, D
Isothermal Titration Calorimeter VP-ITC (MicroCal)	GE Healthcare, Piscataway, USA
JLA 8.100 rotor	Beckman Coulter, Krefeld, D
Laminar flow cabinet Herasafe HS12	Thermo Scientific, Dreieich, D
Microscope FluoView FV1000	Olympus, Hamburg, D
NanoDrop 2000	Thermo Scientific, Wilmington, USA
Nucleosil 100 C18 HPLC precolumn	Knauer, Berlin, D
Optima MAX-XP benchtop ultracentrifuge	Beckman Coulter, Krefeld, D
PCR thermocycler T-Gradient thermoblock	Biometra, Göttingen, D
Peristaltic pump ISM 827 B	Ismatec, Wertheim, D
pH-Meter	Mettler-Toledo, Gießen, D
Pipettes Eppendorf Research vario	Eppendorf, Hamburg, D
Pipetting robot Hydra-plus-One	Thermo Scientific, Dreieich, D
Precision scales	Mettler-Toledo, Gießen, D
RALS 270 dual detector	Malvern Instruments, Worcestershire, U.K.
Refractive index detector VE 3580	Malvern Instruments, Worcestershire, U.K.
Reversed-phase ODS-2 hypersil HPLC column	Thermo Scientific, Dreieich, D
SDS PAGE System Xcell Sure Lock	Life Techologies, Karlsruhe, D
Shaker Incubator Innova 44 R	New Brunswick Scientific, Enfield, USA
Soundsystem Inspire T3030	Creative Labs, Dublin, IRL
Thermoblock MKR13	HLC Biotech, Bovenden, D
TLA 100 rotor S.N. 899	Beckman Coulter, Krefeld, D
Ultracentrifuge Optima L-100 K	Beckman Coulter, Krefeld, D
Vacuum pump	Vacuubrand, Wertheim, D
Vortex Genie 2	Bender+Hobien, Zurich, CH
Water quench Julabo TW20	Julabo, Seelbach, D
Western Blot Module Xcell II	Life Techologies, Karlsruhe, D
XLI analytical ultracentrifuge	Beckman Coulter, Krefeld, D

Appendix B - Chemicals

Chemical / Enzyme / Kit	Cat.-No.	Manufacturer
10 x cloned Pfu reaction buffer	600153-82	Stratagene, La Jolla, USA
2-Log DNA ladder	N3200S	NEB, Frankfurt a. M., D
Acetic Acid	3783.5	Roth, Karlsruhe, D
Acetone	9372.2	Roth, Karlsruhe, D
Acetonitrile	CN20.2	Roth, Karlsruhe, D
Additive Screen	HR2-428	Hampton Research, Aliso Viejo, USA
Agarose	2267.3	Roth, Karlsruhe, D
Ammonium acetate	09689	Sigma-Aldrich, Steinheim, D
Ammonium chloride	09700	Sigma-Aldrich, Steinheim, D
Ammonium citrate dibasic	09833	Sigma-Aldrich, Steinheim, D
Ammonium fluoride	09737	Sigma-Aldrich, Steinheim, D
Ammonium formate	09735	Sigma-Aldrich, Steinheim, D
Ammonium iodide	09874	Sigma-Aldrich, Steinheim, D
Ammonium nitrate	09889	Sigma-Aldrich, Steinheim, D
Ammonium phosphate monobasic	9709	Sigma-Aldrich, Steinheim, D
Ammonium sulfate	9212.2	Roth, Karlsruhe, D
Autoinduction medium	71491-5	Novagen, Darmstadt, D
BamHI	R0136S	NEB, Frankfurt a. M., D
Boric acid	5935.2	Roth, Karlsruhe, D
Calcium acetate Hydrate	21056	Sigma-Aldrich, Steinheim, D
Calcium chloride	A119.1	Roth, Karlsruhe, D
Chloramphenicol	3886.3	Roth, Karlsruhe, D
Coomassie 108rilliant blue R 250 (C.I. 42660)	3862.2	Roth, Karlsruhe, D
di-Ammonium hydrogen phosphate	09839	Sigma-Aldrich, Steinheim, D
di-Potassium hydrogen phosphate anhydrous	P749.2	Roth, Karlsruhe, D
di-Sodium hydrogen phosphate anhydrous	P030.2	Roth, Karlsruhe, D
DMEM	E15-877	PAA, Pasching, A
DNAse I	04 716 728 001	Roche, Mannheim, D
*Dpn*I	R0176S	NEB, Frankfurt a. M., D
DTT	6908.2	Roth, Karlsruhe, D
EcoRI	R0101S	NEB, Frankfurt a. M., D
EDTA	8040.2	Roth, Karlsruhe, D
Ethanol	5054.2	Roth, Karlsruhe, D
Ethidium bromide	2218.1	Roth, Karlsruhe, D
Fetal bovine serum	A11-211	PAA laboratories, Pasching, A
GDP	NU-1172S	Jena Bioscience, Jena, D
GeneAmp© dNTPs	N8080007	Roche Molecular, Branchburg, USA
Glutathione Sepharose™ 4B	27-4574-01	Amersham, Piscatawy, USA
Glycerol	3783.1	Roth, Karlsruhe, D
GSH reduced	3541	Calbiochem, Darmstadt, D
GTP	NU-1012-1G	Jena Bioscience, Jena, D
Guanidinehydrochloride	0037.1	Roth, Karlsruhe, D
HEPES	9105.4	Roth, Karlsruhe, D
*Hind*III	R0104S	NEB, Frankfurt a. M., D
Imidazole	3899.3	Roth, Karlsruhe, D
Isopropanol	9866.5	Roth, Karlsruhe, D
Kanamycinsulfate	T823.4	Roth, Karlsruhe, D
Lithium acetate Dihydrate	62393	Sigma-Aldrich, Steinheim, D
Lithium citrate tribasic Tetrahydrate	62484	Sigma-Aldrich, Steinheim, D
Lithium nitrate	62574	Sigma-Aldrich, Steinheim, D
Magnesium acetate Tetrahydrate	63049	Sigma-Aldrich, Steinheim, D
Magnesium chloride Hexahydrate	63065	Sigma-Aldrich, Steinheim, D
Magnesium formate Dihydrate	00793	Sigma-Aldrich, Steinheim, D
Magnesium nitrate	237175-100G	Sigma-Aldrich, Steinheim, D
Magnesium sulfate Heptahydrate	63138	Sigma-Aldrich, Steinheim, D
Malonic acid	63290	Sigma-Aldrich, Steinheim, D
Mark12™ unstained standard	LC5677	Life Techologies, Karlsruhe, D

Methanol	4627.5	Roth, Karlsruhe, D
MPD	68340	Sigma-Aldrich, Steinheim, D
Ni Sepharose HP	71-5027-67 AD	GE Healthcare, München, D
NuPAGE© LDS Sample Buffer (4x)	NP0007	Life Techologies, Karlsruhe, D
NuPAGE© MES SDS Buffer Kit	NP0060	Life Techologies, Karlsruhe, D
NuPAGE© MOPS SDS Buffer Kit	NP0050	Life Techologies, Karlsruhe, D
NuPAGE© Novex 4-12% Bis-Tris Gel 1,5 mm, 10 / 15 well	NP0335BOX / NP0336BOX	Life Techologies, Karlsruhe, D
PBS	H15-002	PAA, Pasching, A
Pefabloc© SC-Protease inhibitor	A154.2	Roth, Karlsruhe, D
PEG 1000	81188	Sigma-Aldrich, Steinheim, D
PEG 2000MME	81321	Sigma-Aldrich, Steinheim, D
PEG 3350	88276	Sigma-Aldrich, Steinheim, D
PEG 400	91893	Sigma-Aldrich, Steinheim, D
PEG 4000	95904	Sigma-Aldrich, Steinheim, D
PEG 500MME	71578	Sigma-Aldrich, Steinheim, D
PEG 8000	89510	Sigma-Aldrich, Steinheim, D
Penicillin-Streptomycin, liquid, 100x	15140-122	Life Techologies, Karlsruhe, D
Pfu DNA polymerase	600153	Stratagene, La Jolla, USA
pGEX-6-P1	27-4597-01	GE Healthcare, München, D
Potassium acetate	60035	Sigma-Aldrich, Steinheim, D
Potassium chloride	6781.3	Roth, Karlsruhe, D
Potassium citrate tribasic monohydrate	25107	Sigma-Aldrich, Steinheim, D
Potassium dihydrogen phosphate	3904.1	Roth, Karlsruhe, D
Potassium fluoride	60239	Sigma-Aldrich, Steinheim, D
Potassium formate	60246	Sigma-Aldrich, Steinheim, D
Potassium iodide	60400	Sigma-Aldrich, Steinheim, D
Potassium nitrate	60414	Sigma-Aldrich, Steinheim, D
Potassium phosphate	3904.3	Roth, Karlsruhe, D
Potassium sulfate	60528	Sigma-Aldrich, Steinheim, D
Potassium thiocyanate	60517	Sigma-Aldrich, Steinheim, D
PreScission™ Protease	27-0843-01	GE Healthcare, München, D
QIAprep™ Spin Miniprep Kit	27106	Qiagen, Hilden, D
QIAquick gel extraction kit	28704	Qiagen, Hilden, D
Roti©Fect transfection kit	P001.3	Roth, Karlsruhe, D
Sodium acetate Trihydrate	71188	Sigma-Aldrich, Steinheim, D
Sodium chloride	9265.2	Roth, Karlsruhe, D
Sodium citrate tribasic Dihydrate	71402	Sigma-Aldrich, Steinheim, D
Sodium di-hydrogen phosphate 2-hydrate	T879.1	Roth, Karlsruhe, D
Sodium fluoride	71519	Sigma-Aldrich, Steinheim, D
Sodium hydroxide	6771.1	Roth, Karlsruhe, D
Sodium nitrate	71755	Sigma-Aldrich, Steinheim, D
Sodium sulfate Decahydrate	71969	Sigma-Aldrich, Steinheim, D
Sodium tartrate dibasic dihydrate	71994	Sigma-Aldrich, Steinheim, D
Sodium thiocyanate	71938	Sigma-Aldrich, Steinheim, D
T4 DNA ligase	M0202S	NEB, Frankfurt a. M., D
Terrific-Broth medium	HP61.1	Roth, Karlsruhe, D
Tetrabutylammonium bromide	86860-500G	Sigma-Aldrich, Steinheim, D
The Classics II Suite	130723	Qiagen, Hilden, D
The Classics Suite	130701	Qiagen, Hilden, D
The JSCG+ Suite	130720	Qiagen, Hilden, D
The MPD Sutie	130706	Qiagen, Hilden, D
The pHClear II Suite	130710	Qiagen, Hilden, D
Trichloromethane	6340.2	Roth, Karlsruhe, D
Tryptone/peptone	8952.2	Roth, Karlsruhe, D
Uranyl acetate dihydrate	73943	Sigma-Aldrich, Steinheim, D
Western Blotting Detection Reagent Amersham ECL Prime	RPN2232	GE Healthcare, München, D
XhoI	R0146L	NEB, Frankfurt a. M., D
Yeast extract	2363.2	Roth, Karlsruhe, D
Zinc acetate Dihydrate	96459	Sigma-Aldrich, Steinheim, D

Appendix C - Clone list

Protein	Construct	Residues (Start-End)	Plasmid Resistance	FW primer ID (RS)	REV primer ID (RS)
hsDNM1L i2	full length	1-710	pSKB2LNB, KAN	B491, BamHI	B492, EcoRI
hsDNM1L i2	Δ 514-613	1-710 Δ514-613	pSKB2LNB, KAN	B632	B633
hsDNM1L i2	GPRP401-404AAAA	1-710	pSKB2LNB, KAN	B819	B820
hsDNM1L i2	Δ 514-613 GPRP401-404AAAA	1-710 Δ514-613	pSKB2LNB, KAN	B819	B820
hsDNM1L i2	R430D	1-710	pSKB2LNB, KAN	C078	C079
hsDNM1L i2	E426A	1-710	pSKB2LNB, KAN	C082	C083
hsDNM1L i2	N635A	1-710	pSKB2LNB, KAN	C225	C226
hsDNM1L i2	D638A	1-710	pSKB2LNB, KAN	C227	C228
hsDNM1L i2	K642E	1-710	pSKB2LNB, KAN	C229	C230
hsDNM1L i2	M482D	1-710	pSKB2LNB, KAN	C231	C232
hsDNM1L i2	E490A	1-710	pSKB2LNB, KAN	C686	C687
hsDNM1L i2	E490R	1-710	pSKB2LNB, KAN	C688	C689
hsDNM1L i2	full length	1-710	pmEGFP-C1 NEO/KAN	C098 (EcoRI)	C099 (BamHI)
hsDNM1L i2	PAL 404-406 sm	1-710	pmEGFP-C1 NEO/KAN	C100	C101
hsDNM1L i2	PALFVP 404-409 sm	1-710	pmEGFP-C1 NEO/KAN	C102	C103
hsDNM1L i2	PALFVPEV 404-411 sm	1-710	pmEGFP-C1 NEO/KAN	C104	C105
hsDNM1L i2	PALFVPEV 404-411 sm K642E	1-710	pmEGFP-C1 NEO/KAN	C229	C230
hsDNM1L i2	PALFVPEV 404-411 sm R430D	1-710	pmEGFP-C1 NEO/KAN	C078	C079
hsDNM1L i2	PALFVPEV 404-411 sm E426A	1-710	pmEGFP-C1 NEO/KAN	C082	C083
hsDNM1L i2	PALFVPEV 404-411 sm GPRP401-404AAAA	1-710	pmEGFP-C1 NEO/KAN	C260	C261
hsDNM1L i2	PALFVPEV 404-411 sm Δ 514-613	1-710 Δ514-613	pmEGFP-C1 NEO/KANN	B632	B633

sm = silent mutation(s), RS = restriction site,

Appendix D - Alignment

```
hsDNM1L-i2   ---------- ---------- ---------- ---------- ---------- ---------- ---------- ---------- ---------- ----------   1
hsDNM1L-i1   ---------- ---------- ---------- ---------- ---------- ---------- ---------- ---------- ---------- ----------   1
hsDNM1L-i3   ---------- ---------- ---------- ---------- ---------- ---------- ---------- ---------- ---------- ----------   1
scDNM1L      ---------- ---------- ---------- ---------- ---------- ---------- ---------- ---------- ---------- -------MAS   3
hsDynamin1   ---------- ---------- ---------- ---------- ---------- ---------- ---------- ---------- ---------- -------MGN   3
hsDynamin2   ---------- ---------- ---------- ---------- ---------- ---------- ---------- ---------- ---------- -------MGN   3
hsDynamin3   ---------- ---------- ---------- ---------- ---------- ---------- ---------- ---------- ---------- -------MGN   3
hsMxA        ---------- ---------- ---------- ---------- ---------- -----MVVSE VDIAKADPAA ASHPLLLNGD ATVAQKNPGS          35
hsMxB        ----MSKAHK PWPYRRRSQF SSRKYLKKEM NSFQQQPPPF GTVPPQMMFP PNWQGAEKDA AFLAKDFNFL TLNNQPPPGN          76
hsOPA1       DLVKLAPDFD KIVESLSLLK DFFTSGSPEE TAFRATDRGS ESDKHFRKVS DKEKIDQLQE ELLHTQLKYQ RILERLEKEN         240
```

BSE L1^BG G domain P loop switch I α^1B β^1G α^1G

```
hsDNM1L-i2   ---------- ---------- MEALIPVINK LQDVFNTVG- --ADIIQLEQ IVVGTQSSG KSSVLESLVG RDLLPRGTG-   56
hsDNM1L-i1   ---------- ---------- MEALIPVINK LQDVFNTVG- --ADIIQLEQ IVVGTQSSG KSSVLESLVG RDLLPRGTG-   56
hsDNM1L-i3   ---------- ---------- MEALIPVINK LQDVFNTVG- --ADIIQLEQ IVVGTQSSG KSSVLESLVG RDLLPRGTG-   56
scDNM1L      ---------- ---------- LEDLIPTVNK LQDVVYDSG- --IDTFDLEI IAVVGSQSSG KSSIIETLVG RDFLPRGTG-   59
hsDynamin1   R--------- --------G MEDLIPLVNR LQDAFSAICG --NADLDLEQ IAVVGGQSAG KSSVLENFVG RDFLPRGSG-   62
hsDynamin2   R--------- --------G MEELIPLVNR LQDAFSSICQ --SCHLDIEQ IAVVGGQSAG KSSVLENFVG RDFLPRGSG-   62
hsDynamin3   R--------- --------E MEELIPLVNR LQDAFSALCQ --SCLFELEQ IAVVGGQSAG KSSVLENFVG RDFLPRGSG-   62
hsMxA        ---------- -VAENNLCSQ YEEKVRPCID IIDSLRALGV --EQDLALPA IAVIGDQSSG KSSVLEALSG -VALPRGSG-  100
hsMxB        RSQPRAMGPE NN----LYSQ YEQKVRPCID IIDSLRALGV --EQDLATEA IAVIGDQSSG KSSVLEALSG -VALPRGSGE  148
hsOPA1       KELRKLVLQK DDKGIHHRKL KKSLIDMYSE VLDVLSDYDA SYNTQDHLER VVVVGDQSAG KTSVLEMIAQ ARIFPRGSGE  320
```

β2^G β2A^G αE1^G

```
hsDNM1L-i2   IVTRRPLIIQ LVHVS----- ---------- ---------- -QEDKRKTTG EENGVEAEEW GKFLHTKNKL YTDFDEIRQE  110
hsDNM1L-i1   IVTRRPLIIQ LVHVS----- ---------- ---------- -QEDKRKTTG EENGVEAEEW GKFLHTKNKL YTDFDEIRQE  110
hsDNM1L-i3   IVTRRPLIIQ LVHVS----- ---------- ---------- -QEDKRKTTG EENGVEAEEW GKFLHTKNKL YTDFDEIRQE  110
scDNM1L      IVTRRPLVLQ LNNISPNSPL IEEDDNSVNP HDEVTKISGF EAGTKPLEYR GKERNHADEW GEFLHIPGKR YYDFDDIKRE  139
hsDynamin1   IVTRRPLVLQ LVNAT----- ---------- ---------- ---------- -------TEY AEFLHCKGKK FTDFEEVRLE  100
hsDynamin2   IVTRRPLIIQ LIFSK----- ---------- ---------- ---------- -------TEH AEFLHCKSKK FTDFDEVRQE  100
hsDynamin3   IVTRRPLVLQ LVTSK----- ---------- ---------- ---------- -------AEY AEFLHCKGKK FTDFEEVRLE  100
hsMxA        IVTRCPLVLK LKKLVNEDK- ---------- ---------- ---------- -------WRG KVSMQDYEIE ISDASEVEKE  142
hsMxB        IVTRCPLVPK LKKQPCEA-- ---------- ---------- ---------- -------WAG RISYFNTELE LQLPGQVEKE  189
hsOPA1       MMTRSPVKVT LSEGPHHVA- ---------- ---------- ---------- -------LFK DSSREFDLTK EEDIAALRHE  362
```

cis stabilizing loop   switch II   αE1^G β2B^G β3^G α2^G β4^G

```
hsDNM1L-i2   IENETERISG NNKGVSP-EP IHLKIFSPNV VNLTLVDLPG MTKVPVGDQP KDIEIQIREL ILRFISNPNS IIIAVTAANT  189
hsDNM1L-i1   IENETERISG NNKGVSP-EP IHLKIFSPNV VNLTLVDLPG MTKVPVGDQP KDIEIQIREL ILRFISNPNS IIIAVTAANT  189
hsDNM1L-i3   IENETERISG NNKGVSP-EP IHLKIFSPNV VNLTLVDLPG MTKVPVGDQP KDIEIQIREL ILRFISNPNS IIIAVTAANT  189
scDNM1L      IENETARIAG KDKGISK-IP INLKVFSPHV LNITLVDLPG ITKVPIGEQP PDIEKQIKNL ILDYIATPNC LIIAVSPANV  218
hsDynamin1   IEAETDRVTG TNKGISP-VP INLRVYSPHV LNLTLVDLPG MTKVPVGDQP PDIEFQIRDM LMQFVTKENC LIIAVSPANS  179
hsDynamin2   IEAETDRVTG TNKGISP-VP INRVYSPHV LNLTLVDLPG MTKVPVGDQP PDIEYQIRDM ILQFISRESS LIIAVTPANM  179
hsDynamin3   IEAETDRVTG MNKGISS-IP INPRVYSPHV LNLTLIDLPG ITKVPVGDQP PDIEYQIREM LMQFITRENC LIIAVTPANT  179
hsMxA        INKAQNAIAG EGMGISH-EL ITLEISSRDV PDITIILDLPG ITRVAVGNQP ADIGYKIKTL IKKYIQRQET ISIVVVPSNV  221
hsMxB        IHKAQNVYAG NGRGISH-EL ISLEITSPNV PDITIIDLPG ITRVAVDNQP RDIGIQIKAL IKKYIQRQQT INIVVVPCNV  268
hsOPA1       IELRMRKNVK EGCTVSP-ET ISLNVKGPGL QRMVLVDLPG VINTVTSGMA PDTKETIFSI SKAYMQNPNA IILCIQDGSV  441
```

trans stabilizing loop   G4 motif   G5 motif   α3^G β5^G α4^G β6^G αE2^G
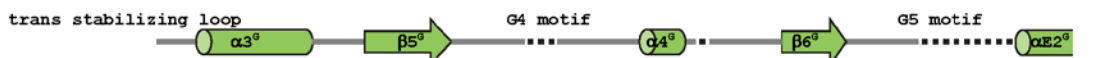
```
hsDNM1L-i2   DMATSEALKI SREVDPDGRR TLAVITKLDL MDAGTD---- AMDVLMGRVI PVK-LGIIGV VNRSQLDINN KKSVTDSIRD  264
hsDNM1L-i1   DMATSEALKI SREVDPDGRR TLAVITKLDL MDAGTD---- AMDVLMGRVI PVK-LGIIGV VNRSQLDINN KKSVTDSIRD  264
hsDNM1L-i3   DMATSEALKI SREVDPDGRR TLAVITKLDL MDAGTD---- AMDVLMGRVI PVK-LGIIGV VNRSQLDINN KKSVTDSIRD  264
scDNM1L      DLVNSESLKL AREVDPQGKR TIGVITKLDL MDSGTN---- ALDILSGKMY PLK-LGFVGV VNRSQQDIQL NKTVEESLDK  293
hsDynamin1   DLANSDALKV AKEVDPQGQR TIGVITKLDL MDEGTD---- ARDVLENKLL PLR-RGYIGV VNRSQKDIDG KKDITAALAA  254
hsDynamin2   DLANSDALKL AKEVDPQGLR TIGVITKLDL MDEGTD---- ARDVLENKLL PLR-RGYIGV VNRSQKDIEG KKDIRAALAA  254
hsDynamin3   DLANSDALKL AKEVDPQGLR TIGVITKLDL MDEGTD---- ARDVLENKLL PLR-RGYIGV VNRSQKDLDG KKDIKAAVLA  254
hsMxA        DIATTEALSM AQEVDPEGDR TIGILTKPDI VDKGTED--K VVDVVRNLVF HLK-KGYMIV KCRGQQEIQD QLSISEALQR  298
hsMxB        DIATTEALSM AHEVDPEGDR TIGIITKPDI MDRGTEK--S VMNVVRNLTY PLK-KGYMIV KCRGQQEITN RLSIAEATKK  345
hsOPA1       DAERSIVTDL VSQMDPHGRR TIFVLTKVDL AEKNVASPSR IQQIIEGKLF PMKALGYFAV VTGKG---NS SESIEAIREY  518
```

G domain   BSE   L1^BS   stalk   αE2^G αE2'^G α5^G α2^B α1N^S

```
hsDNM1L-i2   EYAFLQKK-- YPSLANRNGT ---KYLARTI NRLLMHHIRD CLPELKTRIN VLAAQYQSLI NSYG----EP VDDKSATLLQ  335
hsDNM1L-i1   EYAFLQKK-- YPSLANRNGT ---KYLARTI NRLLMHHIRD CLPELKTRIN VLAAQYQSLI NSYG----EP VDDKSATLLQ  335
hsDNM1L-i3   EYAFLQKK-- YPSLANRNGT ---KYLARTI NRLLMHHIRD CLPELKTRIN VLAAQYQSLI NSYG----EP VDDKSATLLQ  335
scDNM1L      EEDYFRKHPV YRTLSTCGT ---RYLAKLL NQTLLSHIRD KLPDIKTKIN TLISQTEQEL ARYGGVGATT NESRASLVLQ  370
hsDynamin1   ERKFFLSHPS YRHLADRMGT ---PYLQKVL NQQLTNHIRD TLPGLRNKLQ SQLLSLEKEV EEYKNFRPDD PARKTKALLQ  331
hsDynamin2   ERKFFLSHPA YRHLADRMGT ---PHLQKTL NQQLTNHIRD SLPALRSKLQ SQLLSLEKEV EEYKNFRPDD PTRKTKALLQ  331
hsDynamin3   ERKFFLSHPA YRHLADRMGT ---PHLQKVL NQQLTNHIRD TLPNLRNKLQ GQLLSIEHEV EAYKNFKPED PTRKTKALLQ  331
hsMxA        EKIFFENHPY YRDLLEEGKA TVPCLAEKLT TSELITHICK SLPLLENQLK ETHQRITEEL QKYGVDIPED ENEKMFFLLD  377
hsMxB        EITTFQTHPY YRVLLEEGSA TVPRLAERLT TTELIMHIQK SLPLIEGQIR ESHQKATEEL QKYGVDIPED EADKMFFLIE  424
hsOPA1       REEFFQNSKL IKTSMLKAHQ VTTRNLSLAV SDCFWKMVRE SVEQQADSFK ATRFNLETEW KNNYP--RLR ELDRNELFEK  596
```

111

Block 1 — L1N^s L1C^s L2^s / α1N^s α1M^s α1C^s α2^s / ••••GPRP401-404AAAA

```
hsDNM1L-i2   LITKEATEYC NTIEGTAKYI ETSEICGGAR ICYIFHETEG RTIESVDPLG GLNTIDILTA IRNATCPRPA LEVPEVSFEL  415
hsDNM1L-i1   LITKEATEYC NTIEGTAKYI ETSEICGGAR ICYIFHETEG RTIESVDPLG GLNTIDILTA IRNATCPRPA LEVPEVSFEL  415
hsDNM1L-i3   LITKEATEYC NTIEGTAKYI ETSEICGGAR ICYIFHETEG RTIESVDPLG GLNTIDILTA IRNATCPRPA LEVPEVSFEL  415
scDNM1L      LMNKESTNEI SSIDCTSSDI NTKEICGGAR IYYIMNNVEG NSIKSIDPTS NLSVLDVRTA IRNSTGPRPT LEVPEIAFEL  450
hsDynamin1   MVQQEAVDFE KRIECSGDQI DTYEISGGAR INRIFHERFP FEIVKMEFDE KELRRETSYA IKNIHCIRTG LFTPDMAFET  411
hsDynamin2   MVQQEGVDFE KRIECSGDQV DTLEISGGAR INRIFHERFP FEIVKMEFDE KDLRRETSYA IKNIHGVRTG LFTPDIAFEA  411
hsDynamin3   MVQQEAVDFE KRIECSGDQV DTLEISGGAR INRIFHERFP FEIVKMEFNE KELRREISYA IKNIHGIRTG LFTPDMAFEA  411
hsMxA        KINAENQDIT ALVQCE-ETV GEEDIRLFTR LRHEFHKWST IIENNEQEGH KILSRKIQKF ENQYRGRELP GEVNYRTTEI  456
hsMxB        KIKMENQDIE KLVECE-EVV RENETRLYNK IREDFKNVVG ILATNTQKVK NIIHEEVEKY EKQYRGKELL GEVNYKTFEI  503
hsOPA1       AKNEIILDEVI SLSQVTPKHW EEILQQSLWE RVSTHVIENI YLPAAQTMNS GTFNTTVDIK LKQWTDKQLP NKAVEVAWET  676
```

•G385D(yeast) •G398S (yeast) •R376E (rat) •A395D (human) •P444L (yeast)
•G363D (hamster)

Block 2 — L3^s / α2^s α3^s / E426A• •R430A

```
hsDNM1L-i2   LVKRQIKRIE EPSLRCVELV HEEMQRIIQH CSNYSTQELL REPKLHDAIV EVVTCLIRKR LPVTNE---- -MVHNIVAIE  490
hsDNM1L-i1   LVKRQIKRIE EPSLRCVELV HEEMQRIIQH CSNYSTQELL REPKLHDAIV EVVTCLIRKR LPVTNE---- -MVHNIVAIE  490
hsDNM1L-i3   LVKRQIKRIE EPSLRCVELV HEEMQRIIQH CSNYSTQELL REPKLHDAIV EVVTCLIRKR LPVTNE---- -MVHNIVAIE  490
scDNM1L      LVKPQIKLIL EPSQRCVELV YEEIMKICHK CG---SAEIA RVPKLKSMLI EVISELIRER LQPTRS---- -YVESLIDIH  522
hsDynamin1   IVKKQVKKIR EPCLKCVDMV ISEIISTVRQ CT----KKIQ QYPRLREEME RIVTTHIRER EGRTKE---- -QVMLLIDIE  482
hsDynamin2   IVKKQVVKIK EPCLKCVDLV IQEIINTVRQ CT----SKIS SMPRIREETE RIVTTYIRER EGRTKD---- -QILLLIDIE  482
hsDynamin3   IVKKQIVKIK GPSLKSVDLV IQEIINTVKK CT----KKIA NEPRICEETE RIVANHIRER EGKTKD---- -QVLLLIDIQ  482
hsMxA        IVKQQIKAIE EPAVDMLHTV TDMVRLAETD S---IKNEE EFNLHRTAK SKIEDIRAEQ EREGEK---- -LIRLHEQIE  528
hsMxB        IVHQYLIQQIV EPAISMIQKA MEIIQQAFIN VA---KKHEG EFNFNQTVQ STIEDIKVKH TAKAEN---- -MIQLQERIE  575
hsOPA1       IQEEFSRFMT EPKGREHDDI FDKIKEAVKE ES----IKRH KANDEAEDSL RVIQHNALED RSISDKQQWD AAIYFMEEAL  752
```

•C452 (Python mouse)

Block 3 — stalk L4^s B-insert / [deletion (514-613)

```
hsDNM1L-i2   LAYINTKHPD EADACGIMNN NIEEQRRNRL ARELP----- ---------- --SAVSRDK- ---------- ----------  532
hsDNM1L-i1   LAYINTKHPD EADACGIMNN NIEEQRRNRL ARELP----- ---------- --SAVSRDK SKVPSALAPA SQEPSPAASA  553
hsDNM1L-i3   LAYINTKHPD EADACGIMNN NIEEQRRNRL ARELP----- ---------- --SAVSRDK- ---------- ----------  532
scDNM1L      RAYINTNHPN ELSATEAMDD -IMKTRRKRN QELLK----- ---------- --SKLSQQEN GQTNGING-T S---------  574
hsDynamin1   LAYMNTNHED EIGFANAQQR SNQMNKKKTS GNQDE----- -ILVIRKGWL TINNIGIMKG GSKEYWFVLT AENLSWYK--  554
hsDynamin2   QSYINTNHED EIGFANAQQR STQLNKKRAI PNQGE----- -ILVIRRGWL TINNISLMKG GSKEYWFVLT AESLSWYK--  554
hsDynamin3   VSYINTNHED EIGFANAQQR SSQVHKKTTV GNQGTNLPPS RQIVIRKGWL TISNIGIMKG GSKGYWFVLT AESLSWYK--  560
hsMxA        QIVY------ ---CQDQVYR GALQKVEEKE LEEE------ ---------- ---------- ---------- ----------  553
hsMxB        QMVE------ ---CQDQIYS VVLKKVREEI FNPLG----- ---------- ---------- ---------- ----------  601
hsOPA1       QARIKDTENA IENMVGPDWK KRWLYWMNRT QEQCVHN--- ---------- ---------- ---------- ----------  789
```

Block 4 — B-insert

```
hsDNM1L-i2   -----LIQDS RRETKNVASG GGGVGDGVQE PTTGNWRGML ---------- KTSKAEEIIA EEKSKP---- ---IPIMPAS  590
hsDNM1L-i1   EADGKLIQDS RRETKNVASG GGGVGDGVQE PTTGNWRGML ---------- KTSKAEEIIA EEKSKP---- ---IPIMPAS  616
hsDNM1L-i3   ---------- ------VASG GGGVGDGVQE PTTGNWRGML ---------- KTSKAEEIIA EEKSKP---- ---IPIMPAS  579
scDNM1L      -------SIS SNIDQDSAKN SDYDDDGIDA ESKQTKDKFL NY-----FFG KDKKGQPVFD ASDKKRSIAG DGNIEDERNL  642
hsDynamin1   -------DDE EKEKKYMLSV DNLKLRDVEK GFMSSKHIFA LFNTEQRNVY KDYRQLEIAC ETQEEVDS-- -WKASFIRAG  624
hsDynamin2   -------DEE EKEKKYMLPL DNLKIRDVEK GFMSNKHVFA LFNTEQRNVY KDLRQIEIAC DSQEDVDS-- -WKASFIRAG  624
hsDynamin3   -------DDE EKEKKYMLPL DNLKVRDVEK SFMSSKHIFA LFNTEQRNVY KDYRFLEIAC DSQEDVDS-- -WKASLIRAG  630
hsMxA        ---------- ---------- ---------- ---------- ---------- ---------- ---------- ----KKKKSW  559
hsMxB        ---------- ---------- ---------- ---------- ---------- ---------- ---------- ----TPSQNM  607
hsOPA1       --------ET KNELEKMLKC NEEHPAYLAS DEITTVRKN- ---------- LESRGVEVDP SLIKDTWHQV YRRHFIKTAL  850
```

Block 5 — B-insert stalk α4^s / deletion ■] ◆ •K642E

```
hsDNM1L-i2   PQKG------ -HAVNLLDVP VPVARKISAR EQRDCEVIER LIKSYFLIVR KNIQDSVPKA VMHFLVNHVK DTIQSELVGQ  663
hsDNM1L-i1   PQKG------ -HAVNLLDVP VPVARKISAR EQRDCEVIER LIKSYFLIVR KNIQDSVPKA VMHFLVNHVK DTIQSELVGQ  689
hsDNM1L-i3   PQKG------ -HAVNLLDVP VPVARKISAR EQRDCEVIER LIKSYFLIVR KNIQDSVPKA VMHFLVNHVK DTIQSELVGQ  652
scDNM1L      QISD------ -FSLGDIDDL ENAEPPITER EELECEIIKR IIVSYDIIR EMIEDQVPKA VMCLLVNYCK DSVQNRLVTK  715
hsDynamin1   VYPERVGDKE KASETEENGS DSFMHSVDPQ LERQVETIRN IVDSYMAIVN KTVRDLMPKT IMHLMINNTK EFIFSELIAN  704
hsDynamin2   VYPE------ KDQAENEDGA QENTFSVDPQ LERQVETIRN IVDSYVAIIN KCIRDLMPKT IMHLMINNTK AFIHHELLAY  698
hsDynamin3   VYPD------ KSVAENDENG QAENFSVDPQ LERQVETIRN IVDSYMIIN KCIRDLIPKT IMHLMINNVK DFINSELIAQ  704
hsMxA        DFG------- ----AFQSSSA TDSSVEEIFQ HLMAVHQEAS KRISSHIPLI IQFEMLQTYG QQIQKAMIQL  619
hsMxB        KLNS------ ---------- ---HFPSNES SVSSETEIGI HLNAYELETS KRIANQIPFI IQYEMIRENG DSIQKAMYQI  668
hsOPA1       NHCN------ ---LCRRGFY YYQRHFVDSE LECNDVVIFW RIQRMIATTA NTIRQQITNT EVRRIEKNVK EVIEDFAEDG  921
```

•E666K (yeast)

Block 6 — L2B^s / stalk α5^s BSE α3^s

```
hsDNM1L-i2   IYKSSLIDDI ITESEDMAQR RKEAADMIKA IQGASQIIAE IRETHLW--- ---------- ---------- ----------  710
hsDNM1L-i1   IYKSSLIDDI ITESEDMAQR RKEAADMIKA IQGASQIIAE IRETHLW--- ---------- ---------- ----------  736
hsDNM1L-i3   IYKSSLIDDI ITESEDMAQR RKEAADMIKA IQGASQIIAE IRETHLW--- ---------- ---------- ----------  699
scDNM1L      IYKETLIEEI IVEDQTLAQD RELCVKSIGV YKKAATLISN IL-------- ---------- ---------- ----------  757
hsDynamin1   IYSCGDQNTI MEESAEQAQR RDEMLRMYHA IKEALSIIGD INTTTVSTPM PPPVDDSWLQ VQS--VPAGR RSPTSSPTPQ  782
hsDynamin2   IYSSADQSSI MEESAEQAQR RDDMLRMYHA LKEALNIIGD ISTSTVSTPV PPPVDDTWLQ SASSHSPTPQ RRPVSSIHPP  778
hsDynamin3   IYSSEDQNTI MEESAEQAQR RDEMLRMYQA LKEALGIIGD ISTATVSTPM PPPVDDSWIQ HSR---RSPP PSPTTQRRPT  781
hsMxA        IQDKDTYSWI IKERSDTSDK RKFLKERIAR ITQRRRIAQ EPG------- ---------- ---------- ----------  662
hsMxB        IQEKNRYSWI IQEQSETAIK RRILKERIYR ITQRHAICQ ESSKEIH--- ---------- ---------- ----------  715
hsOPA1       EKKIKLITGKRVQ LAEDLKIV VREIQEKIDA EIEALHQEK- ---------- ---------- ---------- ----------  960
```

Amino acid sequences of the three human (*hs*) DNM1L isoforms (Swiss-Prot accession O00429-1,2,3), *Saccharomyces cerevisiae* (*sc*) Dnm1 (P54861), human dynamin1 (Q05193), dynamin2 (P50570), dynamin3 (Q9UQ16), human MxA (P20591) and MxB (P20592) and human OPA1 (O60313) were aligned using CLUSTAL W [123] and manually adjusted. Residues with a conservation of greater than 60% are color-coded (D,E in red; R,K,H in blue; N,Q,S,T in grey; L, I, V, F, Y, W, M, C in green, P,G in brown). Molecule A was used as a reference to determine the secondary structure. In undefined regions of molecule A, information from other molecules was considered. Alpha-helices are shown as cylinders with colors as in Figure 30. Superscript letters are used to assign the domain architecture (G - G domain, B - BSE, S - stalk). Known phosphorylation sites (■) [156, 158-160, 169], a nitrosylation site (♦) [24, 25] and SUMOylation sites (▲) [155] of the DNM1L isoform-1 are indicated. Other described disease relevant and oligomerization-deficient mutants of DNM1L are indicated beneath the sequence [26, 164, 167, 168, 170].

Appendix E - Abbreviation

AC	Affinity chromatography
AIM	Autoinduction medium
AMP-PNP	5'-adenylyl-β-γ-imidodiphosphate
ATP	adenosine-5'-triphosphate
B	B-insert
BamH	*Bacillus amyloliquefaciens H*
Bis-Tris	(Bis(2-hydroxyethyl)-amino-tris(hydroxymethyl)-methane)
CCV	clathrin coated vesicle
cDNA	complementary deoxyribonucleic acid
cDNA	complementary deoxyribonucleic acid
CHAPS	3-[(3-cholamidopropyl)dimethylammonio]-1-propanesulfonate
CME	clathrin mediated endocytosis
COS	CV-1 (simian) in Origin, and carrying the SV40 genetic materia
CV	column volume
cytC	cytochrome C
dd	double destilled
DMEM	Dulbecco's Modified Eagle Medium
DNA	*deoxyribonucleic acid*
DNM1L	dynamin 1-like protein
dNTP	deoxynucleoside triphosphate
Dpn	*Diplococcus pneumoniae*
DTT	dithiothreitol
E	extinction
E. coli	*Escherichia coli*
e.g.	exempli gratia
EcoR	*Escherichia coli R*
EDTA	ethylenediaminetetraacetic acid
eGFP	enhanced green fluorescent protein
EM	electron microscopy
EPR	electron paramagnetic resonance
ER	endoplasmic reticulum
FTIR	fourier transform infrared spectroscopy
fw	forward
g	G-force
GED	GTPase effector domain
GFP	green fluorescent protein
GMPPCP	guanosine-5'-[(β,γ)-methyleno]triphosphate
GMP-PNP	5'-guanylyl-β-γ-imidodiphosphate
h	hour
HEPES	4-(2-hydroxyethyl)-1-piperazineethanesulfonic acid
Hind	*Haemophilus influenzae*
HP	high performance
HPLC	high pressure liquid chromatography
HRP	horse-radish peroxidase
hs	*homo sapiens*
I3 (-4, -5)	interface-3, -4, -5
ID	identification
L	litre
LB	Luria-Bertani
Log	logarithm
MD	middle domain
MES	2-(N-morpholino)ethanesulfonic acid
Mff	mitochondrial fission factor
MOPS	3-(N-morpholino)propanesulfonic acid
MPD	2-methyl-1,3-propanediol
mt	mitochondrial
MTS	mitochondrial targeting sequence
NMR	nuclear magnetic resonance
NTP	nucleotide triphosphate binding protein
O/N	overnight
OD	optical density
PAGE	polyacrylamide gel electrophoresis
PBS	phosphate buffered saline
PEG	polyethylene glycol

_____

Pfu	*Pyrococcus furiosus*
PHD	pleckstrin homology domain
PKC	protein kinase C
PRD	proline-rich domain
ps	protein standard
PS	phosphatidylserine
R.m.s.	root mean square
resp.	respectively
rev	reverse
ROI	region of interest
RS	restriction site
RT	room temperature
SDS	sodium dodecyl sulfate
SEC	size-exclusion chromatography
SEM	standard error of the mean
sm	silent mutation
TB	Terrific-Broth
TBA(B)	tetrabutylammonium (bromide)
TBE	Tris/Borate/EDTA
TMD	transmembrane domain
Tris	tris(hydroxymethyl)aminomethane
TSS	transformation and storage solution
U	unit
w/o	without
w/v	weight per volume

For amino acids, the one and three letter code was used: A, Ala: alanine; C, Cys: cysteine; D, Asp: aspartate; E, Glu: glutamate; F, Phe: phenylalanine; G, Gly: glycine; H, His: histidine; I, Ile: isoleucine; K, Lys: lysine; L, Leu: leucine; M, Met: methionine; N, Asn: asparagine; P, Pro: proline; Q, Gln: glutamine; R, Arg: arginine; S, Ser: serine; T, Thr: threonine; V, Val: valine; W, Trp: tryptophane; Y, Tyr: tyrosine; x: any amino acid.

Bibliography

1. Palade, G.E., *An electron microscope study of the mitochondrial structure.* J Histochem Cytochem, 1953. **1**(4): p. 188-211.
2. Saraste, M., *Oxidative phosphorylation at the fin de siecle.* Science, 1999. **283**(5407): p. 1488-93.
3. Youle, R.J. and M. Karbowski, *Mitochondrial fission in apoptosis.* Nat Rev Mol Cell Biol, 2005. **6**(8): p. 657-63.
4. Thrash, J.C., et al., *Phylogenomic evidence for a common ancestor of mitochondria and the SAR11 clade.* Sci Rep, 2011. **1**: p. 13.
5. Mereschkowski, K.S., *Theorie der zwei Plasmaarten als Grundlage der Symbiogenesis, einer neuen Lehre von der Entstehung der Organismen.* Biol Centralbl, 1910. **30**: p. 353-367.
6. Berdanier, C.D., *Mitochondria in health and disease.* Oxidative stress and disease2005, Boca Raton, FL: Taylor & Francis/CRC Press. xix, 619 p.
7. Logan, D.C., *The mitochondrial compartment.* J Exp Bot, 2006. **57**(6): p. 1225-43.
8. van Meer, G., D.R. Voelker, and G.W. Feigenson, *Membrane lipids: where they are and how they behave.* Nat Rev Mol Cell Biol, 2008. **9**(2): p. 112-24.
9. Newby, Z.E., et al., *Crystal structure of the aquaglyceroporin PfAQP from the malarial parasite Plasmodium falciparum.* Nat Struct Mol Biol, 2008. **15**(6): p. 619-25.
10. Chen, X.J. and R.A. Butow, *The organization and inheritance of the mitochondrial genome.* Nat Rev Genet, 2005. **6**(11): p. 815-25.
11. Hoffmann, H.P. and C.J. Avers, *Mitochondrion of yeast: ultrastructural evidence for one giant, branched organelle per cell.* Science, 1973. **181**(4101): p. 749-51.
12. Hoppins, S., L. Lackner, and J. Nunnari, *The machines that divide and fuse mitochondria.* Annu Rev Biochem, 2007. **76**: p. 751-80.
13. Nunnari, J. and A. Suomalainen, *Mitochondria: in sickness and in health.* Cell, 2012. **148**(6): p. 1145-59.
14. Cho, D.H., T. Nakamura, and S.A. Lipton, *Mitochondrial dynamics in cell death and neurodegeneration.* Cell Mol Life Sci, 2010. **67**(20): p. 3435-47.
15. Twig, G., et al., *Fission and selective fusion govern mitochondrial segregation and elimination by autophagy.* EMBO J, 2008. **27**(2): p. 433-46.
16. Suen, D.F., K.L. Norris, and R.J. Youle, *Mitochondrial dynamics and apoptosis.* Genes Dev, 2008. **22**(12): p. 1577-90.
17. Youle, R.J. and A.M. van der Bliek, *Mitochondrial fission, fusion, and stress.* Science, 2012. **337**(6098): p. 1062-5.
18. Westermann, B., *Mitochondrial fusion and fission in cell life and death.* Nat Rev Mol Cell Biol, 2010. **11**(12): p. 872-84.
19. Bustamante, E. and P.L. Pedersen, *High aerobic glycolysis of rat hepatoma cells in culture: role of mitochondrial hexokinase.* Proc Natl Acad Sci U S A, 1977. **74**(9): p. 3735-9.
20. Schapira, A.H., *Etiology of Parkinson's disease.* Neurology, 2006. **66**(10 Suppl 4): p. S10-23.

_____

21. Calvo, J., et al., *Genotype-phenotype correlations in Charcot-Marie-Tooth disease type 2 caused by mitofusin 2 mutations.* Arch Neurol, 2009. **66**(12): p. 1511-6.

22. Hudson, G., et al., *Mutation of OPA1 causes dominant optic atrophy with external ophthalmoplegia, ataxia, deafness and multiple mitochondrial DNA deletions: a novel disorder of mtDNA maintenance.* Brain, 2008. **131**(Pt 2): p. 329-37.

23. Chen, H. and D.C. Chan, *Mitochondrial dynamics--fusion, fission, movement, and mitophagy--in neurodegenerative diseases.* Hum Mol Genet, 2009. **18**(R2): p. R169-76.

24. Cho, D.H., et al., *S-nitrosylation of Drp1 mediates beta-amyloid-related mitochondrial fission and neuronal injury.* Science, 2009. **324**(5923): p. 102-5.

25. Bossy, B., et al., *S-Nitrosylation of DRP1 does not affect enzymatic activity and is not specific to Alzheimer's disease.* J Alzheimers Dis, 2010. **20 Suppl 2**: p. S513-26.

26. Waterham, H.R., et al., *A lethal defect of mitochondrial and peroxisomal fission.* N Engl J Med, 2007. **356**(17): p. 1736-41.

27. Saraste, M., P.R. Sibbald, and A. Wittinghofer, *The P-loop--a common motif in ATP- and GTP-binding proteins.* Trends Biochem Sci, 1990. **15**(11): p. 430-4.

28. Leipe, D.D., et al., *Classification and evolution of P-loop GTPases and related ATPases.* J Mol Biol, 2002. **317**(1): p. 41-72.

29. Hall, A., *GTPases.* Frontiers in molecular biology2000, New York: Oxford University Press. xix, 340 p.

30. Schwefel, D., et al., *Structural basis of oligomerization in septin-like GTPase of immunity-associated protein 2 (GIMAP2).* Proc Natl Acad Sci U S A, 2010.

31. Praefcke, G.J. and H.T. McMahon, *The dynamin superfamily: universal membrane tubulation and fission molecules?* Nat Rev Mol Cell Biol, 2004. **5**(2): p. 133-47.

32. Haller, O., S. Stertz, and G. Kochs, *The Mx GTPase family of interferon-induced antiviral proteins.* Microbes Infect, 2007. **9**(14-15): p. 1636-43.

33. Low, H.H. and J. Lowe, *A bacterial dynamin-like protein.* Nature, 2006. **444**(7120): p. 766-9.

34. Prakash, B., et al., *Structure of human guanylate-binding protein 1 representing a unique class of GTP-binding proteins.* Nature, 2000. **403**(6769): p. 567-71.

35. Daumke, O., et al., *Architectural and mechanistic insights into an EHD ATPase involved in membrane remodelling.* Nature, 2007. **449**(7164): p. 923-927.

36. Hales, K.G. and M.T. Fuller, *Developmentally regulated mitochondrial fusion mediated by a conserved, novel, predicted GTPase.* Cell, 1997. **90**(1): p. 121-9.

37. Alexander, C., et al., *OPA1, encoding a dynamin-related GTPase, is mutated in autosomal dominant optic atrophy linked to chromosome 3q28.* Nat Genet, 2000. **26**(2): p. 211-5.

38. Gammie, A.E., et al., *DNM1, a dynamin-related gene, participates in endosomal trafficking in yeast.* J Cell Biol, 1995. **130**(3): p. 553-66.

39. Vetter, I.R. and A. Wittinghofer, *The guanine nucleotide-binding switch in three dimensions.* Science, 2001. **294**(5545): p. 1299-304.

40.	Bourne, H.R., D.A. Sanders, and F. McCormick, *The GTPase superfamily: conserved structure and molecular mechanism.* Nature, 1991. **349**(6305): p. 117-27.

41.	Mears, J.A., P. Ray, and J.E. Hinshaw, *A corkscrew model for dynamin constriction.* Structure, 2007. **15**(10): p. 1190-202.

42.	Reubold, T.F., et al., *Crystal structure of the GTPase domain of rat dynamin 1.* Proc Natl Acad Sci U S A, 2005. **102**(37): p. 13093-8.

43.	Grigliatti, T.A., et al., *Temperature-sensitive mutations in Drosophila melanogaster. XIV. A selection of immobile adults.* Mol Gen Genet, 1973. **120**(2): p. 107-14.

44.	Kosaka, T. and K. Ikeda, *Possible temperature-dependent blockage of synaptic vesicle recycling induced by a single gene mutation in Drosophila.* J Neurobiol, 1983. **14**(3): p. 207-25.

45.	Koenig, J.H. and K. Ikeda, *Disappearance and reformation of synaptic vesicle membrane upon transmitter release observed under reversible blockage of membrane retrieval.* J Neurosci, 1989. **9**(11): p. 3844-60.

46.	Shpetner, H.S. and R.B. Vallee, *Identification of dynamin, a novel mechanochemical enzyme that mediates interactions between microtubules.* Cell, 1989. **59**(3): p. 421-32.

47.	Shpetner, H.S. and R.B. Vallee, *Dynamin is a GTPase stimulated to high levels of activity by microtubules.* Nature, 1992. **355**(6362): p. 733-5.

48.	Obar, R.A., et al., *Molecular cloning of the microtubule-associated mechanochemical enzyme dynamin reveals homology with a new family of GTP-binding proteins.* Nature, 1990. **347**(6290): p. 256-61.

49.	Urrutia, R., et al., *The dynamins: redundant or distinct functions for an expanding family of related GTPases?* Proc Natl Acad Sci U S A, 1997. **94**(2): p. 377-84.

50.	Gao, S., et al., *Structural basis of oligomerization in the stalk region of dynamin-like MxA.* Nature, 2010. **465**(7297): p. 502-6.

51.	Muhlberg, A.B., D.E. Warnock, and S.L. Schmid, *Domain structure and intramolecular regulation of dynamin GTPase.* EMBO J, 1997. **16**(22): p. 6676-83.

52.	Hinshaw, J.E. and S.L. Schmid, *Dynamin self-assembles into rings suggesting a mechanism for coated vesicle budding.* Nature, 1995. **374**(6518): p. 190-2.

53.	Takei, K., et al., *Tubular membrane invaginations coated by dynamin rings are induced by GTP-gamma S in nerve terminals.* Nature, 1995. **374**(6518): p. 186-90.

54.	Tuma, P.L., M.C. Stachniak, and C.A. Collins, *Activation of dynamin GTPase by acidic phospholipids and endogenous rat brain vesicles.* J Biol Chem, 1993. **268**(23): p. 17240-6.

55.	Stowell, M.H., et al., *Nucleotide-dependent conformational changes in dynamin: evidence for a mechanochemical molecular spring.* Nat Cell Biol, 1999. **1**(1): p. 27-32.

56.	Sweitzer, S.M. and J.E. Hinshaw, *Dynamin undergoes a GTP-dependent conformational change causing vesiculation.* Cell, 1998. **93**(6): p. 1021-9.

57.	Marks, B., et al., *GTPase activity of dynamin and resulting conformation change are essential for endocytosis.* Nature, 2001. **410**(6825): p. 231-5.

58.	Roux, A., et al., *GTP-dependent twisting of dynamin implicates constriction and tension in membrane fission.* Nature, 2006. **441**(7092): p. 528-31.

59.   Niemann, H.H., et al., *Crystal structure of a dynamin GTPase domain in both nucleotide-free and GDP-bound forms.* EMBO J, 2001. **20**(21): p. 5813-21.

60.   Sever, S., A.B. Muhlberg, and S.L. Schmid, *Impairment of dynamin's GAP domain stimulates receptor-mediated endocytosis.* Nature, 1999. **398**(6727): p. 481-6.

61.   Smirnova, E., et al., *A model for dynamin self-assembly based on binding between three different protein domains.* J Biol Chem, 1999. **274**(21): p. 14942-7.

62.   Chappie, J.S., et al., *An intramolecular signaling element that modulates dynamin function in vitro and in vivo.* Mol Biol Cell, 2009. **20**(15): p. 3561-71.

63.   Chappie, J.S., et al., *G domain dimerization controls dynamin's assembly-stimulated GTPase activity.* Nature, 2010. **465**(7297): p. 435-40.

64.   Scheffzek, K., et al., *The Ras-RasGAP complex: structural basis for GTPase activation and its loss in oncogenic Ras mutants.* Science, 1997. **277**(5324): p. 333-8.

65.   Chappie, J.S., et al., *A pseudoatomic model of the dynamin polymer identifies a hydrolysis-dependent powerstroke.* Cell, 2011. **147**(1): p. 209-22.

66.   Haslam, R.J., H.B. Koide, and B.A. Hemmings, *Pleckstrin domain homology.* Nature, 1993. **363**(6427): p. 309-10.

67.   Ferguson, K.M., et al., *Crystal structure at 2.2 A resolution of the pleckstrin homology domain from human dynamin.* Cell, 1994. **79**(2): p. 199-209.

68.   Faelber, K., et al., *Crystal structure of nucleotide-free dynamin.* Nature, 2011. **477**(7366): p. 556-60.

69.   Ford, M.G., S. Jenni, and J. Nunnari, *The crystal structure of dynamin.* Nature, 2011. **477**(7366): p. 561-6.

70.   Faelber, K., et al., *Structural insights into dynamin-mediated membrane fission.* Structure, 2012. **20**(10): p. 1621-8.

71.   Morlot, S., et al., *Membrane shape at the edge of the dynamin helix sets location and duration of the fission reaction.* Cell, 2012. **151**(3): p. 619-29.

72.   Staeheli, P. and O. Haller, *Interferon-induced human protein with homology to protein Mx of influenza virus-resistant mice.* Mol Cell Biol, 1985. **5**(8): p. 2150-3.

73.   Holzinger, D., et al., *Induction of MxA gene expression by influenza A virus requires type I or type III interferon signaling.* J Virol, 2007. **81**(14): p. 7776-85.

74.   Haller, O. and G. Kochs, *Human MxA Protein: An Interferon-Induced Dynamin-Like GTPase with Broad Antiviral Activity.* J Interferon Cytokine Res, 2011.

75.   Reichelt, M., et al., *Missorting of LaCrosse virus nucleocapsid protein by the interferon-induced MxA GTPase involves smooth ER membranes.* Traffic, 2004. **5**(10): p. 772-84.

76.   Kochs, G. and O. Haller, *Interferon-induced human MxA GTPase blocks nuclear import of Thogoto virus nucleocapsids.* Proc Natl Acad Sci U S A, 1999. **96**(5): p. 2082-6.

77.   Accola, M.A., et al., *The antiviral dynamin family member, MxA, tubulates lipids and localizes to the smooth endoplasmic reticulum.* J Biol Chem, 2002. **277**(24): p. 21829-35.

78.   Kochs, G., et al., *Assay and functional analysis of dynamin-like Mx proteins.* Methods Enzymol, 2005. **404**: p. 632-43.

79. Gao, S., et al., *Structure of myxovirus resistance protein a reveals intra- and intermolecular domain interactions required for the antiviral function.* Immunity, 2011. **35**(4): p. 514-25.

80. von der Malsburg, A., et al., *Stalk domain of the dynamin-like MxA GTPase protein mediates membrane binding and liposome tubulation via the unstructured L4 loop.* J Biol Chem, 2011. **286**(43): p. 37858-65.

81. Burmann, F., et al., *A bacterial dynamin-like protein mediating nucleotide-independent membrane fusion.* Mol Microbiol, 2011. **79**(5): p. 1294-304.

82. Low, H.H., et al., *Structure of a bacterial dynamin-like protein lipid tube provides a mechanism for assembly and membrane curving.* Cell, 2009. **139**(7): p. 1342-52.

83. Ghosh, A., et al., *How guanylate-binding proteins achieve assembly-stimulated processive cleavage of GTP to GMP.* Nature, 2006. **440**(7080): p. 101-4.

84. Cheng, Y.S., R.J. Colonno, and F.H. Yin, *Interferon induction of fibroblast proteins with guanylate binding activity.* J Biol Chem, 1983. **258**(12): p. 7746-50.

85. Cheng, Y.S., C.E. Patterson, and P. Staeheli, *Interferon-induced guanylate-binding proteins lack an N(T)KXD consensus motif and bind GMP in addition to GDP and GTP.* Mol Cell Biol, 1991. **11**(9): p. 4717-25.

86. Vestal, D.J. and J.A. Jeyaratnam, *The guanylate-binding proteins: emerging insights into the biochemical properties and functions of this family of large interferon-induced guanosine triphosphatase.* J Interferon Cytokine Res, 2011. **31**(1): p. 89-97.

87. Anderson, S.L., et al., *Interferon-induced guanylate binding protein-1 (GBP-1) mediates an antiviral effect against vesicular stomatitis virus and encephalomyocarditis virus.* Virology, 1999. **256**(1): p. 8-14.

88. Guenzi, E., et al., *The helical domain of GBP-1 mediates the inhibition of endothelial cell proliferation by inflammatory cytokines.* EMBO J, 2001. **20**(20): p. 5568-77.

89. Praefcke, G.J., et al., *Nucleotide-binding characteristics of human guanylate-binding protein 1 (hGBP1) and identification of the third GTP-binding motif.* J Mol Biol, 1999. **292**(2): p. 321-32.

90. Schwemmle, M. and P. Staeheli, *The interferon-induced 67-kDa guanylate-binding protein (hGBP1) is a GTPase that converts GTP to GMP.* J Biol Chem, 1994. **269**(15): p. 11299-305.

91. Neun, R., et al., *GTPase properties of the interferon-induced human guanylate-binding protein 2.* FEBS Lett, 1996. **390**(1): p. 69-72.

92. Prakash, B., et al., *Triphosphate structure of guanylate-binding protein 1 and implications for nucleotide binding and GTPase mechanism.* EMBO J, 2000. **19**(17): p. 4555-64.

93. Shao, Y., et al., *Pincher, a pinocytic chaperone for nerve growth factor/TrkA signaling endosomes.* J Cell Biol, 2002. **157**(4): p. 679-91.

94. Grant, B., et al., *Evidence that RME-1, a conserved C. elegans EH-domain protein, functions in endocytic recycling.* Nat Cell Biol, 2001. **3**(6): p. 573-9.

95. Caplan, S., et al., *A tubular EHD1-containing compartment involved in the recycling of major histocompatibility complex class I molecules to the plasma membrane.* EMBO J, 2002. **21**(11): p. 2557-67.

96. Chen, H., J.M. McCaffery, and D.C. Chan, *Mitochondrial fusion protects against neurodegeneration in the cerebellum.* Cell, 2007. **130**(3): p. 548-62.

97. Chen, H., et al., *Mitochondrial fusion is required for mtDNA stability in skeletal muscle and tolerance of mtDNA mutations.* Cell, 2010. **141**(2): p. 280-9.

98. Zuchner, S., et al., *Mutations in the mitochondrial GTPase mitofusin 2 cause Charcot-Marie-Tooth neuropathy type 2A.* Nat Genet, 2004. **36**(5): p. 449-51.

99. Shin, H.W., et al., *Identification and subcellular localization of a novel mammalian dynamin-related protein homologous to yeast Vps1p and Dnm1p.* J Biochem, 1997. **122**(3): p. 525-30.

100. Kamimoto, T., et al., *Dymple, a novel dynamin-like high molecular weight GTPase lacking a proline-rich carboxyl-terminal domain in mammalian cells.* J Biol Chem, 1998. **273**(2): p. 1044-51.

101. Imoto, M., I. Tachibana, and R. Urrutia, *Identification and functional characterization of a novel human protein highly related to the yeast dynamin-like GTPase Vps1p.* J Cell Sci, 1998. **111 (Pt 10)**: p. 1341-9.

102. Yoon, Y., et al., *A novel dynamin-like protein associates with cytoplasmic vesicles and tubules of the endoplasmic reticulum in mammalian cells.* J Cell Biol, 1998. **140**(4): p. 779-93.

103. Labrousse, A.M., et al., *C. elegans dynamin-related protein DRP-1 controls severing of the mitochondrial outer membrane.* Mol Cell, 1999. **4**(5): p. 815-26.

104. Smirnova, E., et al., *Dynamin-related protein Drp1 is required for mitochondrial division in mammalian cells.* Mol Biol Cell, 2001. **12**(8): p. 2245-56.

105. Smirnova, E., et al., *A human dynamin-related protein controls the distribution of mitochondria.* J Cell Biol, 1998. **143**(2): p. 351-8.

106. Koch, A., et al., *Dynamin-like protein 1 is involved in peroxisomal fission.* J Biol Chem, 2003. **278**(10): p. 8597-605.

107. Benard, G. and M. Karbowski, *Mitochondrial fusion and division: Regulation and role in cell viability.* Semin Cell Dev Biol, 2009. **20**(3): p. 365-74.

108. Friedman, J.R., et al., *ER tubules mark sites of mitochondrial division.* Science, 2011. **334**(6054): p. 358-62.

109. Otera, H., et al., *Mff is an essential factor for mitochondrial recruitment of Drp1 during mitochondrial fission in mammalian cells.* J Cell Biol, 2010. **191**(6): p. 1141-1158.

110. Palmer, C.S., et al., *MiD49 and MiD51, new components of the mitochondrial fission machinery.* EMBO Rep, 2011. **12**(6): p. 565-73.

111. Zhao, J., et al., *Human MIEF1 recruits Drp1 to mitochondrial outer membranes and promotes mitochondrial fusion rather than fission.* EMBO J, 2011. **30**(14): p. 2762-78.

112. Koch, A., et al., *A role for Fis1 in both mitochondrial and peroxisomal fission in mammalian cells.* Mol Biol Cell, 2005. **16**(11): p. 5077-86.

113. Yoon, Y., et al., *The mitochondrial protein hFis1 regulates mitochondrial fission in mammalian cells through an interaction with the dynamin-like protein DLP1.* Mol Cell Biol, 2003. **23**(15): p. 5409-20.

114. Griffin, E.E., J. Graumann, and D.C. Chan, *The WD40 protein Caf4p is a component of the mitochondrial fission machinery and recruits Dnm1p to mitochondria.* J Cell Biol, 2005. **170**(2): p. 237-48.

115. Lackner, L.L., J.S. Horner, and J. Nunnari, *Mechanistic analysis of a dynamin effector.* Science, 2009. **325**(5942): p. 874-7.

116. Tieu, Q. and J. Nunnari, *Mdv1p is a WD repeat protein that interacts with the dynamin-related GTPase, Dnm1p, to trigger mitochondrial division.* J Cell Biol, 2000. **151**(2): p. 353-66.

_____

117. Ingerman, E., et al., *Dnm1 forms spirals that are structurally tailored to fit mitochondria.* J Cell Biol, 2005. **170**(7): p. 1021-7.

118. Mears, J.A., et al., *Conformational changes in Dnm1 support a contractile mechanism for mitochondrial fission.* Nat Struct Mol Biol, 2011. **18**(1): p. 20-6.

119. Zhang, P. and J.E. Hinshaw, *Three-dimensional reconstruction of dynamin in the constricted state.* Nat Cell Biol, 2001. **3**(10): p. 922-6.

120. Chen, Y.J., et al., *The stalk region of dynamin drives the constriction of dynamin tubes.* Nat Struct Mol Biol, 2004. **11**(6): p. 574-5.

121. Sambrook, J., P. MacCallum, and D. Russel, *Molecular Cloning: A Laboratory Manual.* Vol. 3. 2001: Cold Spring Harbor Laboratory Press. 2344.

122. Chung, C.T., S.L. Niemela, and R.H. Miller, *One-step preparation of competent Escherichia coli: transformation and storage of bacterial cells in the same solution.* Proc Natl Acad Sci U S A, 1989. **86**(7): p. 2172-5.

123. Thompson, J.D., D.G. Higgins, and T.J. Gibson, *CLUSTAL W: improving the sensitivity of progressive multiple sequence alignment through sequence weighting, position-specific gap penalties and weight matrix choice.* Nucleic Acids Res, 1994. **22**(22): p. 4673-80.

124. Laemmli, U.K., *Cleavage of structural proteins during the assembly of the head of bacteriophage T4.* Nature, 1970. **227**(5259): p. 680-5.

125. Moos, M., Jr., N.Y. Nguyen, and T.Y. Liu, *Reproducible high yield sequencing of proteins electrophoretically separated and transferred to an inert support.* J Biol Chem, 1988. **263**(13): p. 6005-8.

126. Wilkins, M.R., et al., *Protein identification and analysis tools in the ExPASy server.* Methods Mol Biol, 1999. **112**: p. 531-52.

127. Lenzen, C., R.H. Cool, and A. Wittinghofer, *Analysis of intrinsic and CDC25-stimulated guanine nucleotide exchange of p21ras-nucleotide complexes by fluorescence measurements.* Methods Enzymol, 1995. **255**: p. 95-109.

128. Schuck, P., *Size-distribution analysis of macromolecules by sedimentation velocity ultracentrifugation and lamm equation modeling.* Biophys J, 2000. **78**(3): p. 1606-19.

129. Sheffield, J.B., *ImageJ, a useful tool for biological image processing and analysis.* Microscopy and Microanalysis, 2007. **13**: p. 200-201.

130. Leslie, A.G., *The integration of macromolecular diffraction data.* Acta Crystallogr D Biol Crystallogr, 2006. **62**(Pt 1): p. 48-57.

131. Kabsch, W., *Xds.* Acta Crystallogr D Biol Crystallogr, 2010. **66**(Pt 2): p. 125-32.

132. Hahn, T., et al., *International tables for crystallography*1984, Dordrecht, Holland ; Boston, U.S.A.Hingham, MA: D. Reidel Pub. Co. ;Sold and distributed in the U.S.A. and Canada by Kluwer Academic Publishers Group. v. <A, A1, B, C, E, G in 12>.

133. Taylor, G., *The phase problem.* Acta Crystallogr D Biol Crystallogr, 2003. **59**(Pt 11): p. 1881-90.

134. McCoy, A.J., et al., *Phaser crystallographic software.* J Appl Crystallogr, 2007. **40**(Pt 4): p. 658-674.

135. Emsley, P. and K. Cowtan, *Coot: model-building tools for molecular graphics.* Acta Crystallogr D Biol Crystallogr, 2004. **60**(Pt 12 Pt 1): p. 2126-32.

136. Murshudov, G.N., A.A. Vagin, and E.J. Dodson, *Refinement of macromolecular structures by the maximum-likelihood method.* Acta Crystallogr D Biol Crystallogr, 1997. **53**(Pt 3): p. 240-55.

_____

137. Adams, P.D., et al., *PHENIX: a comprehensive Python-based system for macromolecular structure solution.* Acta Crystallogr D Biol Crystallogr, 2010. **66**(Pt 2): p. 213-21.
138. Brunger, A.T., *Free R value: cross-validation in crystallography.* Methods Enzymol, 1997. **277**: p. 366-96.
139. Laskowski, R.A. and M.B. Swindells, *LigPlot+: multiple ligand-protein interaction diagrams for drug discovery.* J Chem Inf Model, 2011. **51**(10): p. 2778-86.
140. Schroder, G.F., M. Levitt, and A.T. Brunger, *Super-resolution biomolecular crystallography with low-resolution data.* Nature, 2010. **464**(7292): p. 1218-22.
141. Winn, M.D., et al., *Overview of the CCP4 suite and current developments.* Acta Crystallogr D Biol Crystallogr, 2011. **67**(Pt 4): p. 235-42.
142. Landau, M., et al., *ConSurf 2005: the projection of evolutionary conservation scores of residues on protein structures.* Nucleic Acids Res, 2005. **33**(Web Server issue): p. W299-302.
143. Steinkellner, G., et al., *VASCo: computation and visualization of annotated protein surface contacts.* BMC Bioinformatics, 2009. **10**: p. 32.
144. Schrodinger, LLC, *The PyMOL Molecular Graphics System, Version 1.3r1,* 2010.
145. Davis, I.W., et al., *MolProbity: all-atom contacts and structure validation for proteins and nucleic acids.* Nucleic Acids Res, 2007. **35**(Web Server issue): p. W375-83.
146. Pettersen, E.F., et al., *UCSF Chimera--a visualization system for exploratory research and analysis.* J Comput Chem, 2004. **25**(13): p. 1605-12.
147. Richter, M.F., et al., *Interferon-induced MxA protein. GTP binding and GTP hydrolysis properties.* J Biol Chem, 1995. **270**(22): p. 13512-7.
148. Cole, C., J.D. Barber, and G.J. Barton, *The Jpred 3 secondary structure prediction server.* Nucleic Acids Res, 2008. **36**(Web Server issue): p. W197-201.
149. Hope, H., *Cryocrystallography of biological macromolecules: a generally applicable method.* Acta Crystallogr B, 1988. **44 (Pt 1)**: p. 22-6.
150. Chen, V.B., et al., *MolProbity: all-atom structure validation for macromolecular crystallography.* Acta Crystallogr D Biol Crystallogr, 2010. **66**(Pt 1): p. 12-21.
151. Jensen, R.E., et al., *Yeast mitochondrial dynamics: fusion, division, segregation, and shape.* Microsc Res Tech, 2000. **51**(6): p. 573-83.
152. Ramachandran, R., et al., *The dynamin middle domain is critical for tetramerization and higher-order self-assembly.* EMBO J, 2007. **26**(2): p. 559-66.
153. Strack, S. and J.T. Cribbs, *Allosteric modulation of drp1 mechanoenzyme assembly and mitochondrial fission by the variable domain.* J Biol Chem, 2012. **287**(14): p. 10990-1001.
154. Zhang, Y., X. Gao, and R.M. Garavito, *Biochemical characterization of human dynamin-like protein 1.* J Biochem, 2011. **150**(6): p. 627-33.
155. Figueroa-Romero, C., et al., *SUMOylation of the mitochondrial fission protein Drp1 occurs at multiple nonconsensus sites within the B domain and is linked to its activity cycle.* FASEB J, 2009. **23**(11): p. 3917-27.
156. Cereghetti, G.M., et al., *Dephosphorylation by calcineurin regulates translocation of Drp1 to mitochondria.* Proc Natl Acad Sci U S A, 2008. **105**(41): p. 15803-8.

_____

157.   Chang, C.R. and C. Blackstone, *Drp1 phosphorylation and mitochondrial regulation.* EMBO Rep, 2007. **8**(12): p. 1088-9; author reply 1089-90.

158.   Cribbs, J.T. and S. Strack, *Reversible phosphorylation of Drp1 by cyclic AMP-dependent protein kinase and calcineurin regulates mitochondrial fission and cell death.* EMBO Rep, 2007. **8**(10): p. 939-44.

159.   Han, X.J., et al., *CaM kinase I alpha-induced phosphorylation of Drp1 regulates mitochondrial morphology.* J Cell Biol, 2008. **182**(3): p. 573-85.

160.   Taguchi, N., et al., *Mitotic phosphorylation of dynamin-related GTPase Drp1 participates in mitochondrial fission.* J Biol Chem, 2007. **282**(15): p. 11521-9.

161.   Gandre-Babbe, S. and A.M. van der Bliek, *The novel tail-anchored membrane protein Mff controls mitochondrial and peroxisomal fission in mammalian cells.* Mol Biol Cell, 2008. **19**(6): p. 2402-12.

162.   Mitra, K. and J. Lippincott-Schwartz, *Analysis of mitochondrial dynamics and functions using imaging approaches.* Curr Protoc Cell Biol, 2010. **Chapter 4**: p. Unit 4 25 1-21.

163.   Feuerstein, J., R.S. Goody, and A. Wittinghofer, *Preparation and characterization of nucleotide-free and metal ion-free p21 "apoprotein".* J Biol Chem, 1987. **262**(18): p. 8455-8.

164.   Sesaki, H. and R.E. Jensen, *Division versus fusion: Dnm1p and Fzo1p antagonistically regulate mitochondrial shape.* J Cell Biol, 1999. **147**(4): p. 699-706.

165.   Roux, A., et al., *Membrane curvature controls dynamin polymerization.* Proc Natl Acad Sci U S A, 2010. **107**(9): p. 4141-6.

166.   Alberts, B., *Molecular biology of the cell.* 5th ed2008, New York: Garland Science.

167.   Ashrafian, H., et al., *A mutation in the mitochondrial fission gene Dnm1l leads to cardiomyopathy.* PLoS Genet, 2010. **6**(6): p. e1001000.

168.   Tanaka, A., S. Kobayashi, and Y. Fujiki, *Peroxisome division is impaired in a CHO cell mutant with an inactivating point-mutation in dynamin-like protein 1 gene.* Exp Cell Res, 2006. **312**(9): p. 1671-84.

169.   Chang, C.R. and C. Blackstone, *Cyclic AMP-dependent protein kinase phosphorylation of Drp1 regulates its GTPase activity and mitochondrial morphology.* J Biol Chem, 2007. **282**(30): p. 21583-7.

170.   Chang, C.R., et al., *A lethal de novo mutation in the middle domain of the dynamin-related GTPase Drp1 impairs higher order assembly and mitochondrial division.* J Biol Chem, 2010. **285**(42): p. 32494-503.

Abstract

Mitochondria form a dynamic cytoskeleton-associated tubulovesicular network throughout the whole cell which continuously undergoes fusion- and division processes; collectively termed mitochondrial dynamics. Mitochondrial dynamics is an important cellular tool for proper organelle transport to places of high energy demand inside the cell. Furthermore, mitochondrial dynamics functions as quality control mechanism. During lifetime the mitochondrial genome gets more and more heteroplasmic and mitochondrial fusion is an important process to keep the mtDNA content of a cell homogenous. Thus, fusion enables mitochondria with mutations in different genes to cross-complement each other.

In contrast, fission can separate mitochondria from the network which are damaged by, for example, reactive oxygen species for mitophagy and recycling. Since mitochondria cannot be created *de novo*, fission is also required to equally distribute mitochondria during cytogenesis. Several studies showed that disturbed mitochondrial dynamics is implicated in several severe neurodegenerative disorders such as Alzheimer's disease, Parkinson's disease or Huntington's disease.

The key player in the process of mitochondrial division is the large G protein dynamin 1-like protein (DNM1L). In this work DNM1L was structurally and functionally characterized to better understand the process of mitochondrial division and to explain the causes of DNM1L associated diseases on a molecular level.

Despite limited sequence identity, the domain architecture of DNM1L is similar to that observed for dynamin and MxA. DNM1L is composed of a dynamin-specific N-terminal G domain and an elongated four-helical stalk. Both domains are connected via a three-helical bundle; the bundle signaling element (BSE). The stalk is intersected by another domain, termed B insert which is located at equivalent positions like the lipid binding PH domain in dynamin or the substrate binding loop in MxA.

DNM1L assembled via a central stalk interface, and mutations in this interface disrupted dimerization and interfered with membrane binding and mitochondrial targeting. Two sequence stretches at the tip of the stalk were shown to be required for ordered assembly of DNM1L on membranes and its function in mitochondrial fission. In the crystals, DNM1L dimers further assembled via a second, previously

undescribed, stalk interface to form a linear filament. Mutations in this interface interfered with liposome tubulation and mitochondrial remodeling. Based on these results and electron microscopy reconstructions, we propose an oligomerization model for DNM1L which differs from that of dynamin and might be adapted to the remodeling of mitochondria.

Zusammenfassung

Mitochondrien formen ein tubolovesikuläres Netzwerk, welches die gesamte Zelle durchspannt und eng an das Zytoskelett assoziiert ist. Außerdem ist das mitochondriale Netzwerk sehr dynamisch und kontinuierlichen Teilungs- und Fusionsprozessen unterworfen. Dies ermöglicht der Zelle den gezielten Transport von einzelnen Teilen des mitochondrialen Netzwerks zu Orten hohen Energie-(ATP)-verbrauchs innerhalb der Zelle. Außerdem funktionieren Fusions- und Teilungsprozesse als Qualitätssicherungsmaßnahme. Mitochondriale Fusion ermöglicht es der Zelle zum Beispiel, dass mit fortschreitendem Alter zunehmend heteroplasmische mitochondriale Genom homogen zu halten. Mitochondrien mit verschiedenen Mutationen innerhalb ihres Genoms können gezielt verschmelzen und damit ihr Genom gegenseitig komplementieren.

Im Gegensatz dazu ermöglicht mitochondriale Teilung Mitochondrien, die z.B. durch reaktive Sauerstoffspezies stark beschädigt worden sind, vom Netzwerk abzukoppeln und während des mitophagialen Stoffwechselweges gänzlich abzubauen bzw. deren molekulare Bausteine wieder aufzubereiten. Da Mitochondrien zellulär nicht *de novo* synthetisiert werden können, benötigt die Zelle außerdem einen Mechanismus, um während der Zellteilung das mitochondriale Netzwerk gleichmäßig auf beide Tochterzellen aufzuteilen. Fehlfunktionen, die zu gestörten mitochondrialen Fusions- oder Teilungsprozessen führen, wurden in mehreren unabhängigen Studien in Zusammenhang mit ernsthaften neurodegenerativen Erkrankungen wie Alzheimer, Parkinson oder Huntington gebracht.

Der Hauptakteur mitochondrialer Teilung ist das große G protein "Dynamin 1-like Protein" (DNM1L). In dieser Arbeit wurde DNM1L strukturell und biochemisch charakterisiert mit dem Ziel, den molekularen Mechanismus besser zu verstehen, der hinter dem Prozess der mitochondrialen Teilung steckt und um mögliche Ursachen der oben genannten Krankheiten auf molekularer Ebene betrachten zu können.

Obwohl die Sequenzhomologie nur sehr gering ist, zeigt die Struktur von DNM1L große Ähnlichkeit mit den Strukturen klassischen Dynamins und Myxovirusresistenzproteins A (Mx A). DNM1L besteht aus der für Dynaminproteine typischen N-terminalen G domäne und einer elongierten, stielartigen Domäne (engl. stalk), welche aus vier α-Helices besteht. Beide Domänen sind durch ein Dreihelixbündel

miteinander verbunden (Bündelsignalelement; engl. bundle signaling element: BSE). Die stielartige Domäne wird durch eine weitere Domäne unterbrochen, welche B Domäne (engl. B insert) genannt wird und an äquivalenter Position zu den Substratbindedomänen von Dynamin und MxA lokalisiert ist.

In dieser Arbeit konnte gezeigt werden, dass DNM1L analog zu Dynamin und MxA über eine konservierte Interaktionsschnittstelle in der stielartigen Domäne dimerisiert. Mutationsanalysen zeigten, dass die Dimerisierung über diese Schnittstelle von zentraler Bedeutung für die Membranbindung und mitochondriale Remodelierung ist. Außerdem deuten die Ergebnisse dieser Arbeit darauf hin, dass die B Domäne die Bindung von DNM1L an die mitochondriale Außenmembran vermittelt. Außerdem ist ein weiterer ungeordneter Bereich am distalen Ende der stielartigen Domäne wichtig für die geordnete Oligomerisierung von DNM1L und für dessen Membranbindung.

Im Kristall lagerten sich die DNM1L Dimere über eine weitere Schnittstelle in der stielartigen Domäne zusammen, welche bisher für kein Protein der Dynaminsuperfamilie beschrieben worden ist. Mutationen, die diese Schnittstelle auflösen, führten zu einer gestörten Tubulierung von Liposomen *in vitro* und zum Ausbleiben der Lokalisierung von DNM1L an die mitochondraile Außenmebran *in vivo*. Damit verbunden war ein fehlerhafter mitochondrialer Teilungsprozess, der zu vergrößerten, teilweise mehrere µm langen Mitochondrien führte.

Basierend auf den Ergebnissen dieser Arbeit und cryoelektronenmikroskopischen Studien, schlagen wir ein Oligomerisierungsmodell vor, welches sich von Dynamin und MxA unterscheidet und möglicherweise an die besonderen Anforderungen für den Teilungsprozess der mitochondrialen Doppelmembran und die Größe von Mitochondrien angepasst ist.

Publications

Fröhlich C, Grabiger S, Schwefel D, Faelber K, Rosenbaum E, Mears J, Rocks O Daumke O (2013) Structural insights into oligomerization and mitochondrial remodeling of dynamin 1-like protein. *EMBO J* (in press)

Schwefel D, Fröhlich C, Eichhorst J, Wiesner B, Behlke J, Aravind L, Daumke O (2010) Structural basis for oligomerization in the septin-like GTPase of immunityassociatedproteins 2 (GIMAP2). *Proc Natl Acad Sci U S A* 107(47):20299-304

Schwefel D, Fröhlich C, Daumke O (2010) Purification, crystallization and preliminary X-ray analysis of human GIMAP2. *Acta Cryst* F66:725-9

Acknowledgement

I hereby would like to thank Prof. Dr. Oliver Daumke for his outstanding and excellent supervision. His positive entity, enthusiasm, and scientific skills are super-motivating and a shining example for the whole group. Special thanks to Dr. Katja Faelber and Dr. David Schwefel who generously helped me during data collection and to solve the structure of this fascinating protein. Many thanks also to Dr. Eva Rosenbaum who pimped this thesis with excellent analytical ultracentrifugation data. I want to thank Sabine Werner who is truly the good soul in our group and Marion Papst for excellent technical assistance, Stefan Grabiger who did superb work during his internship and the whole Daumke group for the perfect and helpful atmosphere and for the fun during daily lab work.

My collaboration partners Dr. Jason Mears, Case Western Reserve University of Medicine, Cleveland, OH and Dr. Oliver Rocks, MDC Berlin contributed very valuable to this project.

Dr. Yvette Roske who keeps the Hydra running!

Dr. Bettina Purfürst for teaching me how to use the electron microscope.

Of course a want to thank the MDC for providing such an excellent research environment.

Last but not least I want to thank my friends for giving me hope and inspiration, Sascha, Karina, Fabi, Marlon, Krisi, Thies, Maidi, Max, Kristin, Alexej, Chloé, Riccardo, Magdalena, Claudio, Janko, Song, Anja, Tilman, Jo, Vreni, Nu, Karen, my family, my parents Horst† and Gisela Fröhlich and my brothers Veit, Uwe and Jens. And the sunshine of my life, Glori.

Without you this thesis would not have been what it is. Thank you all!

Erklärung

Ich versichere, dass ich die von mir vorgelegte Dissertation selbständig angefertigt, die benutzten Quellen und Hilfsmittel vollständig angegeben und die Stellen der Arbeit - einschließlich Tabellen, Karten und Abbildungen - die anderen Werken im Wortlaut oder dem Sinn nach entnommen sind, in jedem Einzelfall als Entlehnung kenntlich gemacht habe; dass diese Dissertation noch keiner anderen Fakultät oder Universität zur Prüfung vorgelegen hat. Die Bestimmungen der Promotionsordnung sind mir bekannt. Die von mir vorgelegte Dissertation ist von Prof. Dr. O. Daumke und Prof. Dr. U. Heinemann betreut worden.

Berlin, März 2013

Chris Fröhlich